THESIS

OPTIMIZATION OF PRESSURIZED SOFC-ICE-TURBO HYBRID GENERATION SYSTEM

Submitted by

Hugo Mettes

Department of Mechanical Engineering

In partial fulfillment of the requirements

For the Degree of Master of Science

Colorado State University

Fort Collins, Colorado

Spring 2026

Master's Committee:

Advisor: Todd Bandhauer

Dan Wise
Jeremy Daily

ABSTRACT

OPTIMIZATION OF PRESSURIZED SOFC-ICE-TURBO HYBRID GENERATION SYSTEM

While renewable energy sources are a clear pathway to net-zero emissions, the use of hydrocarbon fuels is still widespread. In the interim high efficiency hydrocarbon power generation systems are required. Solid Oxide Fuel Cell (SOFC) technology is a low emissions alternative to internal combustion engines, being both more efficient and able to run both fossil fuels and hydrogen. SOFC research has made several advancements in recent decades that has further increased their performance and reduced their cost, making them a more viable market alternative. Research has shown SOFC pressurization and hybrid generation increases power density, efficiency, and flexibility. A shift towards pressurized systems running as hybrid generators with internal combustion engines (ICE) has become a viable option to produce >70% efficiencies. However, unlike previous concepts involving gas turbines, ICEs don't pressurize the system. SOFC/ICE hybrids, therefore, require high efficiency electric compressors. This study was focused on the evaluation and optimization of two-stage motored turbochargers within a pressurized SOFC/ICE generation system with key variables of air flow rate, operating pressure, and stack current. First, the motored turbocharger was experimentally validated at increased temperatures to simulate second stage conditions. Then the performance data was incorporated into a system model to optimize the performance of the hybrid SOFC/ICE system over a range of operating conditions. The results showed that the air compression was the most important factor for optimizing the system efficiency with a peak efficiency of 68% achieved at 220 kPa and 80 g/s with a current draw of 35 A.

ACKNOWLEDGMENTS

Dr. Bandhauer, I cannot thank you enough for giving me this opportunity. I came into the lab with a physics background and a love for working with my hands, but near zero experience with formal engineering work. I am grateful that you saw potential for me to be a member of the REACH Colab team. You have fostered a lab environment that develops our independence while keeping us all a connected team, and this has been invaluable to my growth both professionally and socially.

Shane Garland, you have been an incredible supervisor and mentor. Thank you for your patience and calm demeanor throughout the last year and a half. I entered this program missing quite a bit of knowledge, and you never once shied from either helping with a problem or guiding me to solve it on my own. The first few months I stepped by your office several times a day with often elementary questions, and you still were always helpful. You helped me grow my abilities as a student and engineer.

Derek Young, you may not have been directly supervising my research, but you still spent plenty of time helping me with engineering and navigating a new space and field. I want you to know that your outward joyful and optimistic nature was genuinely one of the most wonderful parts of working here. You made the transition from physics undergrad to mechanical engineering grad student easier by being an empathetic and open person. You helped me feel like I belonged here and could get the job done.

I want to thank a few of my professors here at CSU who were pivotal to my success. Dr. Wise, you have been both a great educator and provider of wisdom, I am grateful to have you on my committee and thank you for your support. Dr. Montgomery, thank you for not only helping

me get my first job out of this program, but by proxy has helped me return to the Netherlands. Dr. Dumitrache, thank you for fostering curiosity and helping me learn much of what I will need in my career.

I also want to thank the wonderful people at Regis University, particularly Dr. Gray, my previous advisor and mentor, and Professor Knowles. Both of you were incredible supporters and guides for me. To everyone else who taught classes or survived them with me, I am grateful to you as well.

To everyone at Reach CO-lab, I am incredibly lucky to have worked with you. Those who finished part way through my time here such as Victor and Lars, you were both awesome mentors and incredibly welcoming. Dalton and Sofia, I don't think I could've made it through some of those classes without both your friendship and teamwork. To the rest of the team, you were marvelous company. Working together on homework or goofing around at as a collective, I knew if the day was going to be hard, we could always have a good laugh.

To my family, Mom, Dad, my stepmother Renee, stepfather Terry and siblings Juliette and Sebastian thank you all for the support. Dad, you fostered my love of science from an early age. You have been on this ride with me over the phone helping me think through problems and distracting me with interesting conversation. Mom, you have been a wonderful support and a constant advocate for keeping a passion for life. You let me explore much of myself, never discouraging my experiments in the garage that helped me fall in love with engineering. Renee, I literally would not have been able to go to my undergraduate university without your support, and even with that you still spent hours helping me craft my cover letters for grad school. Terry, you were always there to give a big thumbs up on quite a lot of crazy stuff, and I can't fathom making it here without your support from the start. Sebastian, you have been an unshakable advocate and

saw the engineering spark in me early. You pushed me hard to succeed in my undergrad and here at CSU. I am grateful to all of you, who encouraged my continued education and self-actualization.

To my Wife, Maddie, thank you. You have seen me through the hardships of this degree and everything else that has happened around it. You have been my number one teammate, encouraging me at every step of the way. You were there for the application process, the first rejection letters, and the worst exams and homework assignments, and you persistently encouraged me and helped me believe in myself. I am most grateful to you and your willingness to postpone your master's degree so I could complete mine. I am excited to support you through your graduate education as you did for me.

There are so many more who deserve my gratitude. I want all of you not named here who have been a part of this journey to know that I am incredibly appreciative of you. I can't believe I made it to this point, and to both those mentioned and unmentioned, thank you again.

TABLE OF CONTENTS

LIST OF TABLES

LIST OF FIGURES

NOMENCLATURE

Variable	Description	Units
$\dot{m}$	Fluid mass flow	g/s
T	Temperature	K
p	Pressure	kPa
P	Power	kW
PR	Pressure Ratio	-
Pr	Prandtl Number	-
U	Overall heat transfer coefficient	$W\ K^{-1}\ m^{-1}$
A	Area	m^2
C	Heat capacity rate	$kJ\ s^{-1}\ K^{-1}$
q	Heat transferred	kW
h	Enthalpy	$kJ\ kg^{-1}$
$\bar{h}$	Convective heat transfer coefficient	$kW\ m^{-2}\ K^{-1}$
Nu	Nusselts number	-
NTU	Number of transfer units	-
Re	Reynolds number	-
k	Conductive heat transfer coefficient	$kW\ m^{-1}\ K^{-1}$
Pr	Prandtl number	-
u	Fluid velocity	$m\ s^{-1}$
Cp	Specific heat	$kJ\ kg^{-1}\ K^{-1}$
t	Thickness	m
w	HEX width	m
D	Diameter	m
v	Fluid velocity	$m\ s^{-1}$
L	Pipe length	m
Greek Symbols		
η	Efficiency	%
μ	Dynamic viscosity	Pa s
ε	Effectiveness	-
Δ	Difference	-
ρ	Density	$kg\ m^{-3}$
λ	Moody friction factor	-
ω	Fluid Velocity	$m\ s^{-1}$
Subscript		
i	In	
o	Out	
c	Compressor	
corr	Corrected	
w	Wall	
F	Fluid	

cold	Cold side of HEX	
hot	Hot side of HEX	
ch	Channel within HEX	
h	Hydraulic	
s	Isentropic process	

CHAPTER 1: INTRODUCTION

1.1: Motivation and Background

As of 2024, United States is the second largest consumer of electricity on earth [1]. Electricity is primarily produced by hydrocarbons such as coal and natural gas in the USA. While renewable technologies have been closing the gap, they still rely heavily on these high emission energy sources as shown in Figure 1-1 [2].

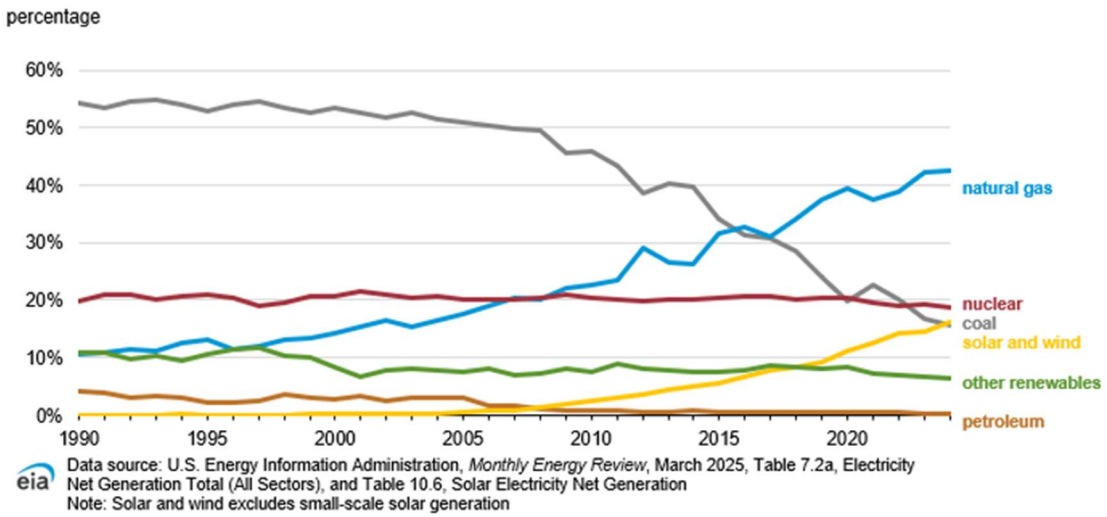

Figure 1-1: Share of U.S electric power sector generation by fuel source, 1990-2024 [2]

This means that the United States has a major impact on total greenhouse gas emissions and has a lot of room to reduce those emissions. While transitioning to renewables is the long-term solution, the use of fossil fuels will remain widespread for the foreseeable future. However, there is still room for improving emissions while using these energy sources. This primarily could be done through improvements in efficiency of the current fossil fuel technologies. An increase in efficiency for these systems would result in less fuel being consumed, which both lowers costs and emissions. Most of the energy produced using fossil fuels is produced with steam power plants or

internal combustion engines. These technologies have had their efficiencies improved since their introductions in the 19th and 20th century, but they have hard efficiency limits set by Carnot efficiency. Reciprocating internal combustion engines, gas turbines (GT), and steam power plants have theoretical efficiency limits between 40 and 60% [3] This means that improving technology has diminishing returns, as these efficiencies cannot be surpassed. However, fuel cells are an alternative method for using these fuels that is not limited by Carnot efficiency.

Fuel cell technology varies greatly; however, they all operate on the same basic principles (Figure 1-2). Fuel is introduced on the anode side and oxidized. This fuel typically consists of hydrogen; however, hydrocarbons and ammonia are possible. Oxygen is broken down into oxides on the cathode side, and either protons or oxide ions are transported through the electrolyte. The electrons are delivered to the load, terminating at the cathode [4]. This operating principle has been applied to many technologies, which usually differ based on the electrolyte being used [5], [6]. The use of an electrochemical process instead of heat results in fuel cells having theoretical efficiency limits around 83%, substantially higher than combustion alternatives. In practice their efficiency ranges from 40-60%, but their performance can be improved greatly, and their lower operating temperatures result in less NOx emissions [4], [7].

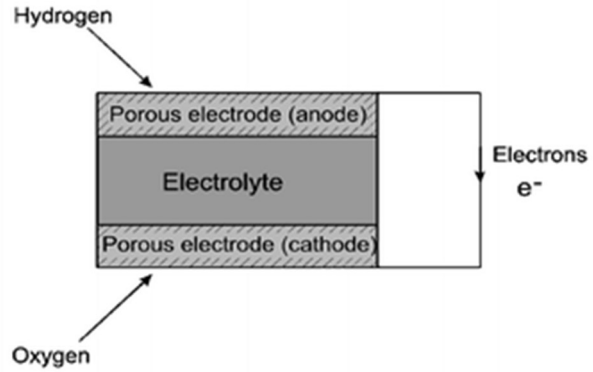

Figure 1-1: Base operating principle of fuel cells [4]

Solid Oxide Fuel Cells (SOFC) are a fuel cell technology that offers many unique capabilities over other fuel cells. SOFCs operate at high efficiencies and have the capacity to

operate on hydrocarbon fuels, enabling them to be used both before and after the grid transition to hydrogen [4]. While their performance on their own is impressive it can be enhanced further by pressurizing the fuel cell, operating the system as a hybrid with an internal combustion engine, and operating at lower temperatures.

Previous work on enhancing the performance of SOFCs via pressurization, hybridization and lowering operating temperatures has been studied [8], [9], [10], [11], [12], [13], [14], [15], [16]. The primary focus of researchers has been on GTs due to their capacity as both a hybrid generator and compression system. These systems can reach impressive maximum thermal efficiencies of 70%. To put this in perspective, a 100-kW high efficiency steam power plant operating at 40% efficiency requires 250-kW worth of fuel. The equivalent SOFC-GT hybrid system would only require 143-kW worth of fuel, nearly cutting consumption and emissions in half. These systems aren't without fault, however, and the weaknesses of GTs leave room for an alternative. A newer concept for increasing performance has been to operate SOFCs with a reciprocating internal combustion engine, which offers several advantages in efficiency and flexibility. Research into the topic has been limited mostly to small scale engine tests, models, and BOP optimizations.

This study is part of collaborative effort between Colorado State University (CSU) and Colorado School of Mines (CSM) to develop a full scale pressurized intermediate temperature 80-kW SOFC-ICE hybrid test facility. The test facility has everything necessary to operate as a power generation system including the fuel and air BOP alongside the SOFC and spark ignited, reciprocating ICE. The air BOP system is unique as it relies on motored compressors instead of the previously studied turbocharger or GT methods of compression. Many of the components within the system have been modeled and tested, including the fuel cell stacks, engine, and air

BOP [12], [17], [18], [19], [20]. The first air BOP system explored by Mitchel et al. was lacking turbines for additional performance increases and the compressors performed below desired efficiency levels. This has resulted in new motored turbochargers being introduced to replace the previous positive displacement compressors.

1.2: Research Objectives

While the optimization of positive displacement compressors for an SOFC-ICE system has been completed, a study on the relationship between motored air BOP systems and the SOFC-ICE has not. Modeling of a similar system using the ICE turbocharger as the compression system has been done [21], however the use of real components and a full-scale facility is missing from the literature. This study aims to model and analyze the relationship between the SOFC-ICE and air delivery system and find an optimal running condition for an 80-kW system.

Three variables were identified for this study that relate the air systems and SOFC-ICE: air flow rate, pressure, and stack current. These three variables range from 80-120 g/s, 200-300 kPa, and 35-40 A, respectively. These ranges were selected as they give a reasonable scope around the originally selected operation conditions for an 80-kW load. To accomplish the goals of this study the following procedure was followed. First, the new motored turbochargers were tested in a testbench for corrected flowrates of 30-110 g/s and pressure ratios of 1.25 to 2.4 under specific conditions that guide modelling of the second compression stage. Second, a model of the air system was constructed including all heat exchangers, turbines, compressors and other minor components. This model was informed by data from the motored turbocharger manufacturer, testbench data, and model data from other components within the system. Third, the results of the air system model were combined with the results of the SOFC-ICE systems produced by a CSM model. The results of these combined models were analyzed to find the best performance conditions for the system.

1.3: Thesis Structure

This paper is separated into seven chapters. The first contained a preliminary introduction to the topic as well as the research goals of this paper. Chapter two contains an in-depth background on the focus of this study including the motivation, previous relevant works, and the current gaps in the literature that this paper aims to fill. Chapter three contains the description of the test facility, testbench and methods for testing the motored turbocharger used in this study. Chapter four contains the modeling methodology used in this study alongside a description of the CSM model. Chapter five contains the results of both the testing on the turbocharger and the modeling of the air system and SOFC-ICE hybrid system. Chapter six contains the analysis of the results, including explanations for the results and the best design point for the range of conditions. Chapter seven contains concluding remarks, particularly focused on the best operating conditions and improvements that can be made upon the system and turbomachinery.

CHAPTER 2: LITERATURE REVIEW

This literature review will be broken down into five sections for clarity. In section one, solid oxide fuel cells will be discussed as a method of generating electricity, including their operating principles, benefits, and the disadvantages most relevant to this study. Section two will review the literature that discusses addressing the costs of SOFC technology. This section will primarily focus on improvements to air systems and lowering the SOFC operating temperature. Section three will discuss current research conducted on hybrid SOFC systems, including relevant work on air systems. Section four will discuss the gaps in the SOFC hybrid literature and the scope of this work.

2.1: Solid Oxide Fuel Cell Technology

Solid Oxide Fuel Cells the primary focus of this paper, operates on the same basic principles as other fuel cells. They are, however, one of the few fuel cell types to use a solid electrolyte, typically yttria-stabilized zirconia. Additionally, they can operate on both carbon monoxide and hydrogen (Figure 2-1). The cathode is supplied with oxygen via atmospheric air, which is reduced to oxygen ions that pass through the electrolyte. The oxygen ions react with the supplied carbon monoxide and hydrogen to produce water and carbon dioxide. This reaction creates considerable heat and electricity [4].

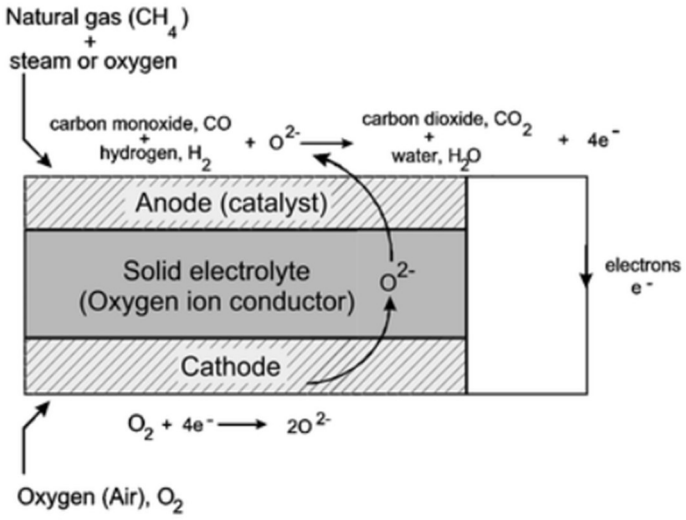

Figure 2-1: SOFC basic operating principles [4]

Because SOFC's run on hydrogen and carbon monoxide at temperatures around 1000°C, they can be fueled with both traditional hydrocarbon fuels and pure hydrogen. These high temperatures offer the opportunity to do internal reforming, reducing the complexity of the fuel system [4], [22]. This fuel flexibility, and their high operating efficiency, make SOFC's an ideal candidate for being a transitional energy conversion device. An SOFC could run on green hydrogen when available while also being a low emissions alternative for running hydrocarbons as fuels.

Solid Oxide Fuel Cells aren't without challenges. The cost of these devices is quite high, and they cannot operate at 100% fuel utilization which results in fuel remaining at the exhaust of the SOFC. The inability to operate at 100% fuel utilization is due to the damage and efficiency losses that occur when there is local fuel starvation. To avoid this fuel starvation, the SOFC operates with more fuel than electrochemically necessary [23]. The high costs involved with SOFCs are a result of several factors, including high rates of degradation, complex manufacturing, and expensive balance of plant (BOP) [24], [25], [26].

Increased degradation of all components of the SOFC introduce both maintenance and material costs. The electrolyte is relatively durable and resistant to high temperatures, however, the materials for the rest of the fuel cell degrade quickly. Addressing this issue would require detailed and complex fabrication processes [26]. The BOP requires extensive material development and cost as well. Both the BOP and fuel cell components degradation is exacerbated by high temperatures within the stacks. For the BOP the result is degradation of the alloy interconnects between cells due to oxidation and chromium evaporation [25]. In addition, the temperatures outside the fuel cell are still significant. Steel and other metals used in supporting structures begin to have degrading strength at these elevated external temperatures (>500°C) [27].

The high operating temperatures also increase the complexity of the full system design. Even at the lower possible operating temperatures (~600°C) temperature gradients can form. Sufficiently large gradients result in deteriorating efficiencies and potential for mechanical failure, particularly at elevated pressures or flows. Avoiding these gradients is vital for operation, however, doing so requires significant complication to the BOP. Consequently, the fuel cell geometries, control systems, and external heat exchangers are more complicated and expensive [28], [29] [30].

2.2: Reducing SOFC Cost by Lowering Operating Temperature

Lowering operating temperature becomes the most obvious method for reducing the costs of SOFC operation. The lowered temperatures would result in decreasing material stress both thermally and chemically, while also simplifying the BOP. In addition, Nernst potential, a major determining factor in SOFC performance, indicates that lowered temperatures would improve cell performance [12], [18]. In practice, however, the opposite trend is observed because other forms of resistance increase at lower temperatures, which starts to counteract any gains made elsewhere.

In addition, the higher resistances of materials at lower temperatures result in an increase in heat generation, pushing the operating temperatures back up.

Lowering the temperatures without decreasing performance of the SOFC necessitates improvements to materials. These improvements include using novel electrolyte and electrode materials, as well as using thinner components. Both methods reduce the material induced overpotentials, while also reducing heat generation due to inefficiency and high resistance [8].

While the performance can be enhanced by material changes, significant gains in performance can also be observed with changes to the air BOP. Researchers have investigated increasing the air mass flow and pressure of the cathode. Increasing airflow has positive effects on stack performance, as it increases the availability of oxygen for chemical reactions and improves heat rejection. This does come at a cost, however, as the increase in airflow correlates with higher power demand from blowers or compressors [23].

Increasing pressure has shown great potential for performance improvement because higher pressure increases the cell operating current. At higher currents the concentration overpotential becomes the dominant loss, reducing concerns for material design. The increase in concentration potential is compensated for by the higher diffusion rates that are a result of increased pressure. In addition, the higher currents result in increased power density. Higher power density means that fewer cells are required to hit a target power [10], [11], [12], [13], [14], [18].

The other reason for operating at high temperatures was the benefit of improved fuel reformation. This is what provided SOFC's with the ability to operate on complex hydrocarbons. However, pressure increases can also improve reformation. Increasing reformation rates through pressure both assist in thermal management and reduce the need for the cells to operate at high temperatures [31].

The increase in pressure and airflow of the cathode comes at the price of increased demand on all components of the air BOP including an increase in power consumption. Not only does the power demand from increased flow and pressurization go up, but the amount of preheating necessary to operate the fuel cells with minimal temperature gradients increases. To address this several approaches have been taken, including only pressurizing the fuel side of the SOFC. This gave the benefit of reducing total power consumption, but the benefit was minimal for SOFC uses, only seeing improvements for electrolysis applications. The single sided pressurization also increased the physical stress on internal components [13]. Another approach is to preheat the air with specially designed SOFC configurations that include internal preheating. This reduces the necessity of expensive external heat exchangers; however, it requires reducing airflow through cathode and increasing the internal temperature gradients [32].

2.3: Hybridization of SOFC's with Additional Power Cycles

Enhancing the performance of SOFCs by lowering their operating temperatures and increasing their operating pressures only provides so much benefit in terms of total efficiency. This is because SOFCs cannot safely operate at 100% fuel utilization. The inability of these devices to do so results in the exhaust gases of the stacks still containing useable energy. If these exhaust gasses go unused the thermal efficiency significantly decreases and emissions are worsened. Fortunately, a few concepts exist to ensure this anode tail gas (ATG) is used efficiently.

The most straightforward solution to increase the global fuel utilization of the SOFC system is to recycle the fuel rich exhaust gases back into the fuel inlet. This provides the ability to precisely control the chemistry of the stacks and not waste fuel. In the case of hydrocarbon use, the added benefit of returning steam back to the inlet assists with the reforming process which can

boost efficiency and reduce costs. Such systems can increase total efficiency to around 66% at full load [31].

The other use for the exhaust gases is to utilize the chemical and heat energy to generate additional electricity. A variety of methods for extracting energy from ATG have been studied, the ones discussed in this paper include both traditional and organic Rankine cycles, the Kalina cycle, GTs, and reciprocating engines. Each of these will be described in the following subsections.

2.3.1:Rankine and Kalina Cycles

The Rankine, organic Rankine, and Kalina cycles all operate on similar principles. Each utilizes a different working fluid; however, they all rely on heat addition to the working fluid that drives a turbine. Both Rankine and organic Rankine cycles operate on a phase change of the fluid at high pressures. The only difference between the two is the use of water in a traditional Rankine cycle, and an alternative fluid such as refrigerant in the organic cycle [3]. Kalina cycles operate similarly but rely on the mixed properties of water and ammonia to generate high temperature vapors that drive a turbine. The advantage of this cycle (alongside organic Rankine) is its ability to operate on low quality heat [33].

Research has been conducted to integrate these cycles with heat from both the combustion of the exhaust gases and the waste heat off the SOFC. This research included operating a top cycle based on the Rankine cycle using the combustion heat, and a bottoming Kalina cycle or organic Rankine cycle off the waste heat from the stacks. Both increase the efficiency (>60%) of the total system but add additional complexity and cost to the system [34], [35].

2.3.2: Gas Turbines

The Brayton cycle or GT cycle primarily relies on air as its working fluid. The cycle compresses the air and then adds heat, typically through the combustion of fuel in the air. This

high pressure and temperature air is run through a turbine which simultaneously drives the compressor and produces electricity. GTs are compact, relatively simple, but are quite limited in their thermal efficiency compared to other internal combustion engines. In addition, their efficiency drops significantly at small scales [3], [36].

GTs can be integrated into a hybrid loop with a SOFC. These GTs can be implemented to preheat and pressurize air for the stacks, and in some cases can be used to generate additional power. Several configurations exist; however, the general approach is the same. Every integration of the concept includes a compressor, combustor, and turbine tied in some capacity to the fuel system of the SOFC. The order of the components can vary depending on the goal of the system.

Three example configurations for SOFC-GT hybrids can be seen in Figure 2-2. Both pressurized and unpressurized variants are possible, with the gas turbine combustion functioning primarily as a method of both preheating the gases in the case where combustion occurs before the stacks, and as a method of preheating and pressurizing in cases where combustion occurs after the stacks [15], [37].

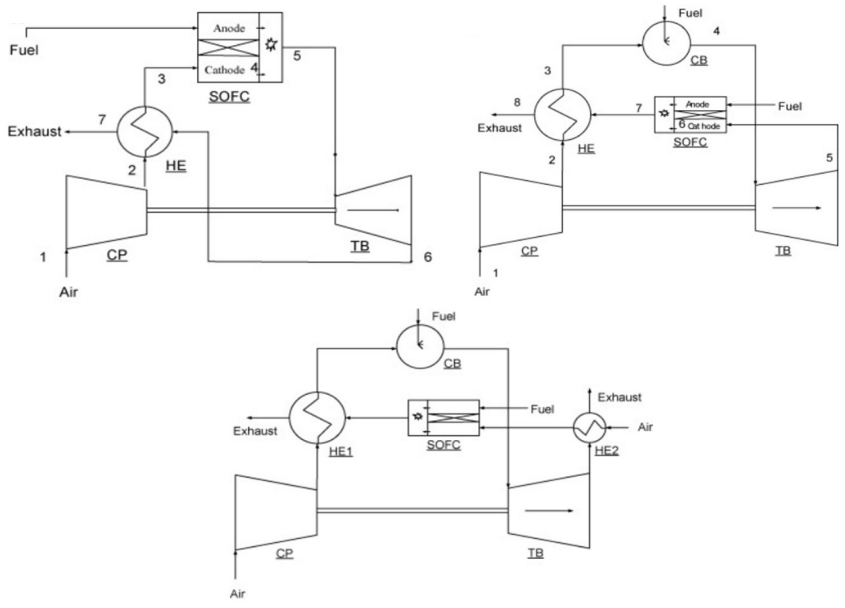

Figure 2-2: Three examples of SOFC-GT hybrid configurations [37]

Models of various configurations found that the efficiency of a SOFC-GT hybrid peaked when both pressurization and heat recuperation from the stacks were implemented. Both the system efficiency itself would increase, and the economic value of high pressure SOFC-GT plants were higher than that of unpressurized equivalents [15], [38]. Williams et al found that gas turbine efficiency had little impact on overall efficiency. This implied that optimizing design of the turbomachinery, such as multiple stages, intercooling and heat recuperation are considered less consequential for SOFC-GT hybrid design [15]. Araki et al, however, produced a model that indicated hybrid operation and pressurization using a gas turbine improves total system efficiency substantially. Araki et al. also showed that intermediate temperature SOFCs at increased pressure were a viable option for high efficiency generation systems [9].

More contemporary study of gas turbines has suggested the optimization of the gas turbine system improves efficiency significantly. Kuchonthara et al. concluded that system efficiency could be increased through the optimization of the heat recuperation system for the gas turbine, especially when introducing steam injection [39]. Diamantis et al. found that specialized design of turbomachinery for SOFC-GT hybrid operation offered a wider operation range in addition to power increases [40]. Studies on single shaft multistage compressors and turbines showed greatly increased performance both in terms of efficiency and turndown ratio when operating pressures are very high [16], [41]. The use of multi-stage turbines was found to increase the operating pressure requirements of the system significantly, and the turbines being on separate shafts could shrink the operating envelope [42]. System efficiency is further improved when the gas turbine is utilized both as a generator and for pressurization. Orschchyn et al. found that power load distribution should be a 66.2/38.2 split in favor of the SOFC. This split could produce a system

efficiency of 75.6%. Other works found similarly increased performance and power distribution when gas turbines drive a generator [15], [16], [39], [41].

Operating a gas turbine with a generator comes with the disadvantage of increasing the total footprint and cost of a SOFC-GT hybrid. In addition, both full sized gas turbines and microturbines are prohibitively expensive in smaller scale applications such as mobile or distributed power systems. These devices have been tested with automotive turbochargers. With the right selection of turbochargers these variants of SOFC-ICE proved to be more efficient than standalone SOFCs. However, controls of these systems are more complex due to the need to accurately control bypass valves in real time to account for strict operating parameters of turbomachines [43], [44].

2.3.3: Reciprocating Engines

Reciprocating engines have been more recently investigated in the literature for use with a SOFC. Reciprocating engines in SOFC hybrid application typically operate on an Otto cycle. This applies whether it is spark ignited ignition (SI) or homogeneous charge compression ignition (HCCI). The one exception to this is reactivity-controlled compression ignition (RCCI), which more closely resembles the diesel cycle [45]. Both cycles operate principally on the compression of air followed by heat addition via combustion. The work is then extracted through the expansion of the gases with a piston [3].

Research into the use of reciprocating engines to generate power off ATG is a recent development within literature. The limitations of gas turbines outlined in the previous section created interest in this alternative generation method commonly referred to as a Solid Oxide Fuel Cell – (reciprocating) Internal Combustion Engine (SOFC-ICE). The advantages of reciprocating engines over gas turbines becomes most apparent at low to medium power applications. The

upfront cost, operating envelope, efficiency, and control complexity all see improvement over GTs in the same application [45], [46].

The reactivity and laminar flame speed of the ATG has been found to be a major limiting factor in the efficacy of a reciprocating engine, particularly spark ignited engines. Previous tests of reciprocating engines showed difficulty igniting the fuel gas [45], [47]. HCCI engines have been the engine of choice for initial experiments running on ATG. Choi et al. showed that a reciprocating engine could run on the fuel provided by the anode exhaust. Running an emulator with a single cylinder engine they were successfully able to test several conditions. They found that tests with highly diluted fuel could still be combusted. Even fuel mixed with steam could still ignite in the HCCI engine. These tests required a high inlet temperature of the engine, which typically lowers overall efficiency. The engine had efficiencies in the range of 25-30%. This showed the viability of operating a reciprocating engine as the bottom cycle of a SOFC hybrid system [48].

Chuahy et al used a similar approach to Choi et al. They used a single piston engine to test ATG compositions in both HCCI and RCCI configurations. The results of these tests were paired with a SOFC-ICE hybrid model, the engine being modeled as a 15 L engine utilizing the same cylinder as the single cylinder test. Their results indicated that this hybrid setup could reliably provide power at the 1 MWe power with an efficiency of 70% (LHV). The study also showed that the laminar flame speed was significantly lower than methane, making SI operation improbable. For SI engines to run on ATG two improvements to the system would need to be made: sufficient condensation prior to the engine inlet, and sufficient turbulence generation within the cylinder [45].

Choi et al. analyzed the operation of an HCCI engine with a SOFC in a separate study. This study used the results of their previous study on the engine paired with a SOFC model. The analysis

had the SOFC operating at ambient pressures but at significantly reduced operating temperatures (~800 K). Because the pressure and temperature of the cells were low, the system efficiency was decreased. The study was able to determine a design point for a 5 kWe class system. Finding that pressure fluctuations from the engine had negligible effect on the stability of the stacks and the efficiency was increased over the equivalent standalone SOFC system [49].

The disadvantage of HCCI engines is that they are better suited for high pressure direct injection much like a diesel engine. Due to the gaseous nature of ATG, HCCI is a less efficient method of generation. Spark assisted ignition (SAI) and SI engines would be better suited for this application [50]. Kim J et al. proved that SAI engines running on ATG was possible. An engine sized for an SOFC-ICE hybrid operating in the 5 kWe class was tested with simulated ATG. The SAI engine proved to be more efficient than its HCCI counterparts while also having more stable combustion. The fuel cell was modeled under ambient pressure conditions and low operating temperatures [50].

Rodriguez et al. analyzed the relationship between SOFC, ICE, and turbocharger. This was done using a system model that varied the SOFC fuel utilization and reformer temperature. The turbocharger relied on the exhaust gas of both the SOFC and engine to power the compression of the system. The study found a peak system efficiency of 62%. The turbocharger required usage of an additional ATG combustor to provide sufficient temperatures when reformer temperatures were low. This study found that the efficiency of the system was driven by the efficiency of the SOFC due to it being the primary power contributor [21].

Reyes-Flores et al. successfully tested a spark ignited anode tail gas engine. The engine required a compression ratio of 17:1, so a modified diesel engine was used for this application. The engine proved the concept could deliver efficient power at the 1 L displacement level. They

found that the peak efficiency of the engine was 31% and much of the losses were due to parasitic loads that would become a less significant draw at larger power scales [19].

2.3.4: Hybrid System Currently Under Development

Colorado State University and Colorado School of Mines have collaborated on a project which aims to address gaps in the literature about pressurized intermediate temperature SOFC-

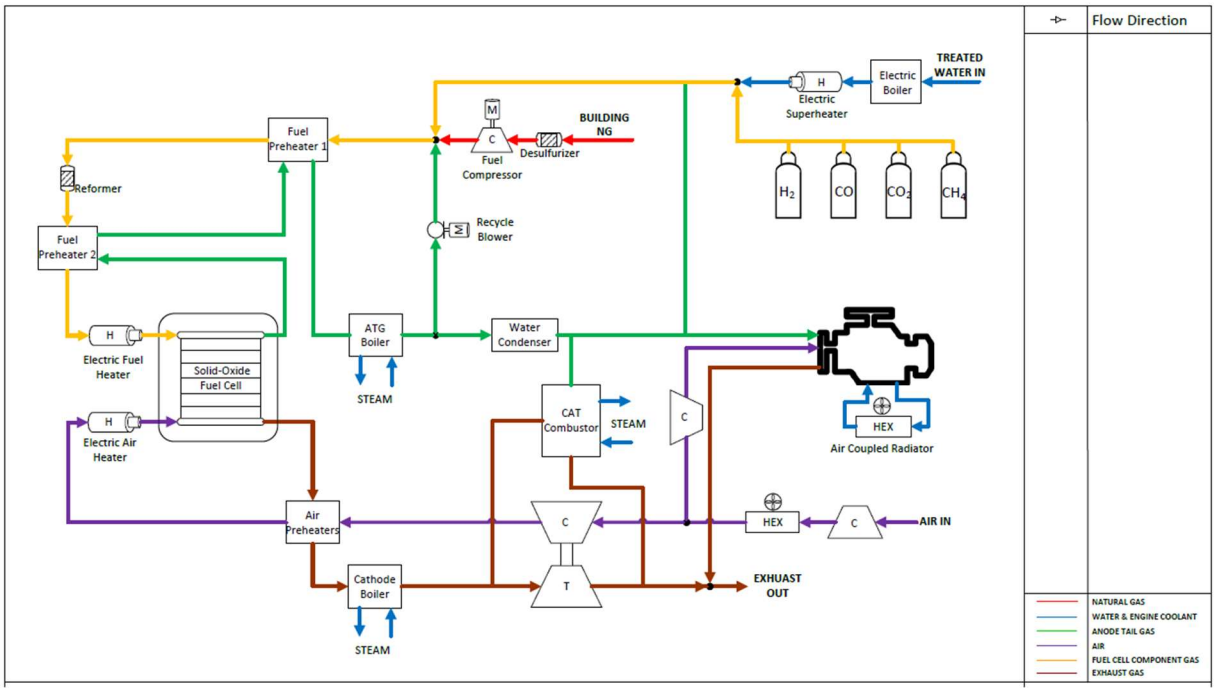

ICE hybrids. This system operates on both pipeline natural gas and hydrogen. The system processes and pressurizes air and fuel that is fed into the SOFC. The exhaust gasses from the fuel cell are partially recycled into the stacks and combusted in a specialized spark ignited ICE. The system is described further in Chapter 3; however, the general layout can be seen in Figure 2-3.

Figure 2-3: General layout of SOFC-ICE hybrid at CSU

The goal of this system is to evaluate a metal supported intermediate temperature system that could reach end markets [51], [52]. Mitchel et al. conducted research on this system with a focus on the high efficiency electrically driven air compression systems with heat recuperation [20]. Reyes-Flores et al. were able to successfully run this systems SI engine on a variety of fuel

blends based on the SOFC models. The results showed the SI engine could run on the fuel at efficiencies of 31%, projecting higher efficiencies with larger engines [19].

2.4: Pressurization Techniques for SOFCs

SOFC pressurization is an inherent quality of GT hybrid systems. These systems are most efficient when the compression system within the gas turbine is used to pressurize the fuel cells in addition to their function within the Brayton cycle. Much of the research is conducted with some form of this configuration [15], [37], [45]. These systems can differ in terms of execution, however, as microturbines, gas turbines, or turbochargers can be used within SOFC-GT hybrids [40], [42], [43], [44]

SOFC-ICE hybrid systems are not always designed with pressurization in mind. This is seen in several of the papers discussed in section 2.2.3. However, three configurations for a pressurized SOFC-ICE hybrid have been discussed in literature: engine attached turbochargers, combustor driven turbochargers, and electrically driven compressors. The most common of these is the use of a turbocharger that uses both engine and SOFC exhaust to drive the turbine. For example, Chuahy et al. used this method. This turbocharger generated 31.5 kW above what the compression process needed, showing that even under sub-optimal conditions this setup could reach necessary pressures. This turbocharger setup reduces the independence of the engine from the SOFC [45]

Rodriguez et al. modelled a system that used a separately run turbocharger that required the use of an ATG combustor when SOFC and reformation temperatures were low. This meant the turbocharger could operate independently of the engine, however, less fuel would be available for the engine [21].

Mitchel et al. evaluated the performance of the air BOP for a pressurized and moderate temperature 80 kW SOFC-ICE hybrid. This system utilized large positive displacement compressors and highly effective brazed plate heat exchangers to deliver air at flows of up to 100 g/s and 300 kPa (Figure 2-4). These devices operate using positive displacement compression, the scroll oscillates in a circular motion compressing the fluid in crescent shaped pockets gradually over several cycles. These devices can be quite efficient and reliable. The advantage of positive displacement devices over their turbomachinery counterparts is their wider operating ranges, which are not limited by surge and choke margins [53], [54]. Scroll compressors are typically used in smaller fluid delivery applications and their efficiency drops at larger scales. These devices were experimental in nature and have no comparable market equivalents. Mitchel et al. were able to

evaluate the air delivery capability of these devices for an SOFC, however, no turbine was used on the cathode exhaust, meaning that a significant amount of energy was lost [20].

Figure 2-4: Image of parallel scroll compressors in CSU system

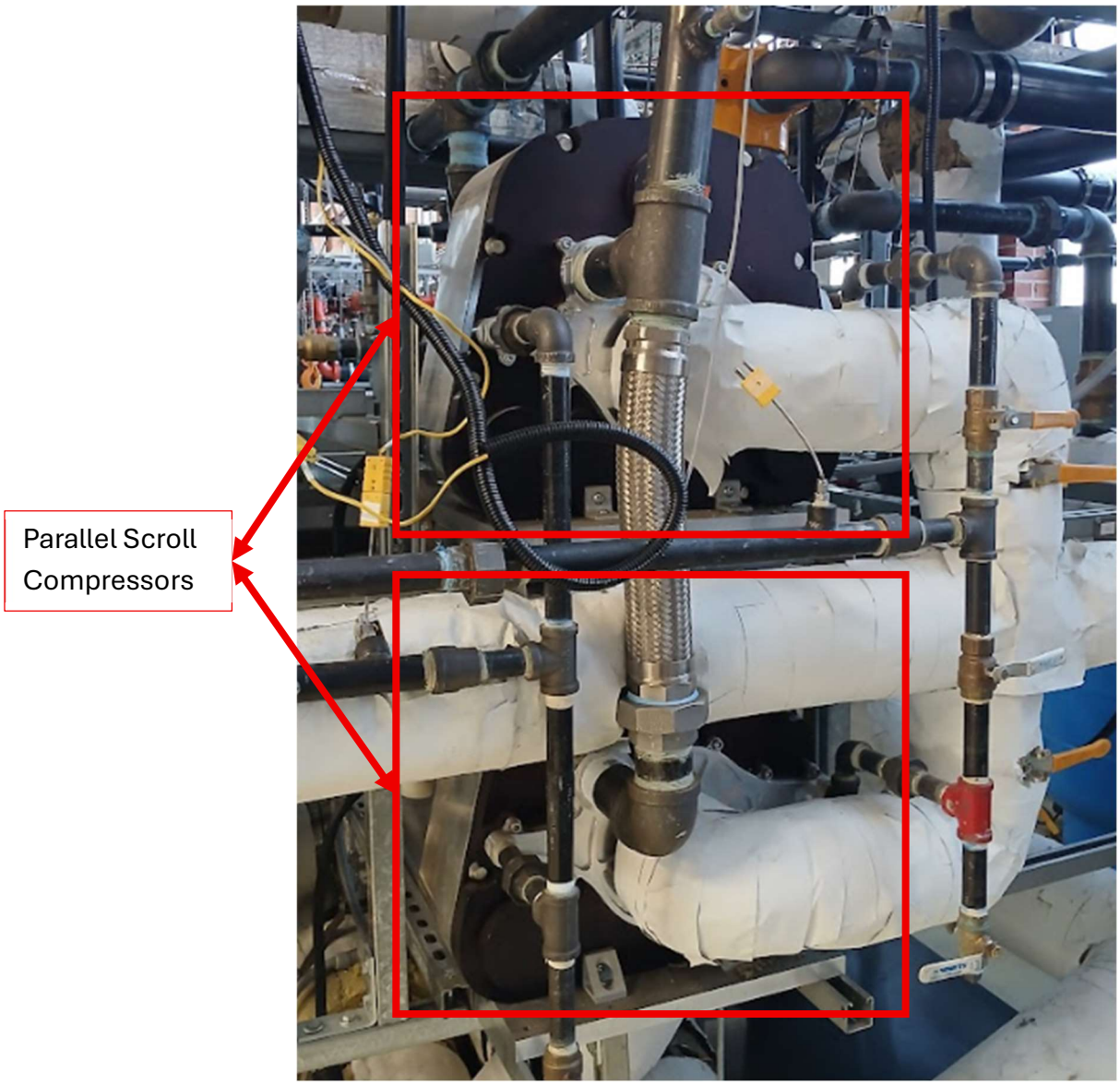

Mitchel et al. study found that major heat and pressure losses in the system significantly degraded overall delivery efficiency. The efficiencies of the compressor system peaked at 65% and this study called for evaluation of a turbine system to recover some of the enthalpy in the exhaust [20].

The present study's air system differs from the work done by Mitchel et al. because it does not incorporate the scroll compressors. Instead, it uses motored turbochargers. While traditional turbochargers and motored positive displacement machines have been explored as options, motored turbochargers are missing from the literature. Motored turbochargers are simple in concept as they follow the same principle as a traditional turbocharger or gas turbine. These devices add a motor onto the shaft. The motor can function to reduce turbo lag seen on automotive turbos. Motored turbochargers can also function, as is the case with this study, with the motor being the primary driver of compression. In the second case, the turbine provides load reduction for the motor which creates a more electrically efficient compressor [55], [56]. These devices can provide high compression efficiencies and low power consumption rates. Unlike turbochargers driven by engine or combustor products, these devices are much simpler to control and leave all the ATG available to the ICE.

While the operation of these motored turbochargers is simpler than turbine and turbocharger equivalents, they are still limited by several factors. Particularly, all turbomachines have surge and choke limits that constrict the operating range of the devices. Surging can be quite damaging, causing shocks and vibrations [54], [57]. These devices are also sensitive to inlet conditions, particularly the inlet temperature can cause issues in their performance. Increased inlet temperatures cause decreases in performance due to viscosity and density changes of the fluid [58], [59], [60], [61], [62], [63]. Typically, this results in needing to upsize the equipment when radical changes in density are expected [63]. If variable fluid properties exist due to a change in inlet conditions the blades must account for this in their profile or have the capacity to change angle [54].

2.5: Gaps in Literature and Focus of Current Investigation

To summarize the literature review provided above, SOFC technology provides a potential solution for lowering emissions of generation systems and addressing energy storage issues [4], [5], [7], [22], [64], [65], [66]. Unfortunately, this technology has struggled to penetrate the energy sector due to its high cost. These costs mostly originate from the expensive manufacturing processes, materials, and balance of plant necessary for the high operating temperatures [25], [26], [28], [29], [32]. Alleviating the high costs of SOFC technology has become a primary motivator of research in the last few decades. Improvements in SOFC technology have reduced the operating temperatures and increased the power density and efficiency using hybridization, pressurization, and material improvements [10], [13], [14], [18], [23], [31], [34], [67], [68]. In addition, researchers have seized the opportunity to combine the benefits of pressurization and hybridization, which have provided clear paths to efficiencies above 65% [15], [21], [23], [39], [45], [48], [49], [50]. The operating principles of gas turbines have made them a choice candidate for pressurized hybrids. This has resulted in most of the literature focusing on SOFC-GT systems. We now have ample understanding of the design, optimization and operation of several SOFC-GT hybrids, including the use of traditional gas turbines, turbochargers, and microturbines [15], [16], [36], [37], [38], [40], [41], [42], [43], [44]. However, SOFC-GT technology has still had difficulty entering the market. The desire for dispersed power systems at a smaller scale has been a difficult hurdle to surpass due to the limitations of gas turbines. While turbochargers and microturbines have been utilized to bridge this gap, they have lower efficiencies [36], [42], [43], [44]. To address this problem, research has shifted towards SOFC-ICE hybrids, which have several advantages over GT hybrids [45], [47], [50].

SOFC-ICE systems have the disadvantage of not being capable of performing the compression necessary on their own. This has resulted in literature focusing on either operating at

ambient pressure with a motored air blower, or the use of an automotive turbocharger tied to both the engine air and SOFC cathode [21], [45], [47], [48], [49], [50]. Full system modeling and experimentation of SOFC-GT systems has been studied extensively, however the same cannot be said for SOFC-ICE equivalents. Experimentation on the individual components, such as the cells, engine, and air BOP have been completed. However, the modeling of these systems has been done primarily with air BOP being set to assumed efficiencies. In addition, there are several other key categories of studies from literature. These are initially the use of intermediate temperatures, SOFC-ICE hybrid operation, pressurization, use of turbines, experimental validation, and full system analysis. These categories can be further broken down into the specific types of ICE, pressurization method, type of turbine, and what components were experimentally validated. As shown in Table 2-1 there has yet to be a single study which encompasses all these noted categories, let alone specifically tests spark ignited ICEs and motored turbochargers.

Table 2-1: Comparison table of previous research to this study

	Intermediate Temperatures	ICE	Pressurized	Turbines	Experimental Validation	Full System Analysis
Chuahy et al.		RCCI HCCI	TC	TC	Engine	✓
Choi et al.		HCCI			Engine	✓
Rodriguez et al.		NOS	TC	TC		✓
Williams et al.			GT	GT		✓
Araki et al.	✓		GT	GT		
Mitchel et al.	✓	SI	Motorized		Air BOP	
Reyes-Flores et al.	✓	SI	Motorized		Engine	
This study	✓	SI	Motorized	MTC	All Subsystems	✓

This study aims to bridge the gaps above by incorporating experimental data of components within the full system with a model to find an ideal operating point. Identifying the best operating condition is invaluable for maximizing the efficiency of SOFC-ICE hybrids. Optimizing these systems will provide higher returns on investment and lower emissions, making SOFC-ICE hybrids a more competitive alternative to traditional fossil fuel generation systems.

CHAPTER 3: TEST FACILITY AND EXPERIMENTAL METHODOLOGY

This chapter describes the test facility at Colorado State University and the tests undergone for this work. The testing section will include the function of components within and general layout of the testbench, and the testing procedure used to generate data that informed the model described in chapter four.

3.1: Facility Description

This work is supporting research for the overarching effort to develop a full scale 80 kW SOFC-ICE generation system. The test facility is being developed at Colorado State University under the ARPA-e INTEGRATE and DOE IEDO projects. This facility consists of a pressurized Ceres SOFC multi-stack module, a modified Kohler diesel ICE and support BOP.

The system operates using several sub systems which include the fuel BOP, air BOP, engine, and SOFC. The fuel system desulfurizes, pressurizes and preheats pipeline natural gas which is then pre-reformed to reduce the more complex hydrocarbons. The ATG produced by the stacks is cooled and steam removed before being used as fuel for the engine. The air system pressurizes and preheats air that is to be delivered to the cathode, the high temperature exhaust gases are used to preheat the inbound air before flowing through turbines. The engine is used as a bottoming cycle for the SOFC, burning the cooled ATG as a fuel. The SOFC itself internally reforms the fuel gas and produces electricity and heat.

The system is designed to achieve 80 kW with electrical efficiencies above 70% and CHP efficiencies approaching 80%. The system generates DC power through the stacks and the ICE attached to a generator. Some of the power generated is used to run the fuel compressor, air

compressors, valves, and other various small loads. The remainder is converted to AC via the inverter and dispersed to the grid.

The experimental focus of this work, the air compression system, was initially a pair of parallel scroll compressors designed to deliver air up to 100 g/s at 320 kPa [20]. However, the facility has shifted to two in series motored turbochargers due to demands for higher flows and efficiency. These devices deliver similar pressures to the scroll compressors with increased flow rates. The air preheating system, designed to bring the compressed air to necessary inlet temperatures of the stacks, is a series of two brazed plate heat exchangers, which have their specifications described in Chapter 4.

3.2: Turbocharger Test Bench

One of the project aims is to develop a high efficiency SOFC air delivery system and to display the viability of motored turbochargers. For this application the Fischer MTCT-120k-Air-Gen 4.2 was selected. SOFC technology has not penetrated markets, so there is limited selection of application specific motored turbochargers. This device is designed for lower temperature PEM cells but was the closest off the shelf design available. Initial designs of the system that include the Fischer device required two compressors in series; however, design limitations of the device mean that a few testing and design considerations must be acknowledged. One consideration is that the limits on axial load for the compressor bearings mean that testing the second stage with increased inlet pressures risks mechanical failure of the device. A second consideration is that the first stage raises the temperature of the second stage inlet over the maximum (Table 3-1), requiring an intercooler between compression stages. A similar consideration for the operating temperatures of the SOFC mean that the exhaust gases need to be cooled to the temperature limit of 120°C at the turbine.

Table 3-1: Specifications for Fischer MTCT-120k-Air-Gen 4.2

Specification	Values
Speed Range [RPM]	20000 – 110000
Max Corr. Mass Flow [g/s]	190
Max Pressure Ratio	3.15
Max Input Voltage to Inverter [VDC]	800
Max Compressor and Turbine Inlet Temperatures [°C]	50 : 120
Coolant Flow Rate [l/min]	8

A testbench was developed to characterize the Fischer device for the second stage compressor conditions and the increased turbine inlet temperatures (Figure 3-1). The testbench sets the turbine inlet at an elevated temperature of 115°C, which was selected to provide a small safety buffer below the limit. To determine performance of second stage compression the temperature of the inlet was matched with the intercooler outlet, but the pressure was set to 101 kPa to stay within axial load limits.

It was determined that testing the device without increasing pressure above 101 kPa would still provide data that would inform the model. It is well established that performance derating of turbomachinery is primarily due to density decreases alongside smaller derating effects from viscosity increases. The primary consequence of decreased density and increased viscosity is the speed increase of the turbomachinery required to drive the same mass flow. [58], [59], [60], [63]. Density increases with pressure, and the viscosity increase from 1 to 2 bar is negligible. The higher density from increased pressure would only slow the compressor speeds which results in less losses and higher efficiencies [54]. Therefore, operating at increased temperatures without increasing the pressure will not result in performance overestimation of the second stage compressor.

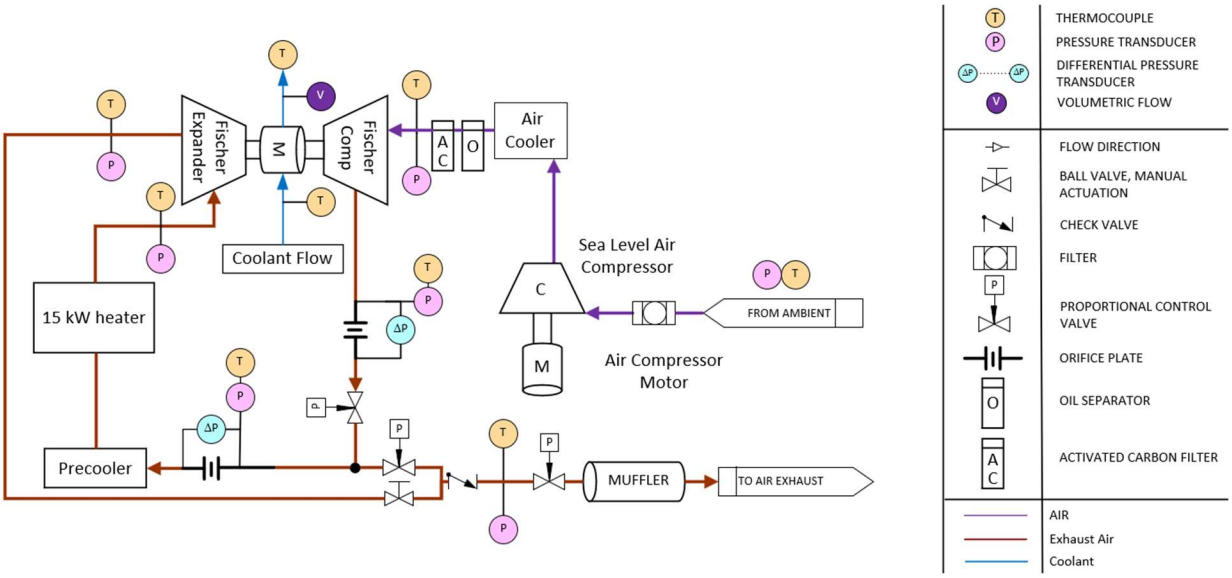

Figure 3-1: Test bench diagram

A ROOTS Universal RAI-J WHISPAIR positive displacement blower compensates for the reduced northern Colorado atmospheric pressure while also increasing the air temperature. The blower is placed in a noise insulating box and is coupled to an air cooler. It is controlled by a PID controller that targets the measured pressure at the inlet of the Fischer compressor. The compressed inlet air is cooled to keep the conditions close to 38°C and then flows through a series of filters before arriving at the compressor inlet. The filters consist of a particulate and oil filter in series to provide the Fischer device and SOFC with protection from debris and potential chemical degradation. The pressure ratio of the compressor is controlled by the speed of the motor and a proportional control valve (Figure 3-2).

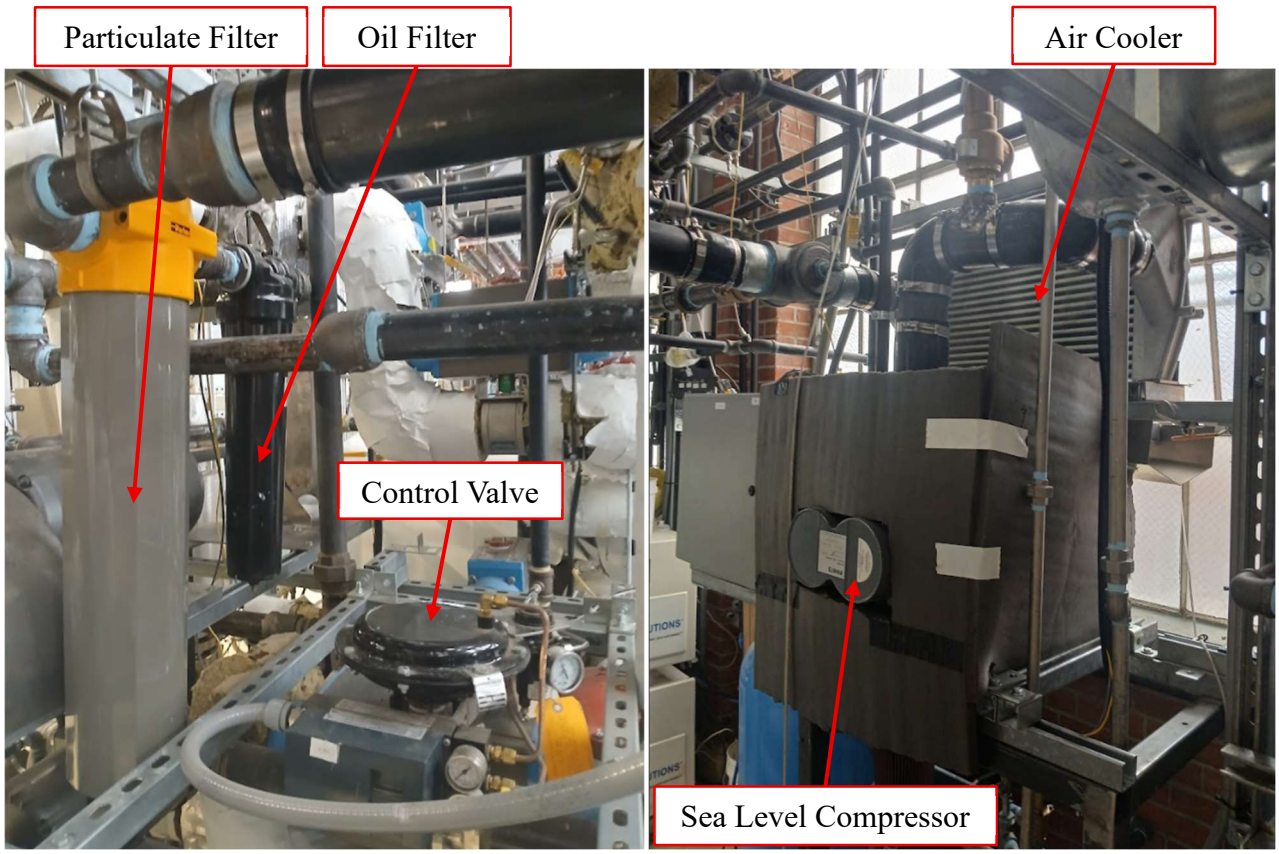

Figure 3-2: Photos of SL compressor, air cooler, filters and proportional control valve

The pressurized air is circulated to the turbine, running through a precooler before being heated to the turbine target temperature (Figure 3-3). The heater is a 15-kW electric resistance heater, which is controlled within LabVIEW, with the target temperature set by a thermocouple at the turbine inlet. The precooler is necessary to avoid exceeding this temperature limit when compression ratios are high. A bypass is in place to route a percentage of the airflow around the turbine if choked flow occurs (Figure 3-4). The air then flows to the exhaust; however, the exhaust air is released through a proportional valve that regulates the outlet flow pressure to 101 kPa. This is done to more accurately emulate sea level conditions. Without regulating the exhaust pressure, the turbines would have more available pressure ratio, which would result in overestimation of performance.

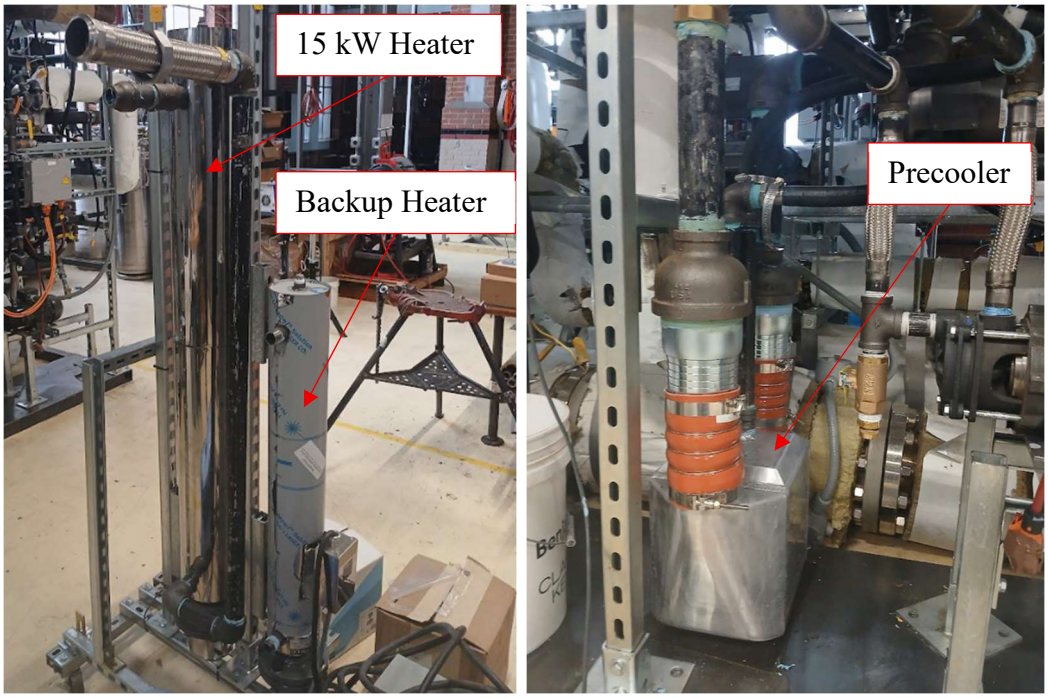

Figure 3-3: *Heater cart and pre-cooler*

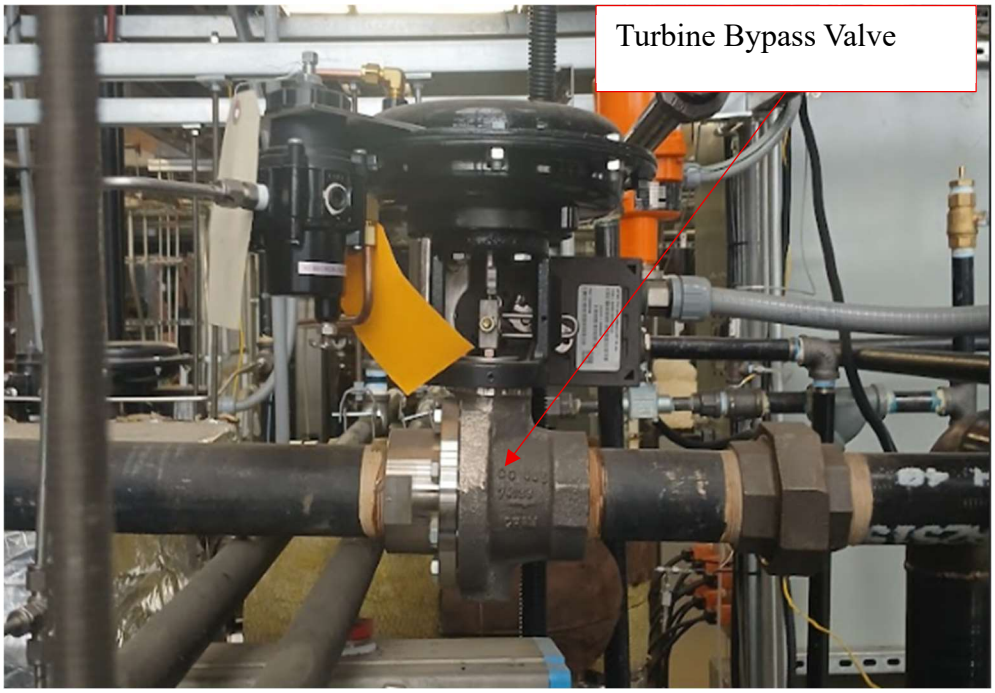

Figure 3-4: Turbine bypass valve

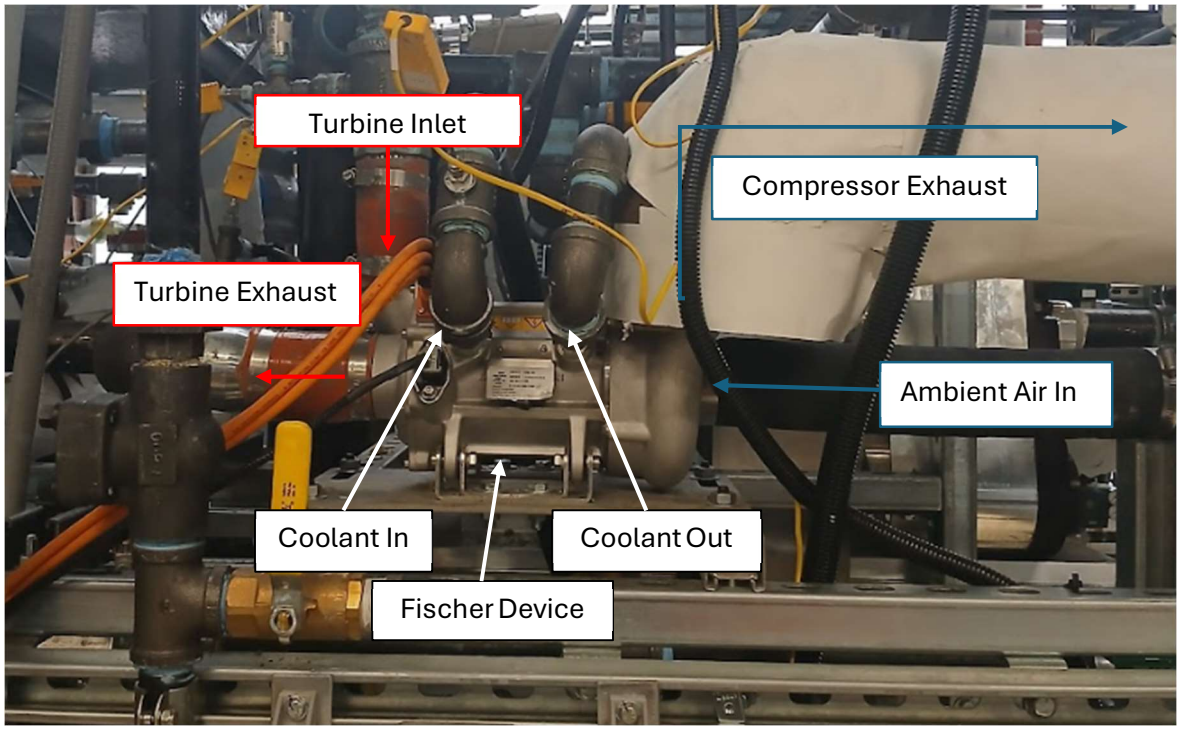

Figure 3-5: Fischer compressor within test bench

The device's performance is characterized by using the data collected from instruments (Table 3-2 and Figure 3-5) and the readings from the Fischer device itself. Which has power supplied by an inverter manufactured by Fischer (Figure 3-6). The uncertainty of the speed and power readings of the Fischer device were not provided by the manufacturer. The instruments within the piping and at the inlet and outlet of the compressor and turbine provide temperature, pressure, and pressure differential data.

Table 3-2: Instrument details

Instrument Type	Uncertainty	Range
K Type Thermocouple	±2°C or 0.75%	0-1250°C
K Type Coolant Thermocouple	±0.073 and 0.0996 °C	5-90°C
Differential Pressure Transducer	± 0.1275 kPa	0-20 in.wg
Pressure Transducer	± 0.25 %	0-50 psi
Volumetric Flow Meter	± 0.8 %	0-50 LPM

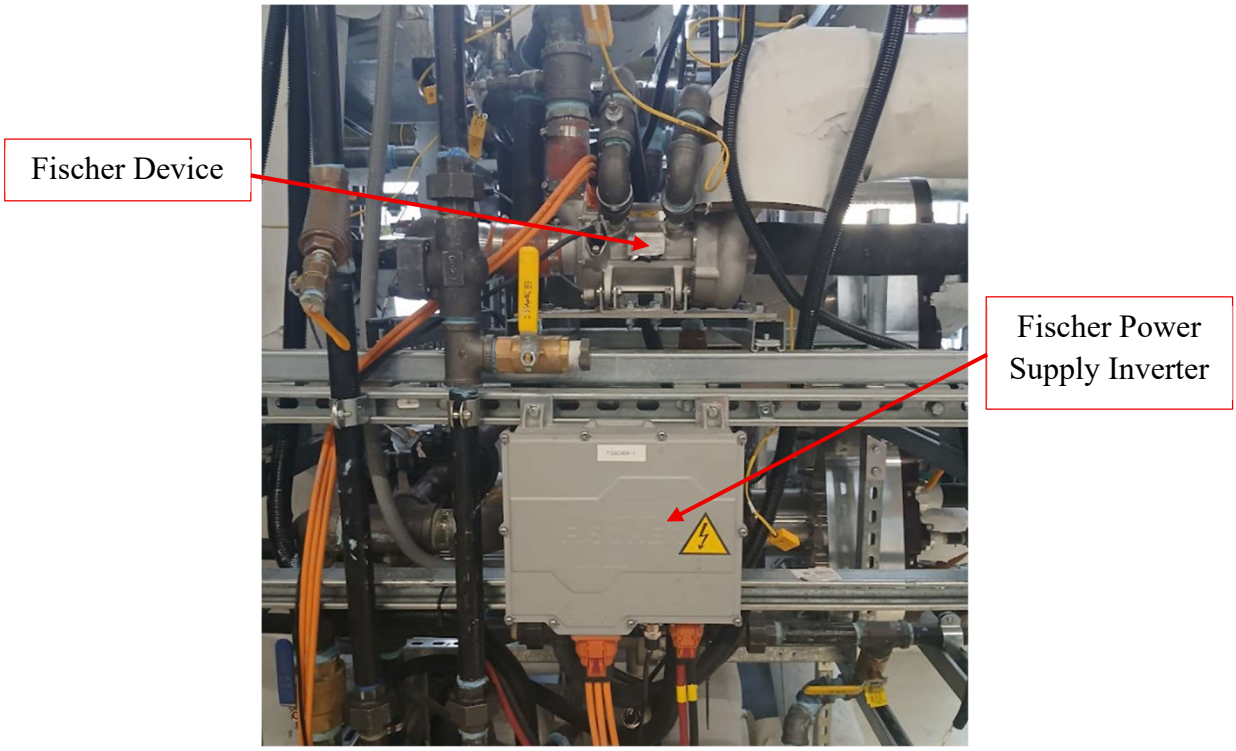

Figure 3-6: Fischer power supply inverter & Fisher device

This data can be used in conjunction with instream orifice plates for calculating mass flow for both controls and characterization. The orifice plates for the lower flow tests (<70 g/s) were performed with two 1.4375" orifice plates, which was later increased to 1.70" for the higher flow tests, with the formula for calculating mass flow with these orifice plates being found in "Orifice Metering of Natural Gas and Other Related Hydrocarbon Fluids, Part 1" [69]. Engineering Equation Solver (EES) was used to calculate the uncertainty of the data using equation 3-1, the standard method of error propagation. EES was also used to calculate the performance of the compressors, with all state point thermodynamic properties found using its internal property tables. The equations for these calculations are found in the modelling section [70].

$$u_c(y) = \sqrt{\sum_{i=1}^{N} \left(\frac{\delta f}{\delta x_i}\right)^2 u^2(x_i)} \qquad 3\text{-}1$$

To capture the heat rejection rate from the device to the coolant, a volumetric flow meter and thermocouples were placed within the coolant stream. The coolant thermocouples were

calibrated to a higher degree of accuracy to account for the smaller changes in temperature of the coolant. The coolant system uses 30/70 propylene glycol, and flows through the compressor, pre-cooler, and Fischer inverter in addition to the other systems of the facility. The system pumps coolant through several flow control valves, to different subsystems, however, all heat is rejected in a 100-kW rated radiator outside the test facility (Figure 3-7).

Figure 3-7: Coolant system radiator

3.3: Testing Approach

Two test plans were completed to characterize the device (Figure 3-8). The blue line represents the tests of both the compressor and turbine across the range the second stage compressor is anticipated to operate at. The red line represents the tests in the middle of the blue range that only included the compressor with the turbine fully bypassed.

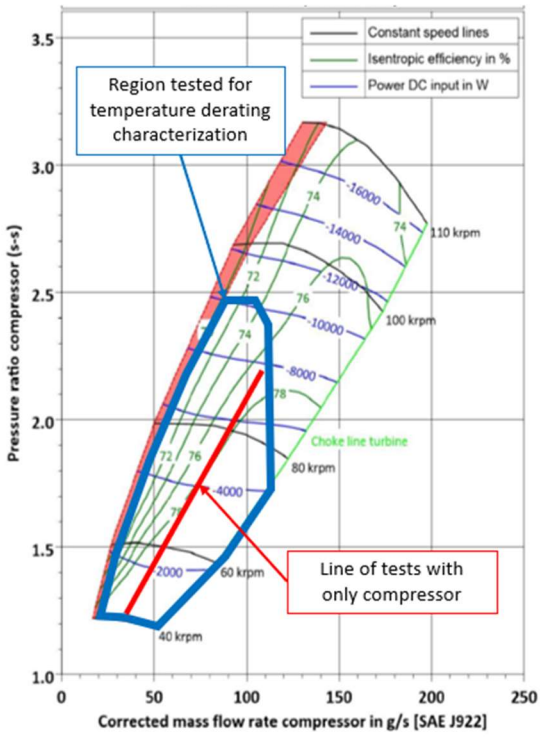

Figure 3-8: Manufacturer compressor map and test ranges

The purpose of this second category of tests was to ascertain the heat transfer rate from the turbine to correct the initial >100% efficiencies found at low motor speeds. The tests in both categories were done in increments of 5 g/s and 0.1 pressure ratio. Each test was run at steady state with instrument data recorded at 1 Hz for 2 minutes and averaged. The data was collected and analyzed to inform the modeling as described in Chapter 4.

CHAPTER 4: MODELING METHODOLOGY

This chapter contains a description of the model used in this study. It is split into three main sections that cover the general full system model, the Colorado School of Mines model, and the CSU air delivery system model.

4.1: Full System Model Description

The previous chapter and several studies have described the CSU 80 kW SOFC/ICE hybrid system in detail [19], [20], [52]. For this study, however, a simplified model of the system was developed to explore a range of air BOP operating conditions as shown in Figure 4-1.

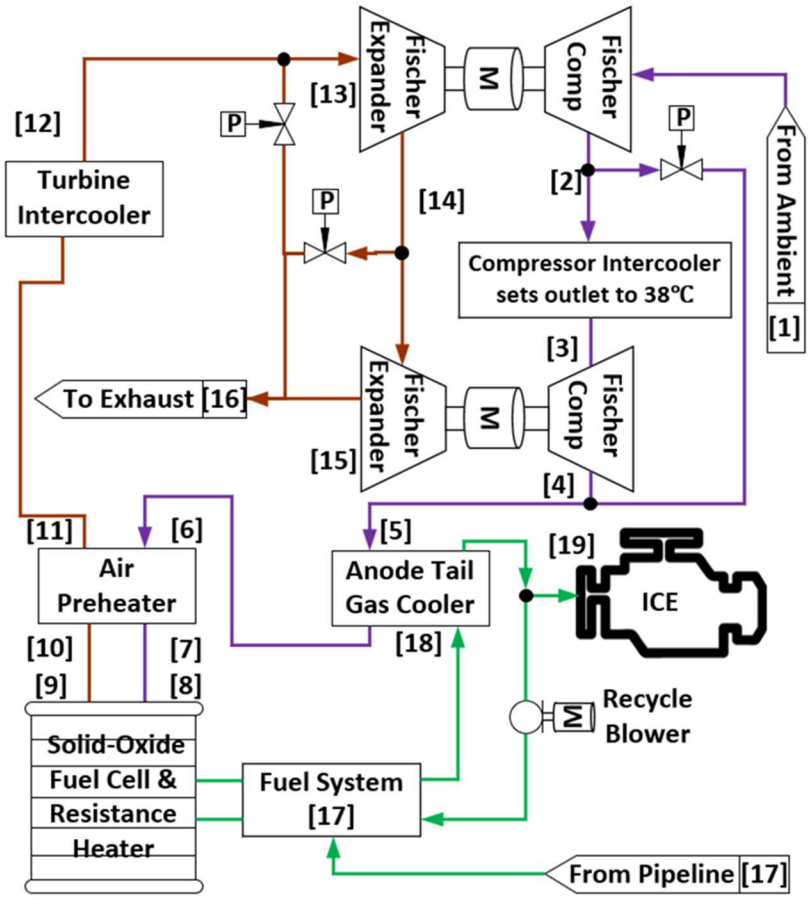

Figure 4-1: Full system model diagram

The model contains two distinct portions developed in cooperation between CSU and CSM. The first portion of the model was developed by CSM and includes the SOFC, ICE, and fuel BOP parasitic load. The second portion of the model was developed by CSU in EES and includes a parametric study of the motored turbochargers that includes the thermodynamics of the piping, heat exchangers, and turbomachinery.

4.2: Colorado School of Mines Model: SOFC, ICE and Parasitic Load

The SOFC in this system uses three multi stack modules (MSM), each containing 4 Ceres Power stacks. Each stack consists of 250 cells that each have an area of 194.9 cm^2 each. The CSM model has all 3 stacks modeled independently for their thermal, flow, and electrochemical operation. The model is built on both manufacturer data and experimental data conducted at CSM. The maldistribution of gases to each stack is accounted for with the flows benchmarked against COMSOL CFD models of the stacks. The engine, parasitic loads, and fuel BOP systems are modeled with efficiency curves from the equipment within the test site [17]. The range of fuel cell conditions for this study were input into the CSM model to evaluate the cell efficiency, power production, heat release, and pressure drop. The three model variables: pressure, air flow, and current had their ranges selected based on previous modeling and experimental data from CSM for the analysis of the stacks in the 70-100 kW range and can be seen within Table 4-1 [12], [18].

Table 4-1: SOFC operating parameters for model

Condition	Values
Pressure of Air at Cathode Inlet	200-300 kPa
Mass Flow of Air to Cathode	80-120 g/s
Operating Amperage of Fuel Cell	35-40 Amps
Outlet Temperature of Cathode	630 °C
Fuel Utilization: Anode Recycle Rate	70 % : 30%
Fuel Composition	84% CH_4, 12% C_2H_6, 4% CO_2

4.3: Colorado State University Air Balance of Plant Model

For the CSU portion of the model, several system assumptions were made as shown in Table 4-2 with their respective state points numbered in Figure 4-1.

Table 4-2: State points that include assumptions

State Point Number	Name	Assumed Value
1	Stage One Compressor Inlet	101 kPa : 22°C
3	Compressor Intercooler Outlet	38°C
9	Stack Cathode Exit Temperature	630°C
13	Turbine Stage One Inlet	115°C
16	Exhaust	≥101 kPa
17	Fuel Flow From BOP	Ranges to meet other conditions
18	Anode Tail Gas Cooler Hot Side Inlet	275°C: Pressure Set to Same as Air Side

The first stage compressor inlet temperature and pressure were set at 22°C and 101 kPa, respectively, to match with the Fischer provided compressor maps. The intercooler of the compressors was assumed to produce a consistent 38°C outlet temperature which was matched with the experimental results. The fuel cell's outlet temperature was set at 630°C, with a set utilization and anode recycle rate. The fuel pressure and flow rate are allowed to vary to ensure the set states are conserved. The air BOP EES model can be split into three portions, compression, heat exchangers and pipe losses, and expansion and exhaust.

4.3.1: Compression

The compression portion of the model includes the pressurization of air in one or two stages with intercooling. For this study, the air flow rate varied between 80 g/s and 120 g/s at an increment of 10 g/s while the fuel cell inlet pressure varied between 200 kPa and 300 kPa in increments of 20 kPa. The first step was to select an air flow rate and pressure ratio within the expected ranges

and calculate the target compressor outlet pressure which is determined by the piping and component pressure losses (described in next section). The inlet conditions at state 1 are used in equation 4.1 to calculate corrected mass flow, which is then used to interpolate the manufacturer map (Figure 3-8) for efficiency. The outlet pressure, compressor efficiency, and power consumption are calculated using equations 4.2, 4.3, and 4.4. The enthalpy and temperature values are determined from EES's internal property tables.

$$\dot{m}_{\mathrm{corr}} = \frac{\dot{m}\sqrt{\frac{T_{\mathrm{i}}}{298\mathrm{K}}}}{\frac{p_{\mathrm{i}}}{1\ \mathrm{bar}}} \tag{4.1}$$

$$p_{\mathrm{o}} = p_{\mathrm{i}} \times PR \tag{4.2}$$

$$\eta_{\mathrm{c}} = \frac{(h_{\mathrm{o,s}} - h_{\mathrm{i}})}{(h_{\mathrm{o}} - h_{\mathrm{i}})} \tag{4.3}$$

$$P_{\mathrm{c}} = \dot{m}(h_{\mathrm{o}} - h_{\mathrm{i}}) \tag{4.4}$$

If the target pressure is achieved with one stage, the second compressor is bypassed. If not, the temperature at the inlet of stage two is set to 38°C by the intercooler, and equation 4.1 is used again with the new inlet conditions. The second stage corrected mass flow and pressure ratio are used to interpolate over the experimentally generated map (Figure 5-1). Equations 4.2-4.4 are used to calculate the final compressor outlet pressure, temperature, and power consumption. The logic for the compressor model is represented by a diagram in Figure 4-2 for clarity.

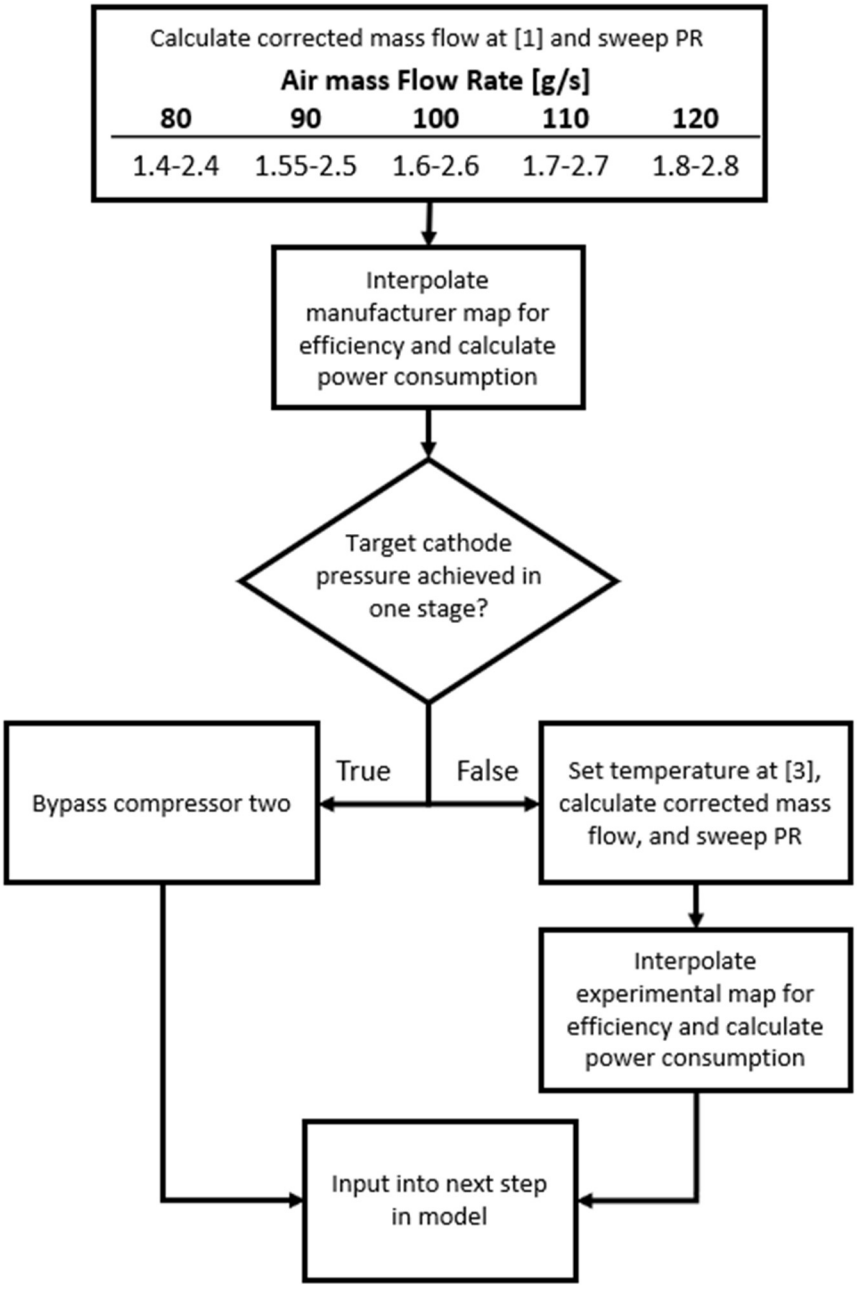

Figure 4-2: Air compression model flowchart

4.3.2: Heat Exchangers and Pipe Losses

The temperatures of the gases in the air system are important for calculating the pressure losses in the system. The pressure losses are vital for understanding the turbomachinery

performance of the system because higher flowrates and/or lower pressures will increase pressure drop, requiring more power to reach target pressures.

After the air compression is complete, the air flows through piping and two counterflow brazed plate heat exchangers (HEX), the anode tail gas (ATG) cooler and the air preheater, before reaching the fuel cells. The performance of the HEX was modeled and evaluated by Mitchel et al. and this model bases its heat transfer calculations on their work [20]. The HEX specifications can be seen in Table 4-3.

Table 4-3: Heat exchanger specifications

Specifications	Air Preheater	ATG Cooler
Height [mm]	350	129
Length [mm]	613	613
Width [mm]	186	186
Number of Plates	140	48
Heat Exchanger Surface Area [m^2]	12.85	4.35
Fluid Hot Side	Exhaust Air	Anode Tail Gas
Fluid Cold Side	Inlet Air	Inlet Air

The cold inlet condition (state [5]) to the ATG cooler was determined from the previous compressor model, but the hot inlet condition (state [18]) was set from the CSM model at 275°C. Similarly, the hot inlet condition (state [10]) was determined by setting the conditions at state [10] to 630°C. The pressure of the gas streams was set to match the outlet of the compressor after subtracting calculated pipe pressure drops. The flow rate of the ATG was averaged for all cases, and the exhaust air flow rate is assumed to be ~90% of the flow rate of the inlet air.

The performance of the heat exchangers is evaluated using the Effectiveness-NTU (ε-NTU) method and is modeled in four parts to enhance accuracy (Figure 4-3).

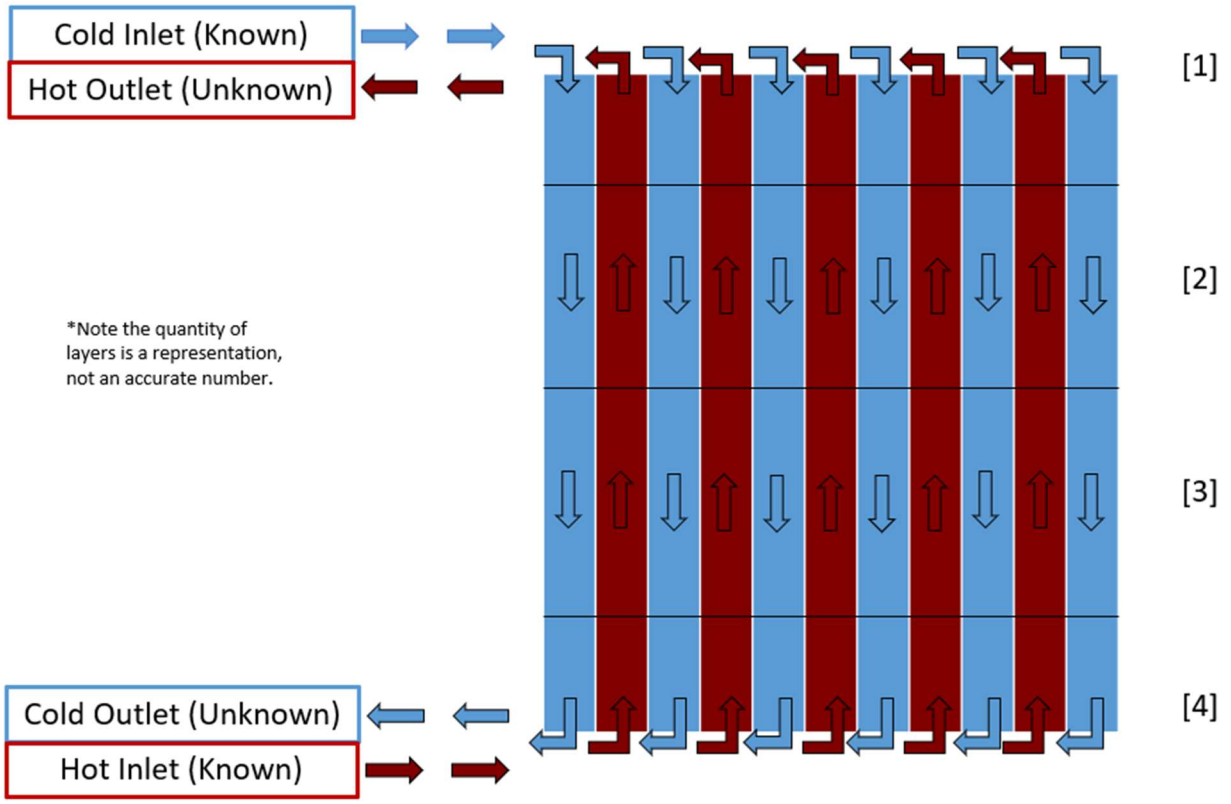

Figure 4-3: HEX model representation

Each portion is calculated using the prior states conditions, with the flowrates determined by the turbomachinery upstream of the HEX. To perform the ε-NTU method, the values for *NTU* and ε need to be calculated, which are done with equations 4.5, 4.6, and 4.7 [71].

$$NTU = \frac{UA}{C_{min}} \tag{4.5}$$

For counterflow HEXs where $C_r < 1$

$$\varepsilon = \frac{(1-\exp[-NTU(1-C_r)])}{1-C_r \exp[-NTU(1-C_r)]} \tag{4.6}$$

$$\varepsilon = \frac{q}{q_{\max}} \tag{4.7}$$

The area is pre-determined by the specifications sheet, however, U and $C_{\min}$ need to be determined. $C_{\min}$ is calculated using EES property tables and Equations 4.8, 4.9, and 4.10.

$$C_{cold} = \dot{m}_{cold}\left(C_{p,cold}\right) \tag{4.8}$$

$$C_{hot} = \dot{m}_{hot}\left(C_{p,hot}\right) \tag{4.9}$$

$$C_r = \frac{\min[C_{cold}, C_{hot}]}{\max[C_{cold}, C_{hot}]} \tag{4.10}$$

U, the overall heat transfer coefficient of the HEX, is calculated using Equation 4.11.

$$U = \frac{1}{\left[\frac{1}{\bar{h}_{cold}} + \frac{t_{plate}}{k_{plate}} + \frac{1}{\bar{h}_{ho}}\right]} \tag{4.11}$$

The convective coefficients denoted h are calculated using the Wenzhe and Pega correlation in Equation 4.12. The values for the thickness and conductivity of the plates within the HEX are provided within its data sheet [72], [73].

$$\overline{Nu} = \frac{\overline{h_f} D_h}{k_f} = 0.2913(Re_{ch}^{0.702}) \left(\frac{\mu_f}{\mu_w}\right)^{0.14} \left(\mathrm{Pr}_{\mathrm{f}}^{\frac{1}{3}}\right) \tag{4.12}$$

The subscript f denotes the specific fluid whose properties are being calculated. The Reynolds number (Re_{ch}) is calculated in Equation 4.13, the thermodynamic properties of the fluid are provided by property tables within EES, and the hydraulic diameter (D_h) is provided from information within the datasheet. The pressing depth and width are also pulled from the datasheet for Equation 4.13.

$$Re_{ch,f} = \frac{2\dot{m}_f}{Pressing_{depth}(w)\mu_f} \tag{4.13}$$

Finally, q_{max} is calculated using Equation 4.14, which enables the calculation of the HEX heat transfer rate and outlet temperatures of each state point using Equations 4.7 and 4.15.

$$q_{max} = C_{min}\left(T_{h,in} - T_{c,in}\right) \tag{4.14}$$

$$T_{out,f} = \frac{q}{C_f} + T_{in,f} \tag{4.15}$$

The pressure drop across the HEX was calculated using the same 4 step model using the Neagu correlation (Equation 4.16). This will be added to the pipe pressure drops calculated later in this section.

$$\Delta P_{ch} = 4f\left(\frac{\rho u^2}{2}\right)\left(\frac{L}{D_h}\right) \quad (4.16)$$

The pipe pressure losses are modeled in five locations across the system: compressors to heat exchangers, heat exchangers to cathode inlet, cathode outlet to air preheaters, air preheaters to turbine inlet, and turbine outlet to exhaust. These losses are used to determine the pressure ratio at the outlet of the compressors, since the inlet to the fuel cells is set.

The pipe losses are evaluated using Equations 4.17 (Colbrook Equation), 4.18 (Minor Losses), and 4.19 using the specific pipe inlet conditions. The Colbrook equation is selected for pressure drop due to the turbulence being high, which was evaluated using Equation 4.20. Minor loss coefficients for the pipe fittings, such as elbows and tees, are determined by manufacturer values for each component.

$$\frac{1}{\lambda} = -2\ln\left(\frac{2.51}{Re\times\sqrt{\lambda}} + \frac{e}{D}\times 0.269\right) \quad (4.17)$$

$$h_{\mathrm{L,minor}} = K_{\mathrm{tot}}\left(\frac{\mu_{\mathrm{air}}^2}{2g}\right), K_{\mathrm{tot}} = \sum n_{\mathrm{i}}k_{\mathrm{i}} \quad (4.18)$$

$$\Delta P = \frac{\lambda L\rho}{2D}\omega^2 + h_{\mathrm{minor}} \quad (4.19)$$

$$Re_{pipe} = \frac{\rho_{air}v_{air}D_{pipe}}{\mu} \quad (4.20)$$

The pressure drop is used to determine the compressor outlet pressure and pressure ratio for a given target pressure. For example, if the target is 300 kPa, the drop may require the compressor to bring the air to 320 kPa to achieve the target.

4.3.3: Turbines

The final section of the CSU modeling effort is the gas expansion through the turbine. After the exhaust air from the fuel cells has passed through the air preheater it goes to a liquid cooled turbine intercooler where the outlet condition is assumed to be 115°C, with the pressure set by the pipe and heat exchanger losses. The logic for expansion is substantially more complex than compression, as the performance limits are more stringent (Figure 4-4).

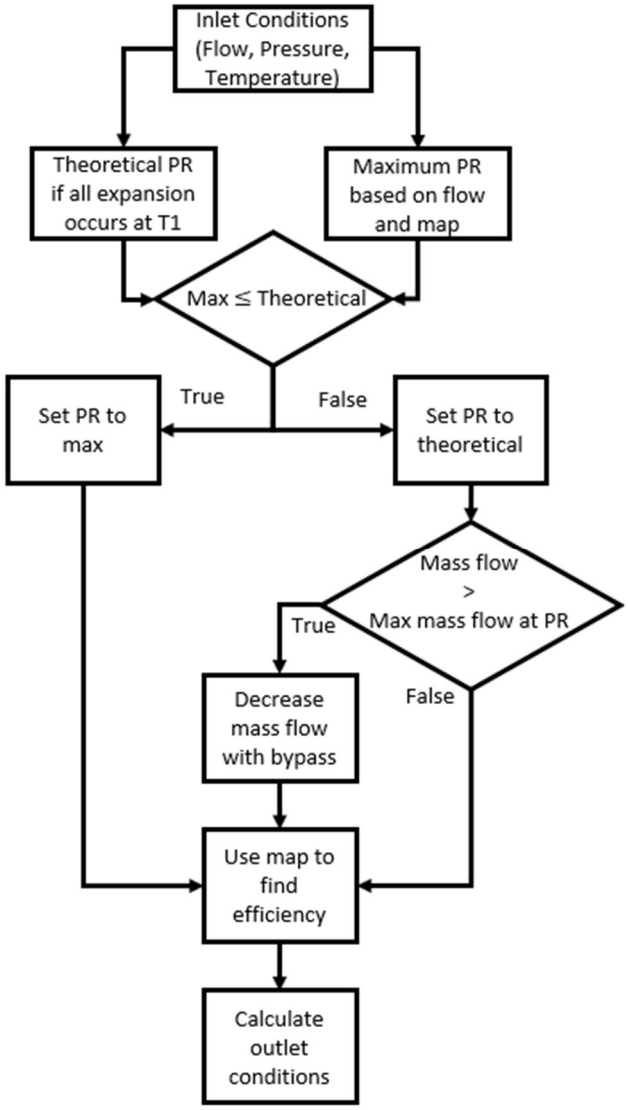

Figure 4-4: Turbine model flowchart

The inlet temperature and pressure were used to calculate a reduced mass flow rate (Equation 4.21), which was used to interpolate several tables based on the experimental and manufacturer data.

$$\dot{m}_{\text{reduced}} = \frac{\dot{m}_{\text{t}}\sqrt{T_{\text{i}}}}{P_{\text{i}}} \tag{4.21}$$

First, a table that establishes the range of pressure ratios available to the reduced flowrate is checked. The maximum pressure ratio from this range was used to check if the outlet pressure of the exhaust after pressure losses is below 101 kPa. If the pressure was below, the pressure ratio

that does not result in a sub 101 kPa pressure was selected and the second turbine is bypassed. If the pressure was above 101 kPa, the pressure ratio was set by the flow rate, and the second turbine is not bypassed. To calculate the pressure ratio from the flow rate, the reduced flow was compared to the range of available flowrates for the supplied inlet pressure. If the mass flow exceeds the maximum, the flow was set to the maximum for that pressure and the remaining flow bypasses the turbine.

With the pressure ratio selected, the experimental turbine curve was interpolated for the efficiency and the outlet conditions such as power generation, pressure, and temperature which were calculated using equations 4.22 and 4.23.

$$\eta_t = \frac{(h_{\mathrm{o}} - h_{\mathrm{i}})}{h_{\mathrm{o,s}} - h_{\mathrm{i}}} \tag{4.22}$$

$$P_{\mathrm{t}} = \dot{m}_{\mathrm{t}}(h_{\mathrm{o}} - h_{\mathrm{i}}) \tag{4.23}$$

In many cases, the first stage of the turbine was available because the first stage did not reach an outlet condition of 101 kPa. In these cases, the same procedure is followed for the second stage, however, the efficiency is referenced from the manufacturer curve due to the lower inlet temperatures at the second stage. Finally, the model subtracts the turbine power generation from compressor power consumption, and accounts for a combined motor and electrical efficiency of 86% as measured in testing. A minimum power consumption of the Fischer devices is found for each of the combinations of air flow rate and cathode inlet pressure. The power consumption of the compressor-turbines is added to the CSM model data which provides total system efficiency and power output.

CHAPTER 5:RESULTS AND DISCUSSION

5.1 Experimental Results

5.1.1: Compressor Results

The results of the experimental testing for the compressor are shown in Figure 5-1.

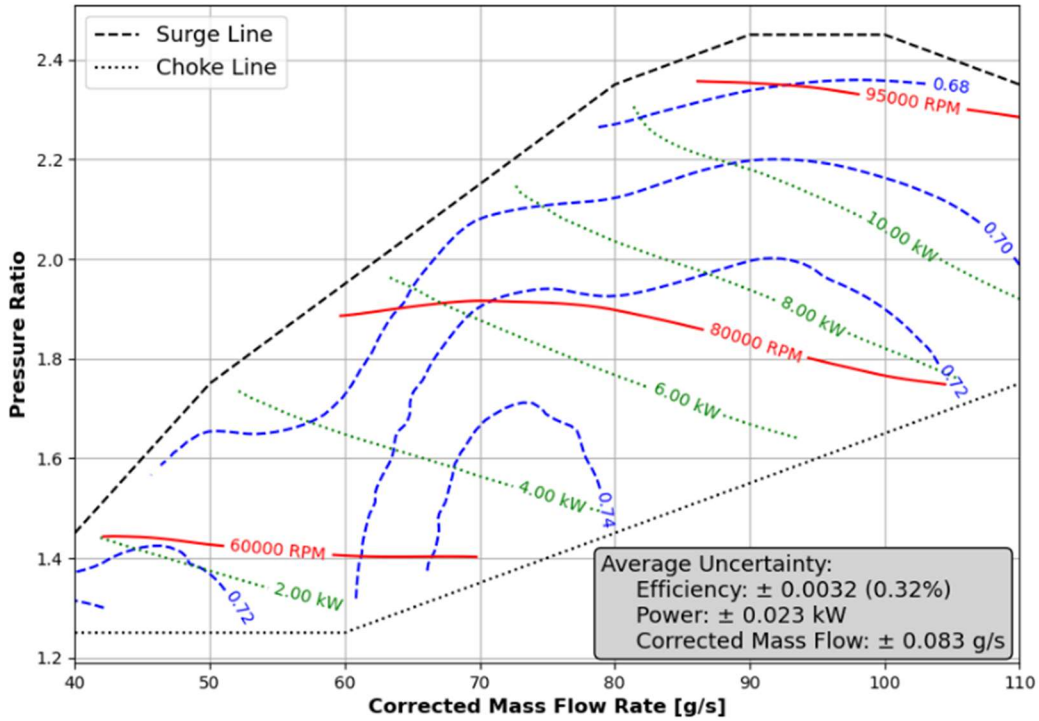

Figure 5-1: Experimental Fischer compressor map

During these experiments, the compressor inlet temperature varied ±3°C around the 38°C target due to typical summer temperature variation in Colorado. This required the use of ambient temperature corrections. Using the analytical method found in the work of Smith et al, the data was able to be adjusted for the variations in temperature. A reference temperature of 38℃ was selected, before the stagnation pressure, density, temperature was calculated using the standard air assumptions for specific heat ratio and gas constant. These values are then used to calculate the new corrected pressure ratios, which smooth the curves for each flowrate significantly[74].

The higher ambient temperature caused several differences between the manufacturer provided map and the experimentally generated map. The corrected speed lines matched the manufacturer map, however, the real speed reached the 110,000 RPM speed limit without reaching the expected pressure ratios and flows. This is due to the difference in density at the elevated inlet temperature resulting in a higher speed. The compressor could not exceed a speed of 110,000 RPM, indicating the max motor power was reached, and the turbine was not producing enough work due to restricted flows described in the next section. The increased inlet temperature likely restricts the operating range of the compressor and results in a decrease in compressor efficiency between 2 and 4%. In addition, the peak efficiency island shrunk significantly and moved to lower flow rates and pressure ratios. This is likely caused by a decrease in gas density with the temperature rise, so the compressor must spin faster to achieve the same target pressure. Because the compressor was designed to operate at a specific range of conditions for a given speed, a large deviation from this island will result in efficiency losses [58], [59], [60].

5.1.2: Turbine Results

The turbine results initially showed >100% efficiencies at lower speeds and pressures because of heat rejection to the coolant and through the housing to the surroundings. Previous turbocharger research by Sirakov et al. found that a single heat rejection rate was sufficient when low speed efficiencies are skewed for turbochargers, so the same is assumed in this study for the motored turbocharger [75]. Using the data from the isolated compressor tests (red line on Figure 3-8), an average heat rejection rate across the map was calculated by using the measured coolant temperatures and flow rate as shown in equation 11 [47]. The ratio of heat rejected to motor work for isolated cases is used to calculate the motor heat rejection of the turbine inclusive tests under the same compressor conditions. The difference between the calculated motor heat production rate

and the measured heat rejection provides a near constant value that averages out to 422 W. For equations 5.24 and 5.25 subscript C denotes compressor only, and CT denotes compressor and turbine test. The corrected results can be seen on a turbine efficiency curve in Figure 5-2.

$$Q_{\text{rejected}} = \dot{m}_{\text{coolant}} cp_{\text{coolant}} \left(T_{\text{coolant,out}} - T_{\text{coolant,in}}\right) \tag{5.24}$$

$$Q_{\text{turbine}} = Q_{C,CT} - \left(\frac{Q_{\text{C,C}}}{W_{\text{motor,C}}}\right) W_{\text{motor,CT}} \tag{5.25}$$

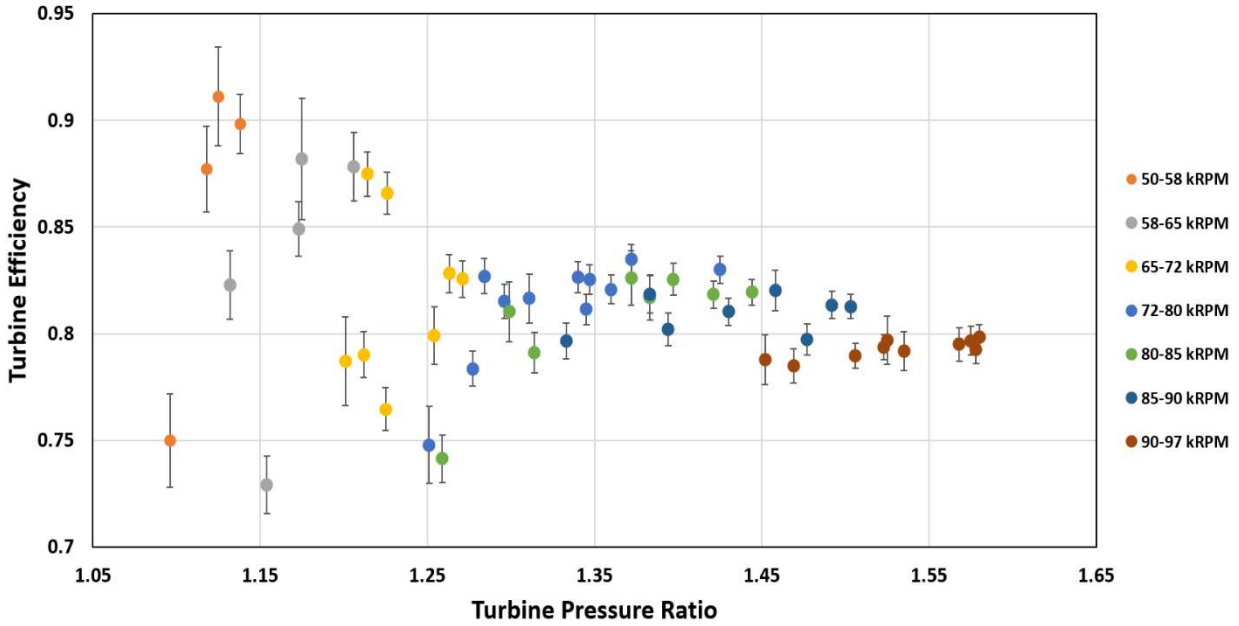

Figure 5-2: Turbine efficiency curve

The reduced mass flow rate and efficiency were calculated using experimental data and equations 4.21 and 4.22, respectively. The efficiency data (Figure 5-2) showed the development of speed curves for the turbine, which are color coded in the figure. However, the curves are not ideal, with some wide variations occurring. These can be explained by variations in the mass flow. The high flow low pressure cases are operating far off the turbine curve. The turbine speed, being independent from turbine flow because the turbine is attached to the same shaft as the compressor, results in speeds much higher than what would be necessary for the pressure ratio available. Overexpansion occurs before the pressure transducer in this process, resulting in greater instabilities and lowered efficiencies. Another key result from the testing is that both the manufacturer curve and the experimental curve converge at 80% for high pressure ratios. The two

curves converge on the same value because the heat rejection rate is constant, so at high flows and pressures the heat losses become insignificant.

Another key result from the experimental study was the operating range of the turbine. Figure 5-3 shows the range of pressure ratios for a given reduced mass flow and a range for reduced mass flow at a given pressure ratio.

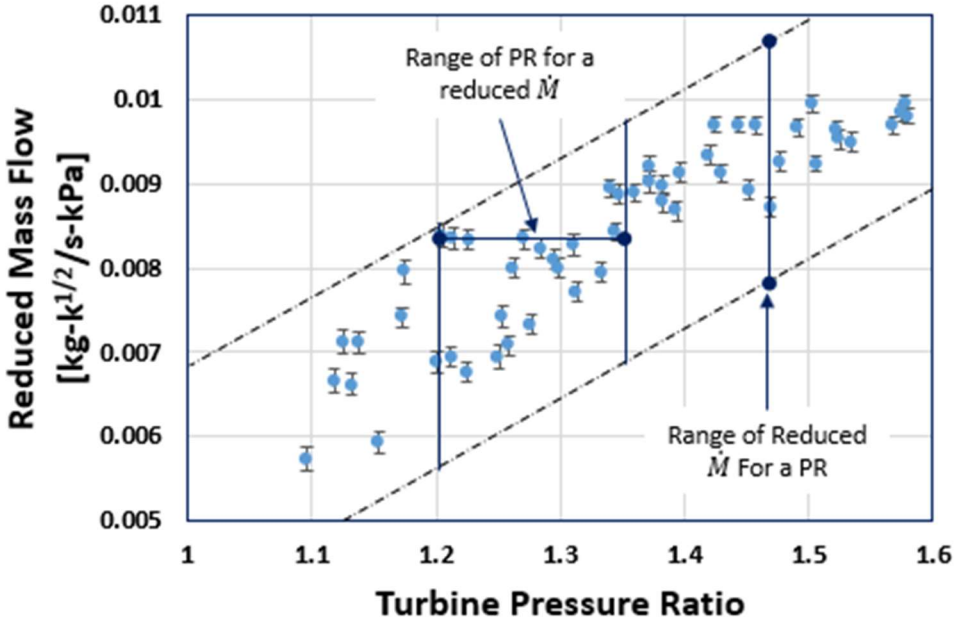

Figure 5-3: Turbine reduced mass flow curve

These ranges are used to determine performance of the turbine as shown in the modeling section. In addition, the experimental reduced mass flow rate was approximately 17% less than the manufacturer equivalent at a given pressure ratio. This decrease is primarily caused by the lower density of the exhaust air because the temperature was 115°C compared to the 70°C manufacturer tests.

5.2: Model Results

The results from the experimental data at increased temperatures were input into the model to determine performance across a range of operating conditions. The results of turbo-machine power consumption are shown in Figure 5-4.

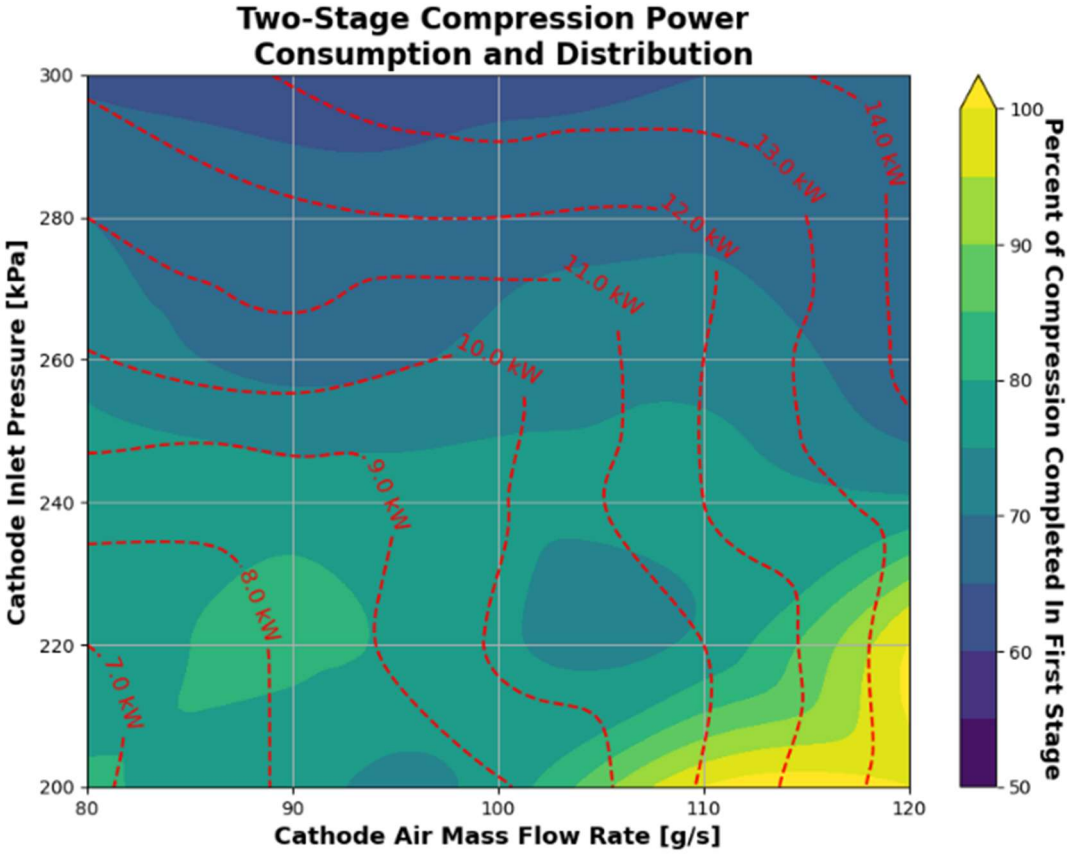

Figure 5-4: Compressor performance in test range

Although single stage compression was possible in many configurations, in every case where two-stage operation of the compressor-turbine system was possible it was more efficient. The only cases where single-stage operation was viable were cases of high flow and low pressure (bottom right of Figure 5-4) as a second stage is past the choke line of the map. In some cases where the first turbine's inlet pressure was low, but the flow was still high, the second stage was bypassed. This is because at the higher flow rates the first stage was choked unless it did all the expansion, resulting in the second turbine being bypassed.

The pressure losses through the system resulted in significant over pressuring at the outlet of the compressor. At lower target pressures, the compressor outlet could be as high as 60 kPa above the fuel cell inlet. The pressure losses in the piping are larger at low pressures because the decrease in density requires higher flow velocity and thus higher friction losses for the same mass flow. In addition, higher flow rates cause a similar effect, with the increase in flow causing an increase in velocity which increases pressure drop for the same inlet pressure. Figure 5-4 shows the power consumption of the compressors and turbines combined, which form a corner along the center of the map. This corner forms because the turbine operates at a limited flow rate at a specific pressure. Following the 9-kW line for example, the turbines compensate for the power consumption as flow increases but at 95 g/s the second stage turbine starts to be bypassed, resulting in a steep drop off. The bypassing of the turbines is so extensive due to the devices being meant for lower temperature PEM cells. If the turbine was larger to accommodate the decreased density at 115°C then the first stage turbine could operate at a smaller expansion ratio, enabling full utilization of the second stage.

Multiple phenomena are observed in Figure 5-5, which displays the system power and efficiency for the various flow conditions and currents.

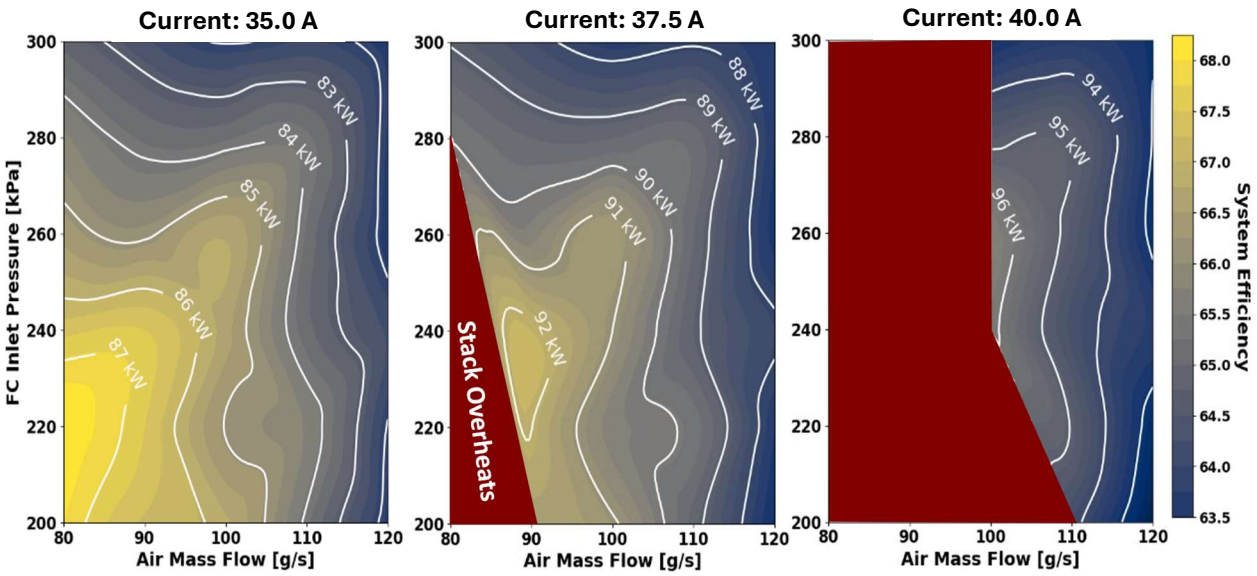

Figure 5-5: System power and efficiency contour

First, as the current was increased, many conditions began to fail due to heat transfer limitations within the cells. This is because of the increase in current results in more heat being produced. The modeling process assumes that the maximum allowable temperature gradient across the cells was 120°C, which limits air flow rate such that at high current draw and low air flow the operating temperatures of the cells are violated. This resulted in several model results being rejected particularly the low flow cases where insufficient heat rejection occurred. Lower pressure conditions also violated these limits because the cell efficiency dropped at lower pressures which generates more heat. Second, system efficiency of the full system appears to concentrate at the lowest flows and pressures. The peak efficiency of the system of 68.2% was observed to be 220 kPa and 80 g/s as shown in Figure 5-6.

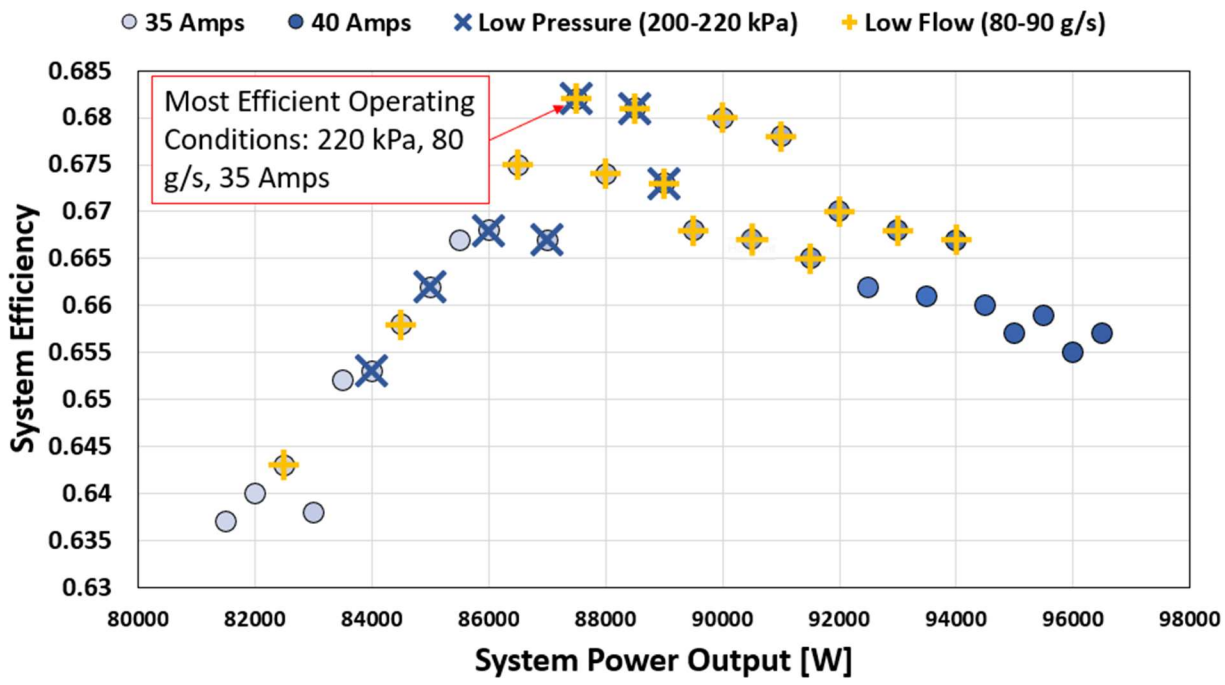

Figure 5-6: Best performance for every power output

This indicates that pressurization of the system is still necessary to increase performance, and an ideal condition can be found in the 200-240 kPa region. The diagonal trend across the Figure 5-5 is due to the results from Figure 5-4, in which a corner for each power consumption is formed. The peak efficiencies for a given pressure line up with the corners, in which the maximum flow rate is achievable before a steep increase in power consumption is required due to turbine choke. The parabolic trend in Figure 5-6 is explained by the two limbs of the arc separately. The left limb shows the trend towards higher efficiency as the amount of power consumed by the air BOP is reduced (lower flowrates and pressures). The right limb shows the results of increasing cell current, which results in a smaller but still significant decrease in efficiency due to ohmic losses.

5.3:Discussion

When analyzing the results, four key system variables affect the total system performance: turbocharger power consumption, engine power production, system parasitic load, and stack efficiency. The three non-fuel cell system variables are all effected by the three modeled variables (air flow, pressure, and stack current); however, each component has a primary correlation with a system variable (Table 6-1).

Table 5-1: System and model variable correlations

Fuel Cell Variable	Engine Power	Parasitic Load	Compressor Load
Stack Amperage	0.98	0.57	0.22
Inlet Pressure	-0.12	0.84	0.62
Air Flowrate	0.27	0.065	0.67

The engine power correlates closely with increased stack current, parasitic load with inlet pressure, and compressor load with air flow rate and pressure. The correlation of compressor load with air flow and pressure is self-evident. The effects of stack current on the parasitic load and engine power are a result of increased fuel flow. As stack current increases, the fuel flow rate must increase to maintain the fuel utilization which also results in an increased fuel flow to the engine that can produce higher power. The same is true for the parasitic load in which the fuel compressor power increases due to increased fuel flow and pressure. The higher correlation of pressure than fuel flow rate is because fuel flow rate variation is much smaller than the pressure variation.

The final system variable, the stack efficiency, is connected directly to each modeled variable. In Figure 5-5 the efficiency across each plot can be seen decreasing with the increase in

current. This is due to decreases in stack efficiency from increased Ohmic overpotentials at higher current density [18]. Another variable which affects cell performance is pressurization, which increases efficiency roughly 1.7% from 200 kPa to 300 kPa when all other conditions are maintained. The air flow rate increases efficiency marginally, around 0.3% over maintained conditions. The effect of these variables is visualized for the 40-Amp case in Figure 6-1 where the efficiency and power are represented by triangles and circles, respectively, and each set of air flow rates is color coded.

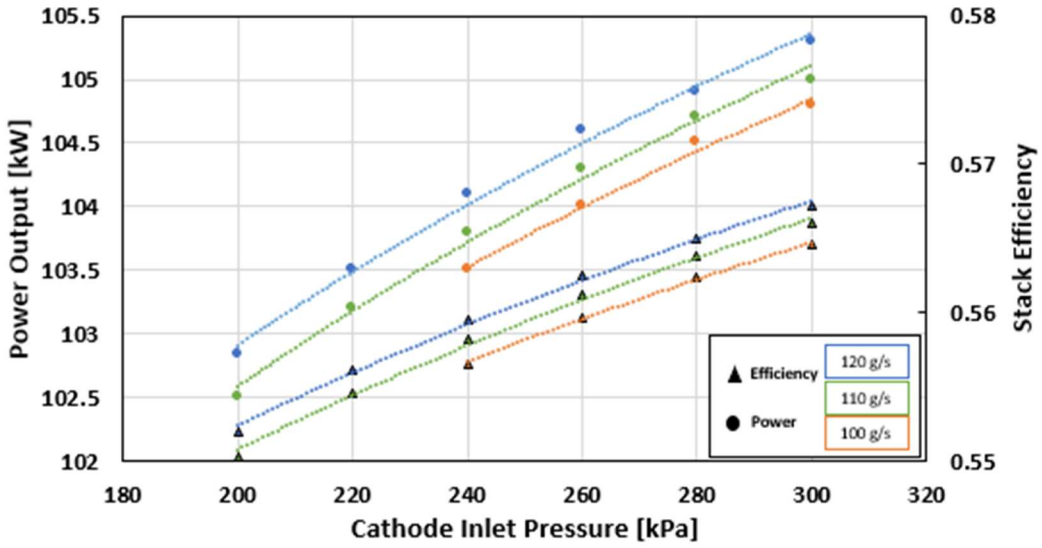

Figure 5-7: Efficiency impacts of model variables on stacks at 40 Amps

The x-axis is the inlet pressure of the cathode, while the y-axes are the power output or efficiency of the stacks. Across the three flowrates shown: 100, 110, and 120 g/s, there is a linear increase in efficiency of roughly 0.04%. When flow rate is held constant, pressure increases efficiency 0.02-0.04% per 20 kPa with higher pressures showing smaller increases. All these efficiency improvements result in a total efficiency increase of 1.7% which corresponds to a power increase of 2.75 kW.

Each system variable contributes either negatively or positively to system efficiency. The compressor and parasitic loads reduce efficiency while the engine and stacks increase it. To determine which variable has the higher impact, their range of contribution to system efficiency was determined individually with equations 5.26 and 5.27.

$$R_{variable} = Max(\eta_{\text{variable}}) - Min(\eta_{\text{variable}}) \quad (5.26)$$

$$\eta_{\text{variable}} = P_{\text{variable}}/(LHV_{\text{fuel}} \times \dot{m}_{\text{fuel}}) \quad (5.27)$$

Figure 5-2 does not show the total contribution to efficiency of a variable, but how much that variable's contribution to the system efficiency changes over the case range.

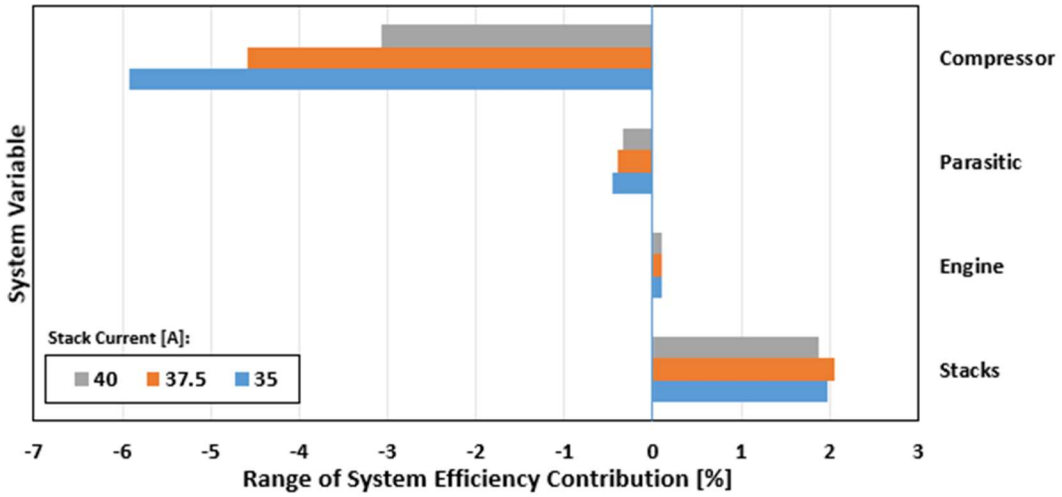

Figure 5-8: Range of system efficiency contribution of system variables

The range selected for Figure 6-2 matches those seen in Figure 5-5: 35, 37.5 and 40 Amps. The average change in efficiency was -4.5%, -0.59%, 0.10%, and 1.96%, for the compressor, parasitic, engine, and stack efficiency, respectively. The compressor has the highest efficiency change which indicates the compressor is the dominant factor in the system efficiency. However, as the current increases, the change in efficiency drops from -5.94% to –2.80% which indicates that the significance of the compressor's performance becomes less dominant at higher current levels. This matches the results seen in Figure 5-6, where for higher currents the compressors' effect on efficiency is reduced and the ohmic losses in the fuel cells begin to dominate.

CHAPTER 6:CONCLUSION

The present study aimed to find the optimal operating conditions for an 80-kW pressurized SOFC/ICE/Turbo hybrid system operating on natural gas fuel over a range of air flows, stack currents, and pressures. The results show that the pressurization of the cells does provide an increase in stack efficiency, however, there is a corresponding air BOP load which lowers system efficiency. Furthermore, the air BOP load has the largest effect on system performance over the range of conditions that was evaluated for this study. The peak efficiency of 68% for the presented SOFC/ICE/TURBO system with a two-stage Fischer motored turbocharger was reached at 220 kPa and 80 g/s with a current draw of 35 A. This result indicates that pressurization is still a necessary part of improving system performance because the optimal point was not at the lowest pressure and flow rate.

This is valuable insight for the continued development of pressurized SOFC-ICE hybrids, as it indicates that increased pressurization will only decrease the performance of these systems because of the logarithmic gains of pressurizing SOFCs in contrast to the relatively linear losses incurred by the compressor system. Designing these hybrid systems for lower pressures and flows enables designs to be more cost effective as the investment into the air BOP will be less significant, and the optimized efficiency of the system will result in higher return on investment and lowered emissions, making SOFC-ICE hybrids a more competitive alternative to traditional fossil fuel generation systems.

For future work, the Fischer device was only tested as a single stage to replicate some of the conditions the second stage will experience. However, for more accurate modeling, two-stage operation needs to be validated by operating the devices for the expected pressure ratios shown in

this study. Further analysis of the Fischer device's ability to handle the axial load expected on the second stage needs to be completed before any testing is to be completed. The device is not being used within its intended design range and therefore concerns of damage to the axial bearing need to be addressed. In addition, full system experiments should follow the compressor validation to confirm the modeling results presented in this study.

Exploring only the three independent variables discussed in this study would require a massive quantity of tests to capture the system dynamics. This is not ideal due to the expense and time required to test the full system. To reduce the testing time, I suggest factorial experimental design in which the three factors are tested each at 3 levels. This initial set of tests would result in "cubes" of experimental data which would indicate an ideal range to further narrow the testing scope. This would hopefully only require an initial 27 tests, followed by subsequent test batches of similar scale instead of sweeping the 300 cases explored in the model. This would provide significant advantage when attempting to narrow down the performance to single kPa or g/s conditions, as such testing would require tens of thousands of tests using traditional methods.

The best point of operation found in this study for the 80-kW system may not reflect the optimal running conditions for a much larger system. A similar study done on the 1 MW scale would be valuable for considering larger scale designs. As the air BOP power draw may be of much less significance at those scales, reducing the impact it has on the total system efficiency.

The limited availability of specialized motored turbochargers means that the Fischer device selected for this study was not specifically designed for SOFC applications. The temperature limits at the turbine inlet meant that much of the available enthalpy was lost to the precooler. The air preheater hot side has an outlet temperature that averages around 150°C, meaning for 100 g/s of airflow the system is losing around 3.5 kW to cooling the flow. The system efficiency could be

further increased by redesigning the turbomachinery. Particularly, the size of the turbine would need to be redesigned to match the lower densities. In addition, the seals and bearings would need to be made with different materials to handle the 150℃-200℃. Such redesigns may pose challenges, as the speed of the compressor may not match well with the turbine with these modifications.

WORKS CITED

[1] "Electricity Consumption by Country 2025." Accessed: Nov. 19, 2025. [Online]. Available: https://worldpopulationreview.com/country-rankings/electricity-consumption-by-country

[2] "U.S. Energy Information Administration - EIA - Independent Statistics and Analysis." Accessed: Nov. 19, 2025. [Online]. Available: https://www.eia.gov/environment/emissions/carbon/

[3] Y. a. Çengel, "Thermodynamics: An Engineering Approach," *McGraw-Hill*, 2004.

[4] R. M. Ormerod, "Solid oxide fuel cells," 2003. doi: 10.1039/b105764m.

[5] A. Farooq and Ö. N. Cora, "Current Status and Future Perspectives for Mobility Options Toward Sustainable Transportation With a Focus on Fuel Cells," *Wiley Interdiscip Rev Energy Environ*, vol. 13, no. 5, Sep. 2024, doi: 10.1002/wene.539.

[6] Office of Energy Efficiency and Renewable Energy, "Comparison of Fuel Cell Technologies | Department of Energy," Hydrogen and Fuel Cell Technologies Office. Accessed: Jan. 05, 2026. [Online]. Available: https://www.energy.gov/eere/fuelcells/comparison-fuel-cell-technologies

[7] DOE, "Fuel Cells | Department of Energy," Department of Energy. Accessed: Jan. 05, 2026. [Online]. Available: https://www.energy.gov/eere/fuelcells/fuel-cells

[8] A. Tarancón, "Strategies for lowering solid oxide fuel cells operating temperature," 2009. doi: 10.3390/en20401130.

[9] T. Araki, T. Ohba, S. Takezawa, K. Onda, and Y. Sakaki, "Cycle analysis of planar SOFC power generation with serial connection of low and high temperature SOFCs," *J Power Sources*, vol. 158, no. 1, 2006, doi: 10.1016/j.jpowsour.2005.09.003.

[10] A. V. Virkar, K. Z. Fung, and S. C. Singhal, "The Effect of Pressure on Solid Oxide Fuel Cell Performance," in *Region 3 Southeastcon*, Blacksburg: Utah University Department of Materials Science and Engineering, Apr. 1997.

[11] M. Henke *et al.*, "Effect of pressure variation on power density and efficiency of solid oxide fuel cells," *Electrochim Acta*, vol. 66, 2012, doi: 10.1016/j.electacta.2012.01.075.

[12] C. Cadigan *et al.*, "Performance characterization of metal-supported solid-oxide fuel cell stacks at elevated pressure," *J Power Sources*, vol. 573, 2023, doi: 10.1016/j.jpowsour.2023.233083.

[13] O. B. Rizvandi and H. L. Frandsen, “Modeling of single- and double-sided high-pressure operation of solid oxide electrolysis stacks,” *Int J Hydrogen Energy*, vol. 48, no. 77, 2023, doi: 10.1016/j.ijhydene.2023.04.169.

[14] Y. Wang, R. Zhan, Y. Qin, G. Zhang, Q. Du, and K. Jiao, “Three-dimensional modeling of pressure effect on operating characteristics and performance of solid oxide fuel cell,” *Int J Hydrogen Energy*, vol. 43, no. 43, 2018, doi: 10.1016/j.ijhydene.2018.09.025.

[15] G. J. Williams, Siddle A, and Pointon K, “Design Optimisation of a Hybrid Solid Oxide Fuel Cell and Gas Turbine Power Generation System,” Jul. 2001. [Online]. Available: https://www.osti.gov/etdeweb/biblio/20249899

[16] Y. Yi, A. D. Rao, J. Brouwer, and G. S. Samuelsen, “Analysis and optimization of a solid oxide fuel cell and intercooled gas turbine (SOFC–ICGT) hybrid cycle,” *J Power Sources*, vol. 132, no. 1–2, pp. 77–85, May 2004, doi: 10.1016/J.JPOWSOUR.2003.08.035.

[17] G. Floerchinger, O. B. Rizvandi, and R. J. Braun, “Considerations for the Design of Deployable SOC Systems with Multi-Stack Modules: Applying Experience from Kw-Scale Test Tystems,” in *SOFC-XIX*, Stockholm: The Electrochemical Society, Jul. 2025.

[18] G. Floerchinger, C. Cadigan, N. P. Sullivan, and R. J. Braun, “Characterizing the Performance of kW-Scale Multi-Stack Solid Oxide Fuel Cell Modules through Modeling,” *ECS Trans*, vol. 111, no. 6, 2023, doi: 10.1149/11106.0803ecst.

[19] V. A. Reyes-Flores *et al.*, “Operational Conditions for an Internal Combustion Engine in a SOFC-ICE Hybrid Power Generation System,” *Energies (Basel)*, vol. 18, no. 7, Apr. 2025, doi: 10.3390/en18071838.

[20] L. J.-B. Mitchel, “High efficiency air delivery system for solid oxide fuel cell power generation,” Colorado State University, 2024.

[21] J. C. Rodríguez, N. F. Harun, N. Zhou, E. Sabolsky, and D. Tucker, “System analysis of a 100kW internal combustion engine (ICE) solid oxide fuel cell (SOFC) hybrid configuration,” in *American Society of Mechanical Engineers, Power Division (Publication) POWER*, 2020. doi: 10.1115/POWER2020-16620.

[22] A. B. Stambouli and E. Traversa, “Solid oxide fuel cells (SOFCs): A review of an environmentally clean and efficient source of energy,” 2002. doi: 10.1016/S1364-0321(02)00014-X.

[23] B. Li, Z. Lyu, J. Zhu, M. Han, and Z. Sun, “Study on the operating parameters of the 10 kW SOFC-CHP system with syngas,” *Int J Coal Sci Technol*, vol. 8, no. 4, 2021, doi: 10.1007/s40789-021-00451-3.

[24] M. M. Whiston, I. M. L. Azevedo, S. Litster, C. Samaras, K. S. Whitefoot, and J. F. Whitacre, “Meeting U.S. Solid Oxide Fuel Cell Targets,” 2019. doi: 10.1016/j.joule.2019.07.018.

[25] M. J. Reddy, J. E. Svensson, and J. Froitzheim, “Evaluating candidate materials for balance of plant components in SOFC: Oxidation and Cr evaporation properties,” *Corros Sci*, vol. 190, 2021, doi: 10.1016/j.corsci.2021.109671.

[26] S. P. Jiang, “Issues on development of (La,Sr)MnO3 cathode for solid oxide fuel cells,” *J Power Sources*, vol. 124, no. 2, 2003, doi: 10.1016/S0378-7753(03)00814-0.

[27] The Engineering ToolBox, “Metals Strength vs. Temperature.” Accessed: Oct. 19, 2025. [Online]. Available: https://www.engineeringtoolbox.com/metal-temperature-strength-d_1353.html

[28] H. Djamel, A. Hafsia, Z. Bariza, B. M. Hocine, and O. Kafia, “Thermal field in SOFC fed by hydrogen: Inlet gases temperature effect,” *Int J Hydrogen Energy*, vol. 38, no. 20, pp. 8575–8583, Jul. 2013, doi: 10.1016/J.IJHYDENE.2013.01.004.

[29] C. Lin, F. Kerscher, and H. Spliethoff, “Thermal gradient management in solid oxide fuel cells: Mechanisms, strategies, and future directions,” *J Power Sources*, vol. 656, p. 238017, Nov. 2025, doi: 10.1016/J.JPOWSOUR.2025.238017.

[30] P. Costamagna, “The benefit of solid oxide fuel cells with integrated air pre-heater,” *J Power Sources*, vol. 69, no. 1–2, pp. 1–9, Nov. 1997, doi: 10.1016/S0378-7753(96)02386-5.

[31] K. P. Recknagle, E. M. Ryan, B. J. Koeppel, L. A. Mahoney, and M. A. Khaleel, “Modeling of electrochemistry and steam–methane reforming performance for simulating pressurized solid oxide fuel cell stacks,” *J Power Sources*, vol. 195, no. 19, pp. 6637–6644, Oct. 2010, doi: 10.1016/J.JPOWSOUR.2010.04.024.

[32] P. Costamagna, “The benefit of solid oxide fuel cells with integrated air pre-heater,” *J Power Sources*, vol. 69, no. 1–2, pp. 1–9, Nov. 1997, doi: 10.1016/S0378-7753(96)02386-5.

[33] “Kalina Cycle - an overview | ScienceDirect Topics.” Accessed: Oct. 22, 2025. [Online]. Available: https://www.sciencedirect.com/topics/engineering/kalina-cycle

[34] M. Song, Y. Zhuang, L. Zhang, W. Li, J. Du, and S. Shen, “Thermodynamic performance assessment of SOFC-RC-KC system for multiple waste heat recovery,” *Energy Convers Manag*, vol. 245, p. 114579, Oct. 2021, doi: 10.1016/J.ENCONMAN.2021.114579.

[35] M. A. Emadi, N. Chitgar, O. A. Oyewunmi, and C. N. Markides, “Working-fluid selection and thermoeconomic optimisation of a combined cycle cogeneration dual-loop organic

Rankine cycle (ORC) system for solid oxide fuel cell (SOFC) waste-heat recovery," *Appl Energy*, vol. 261, p. 114384, Mar. 2020, doi: 10.1016/J.APENERGY.2019.114384.

[36] A. Javed, H. A. Khalid, S. U. bin Arif, M. Imran, A. Rezk, and Z. A. Khan, "Micro gas turbine small-scale effects in range extended electric vehicles," *Journal of Energy Resources Technology, Transactions of the ASME*, vol. 143, no. 12, 2021, doi: 10.1115/1.4051384.

[37] X. Zhang, S. H. Chan, G. Li, H. K. Ho, J. Li, and Z. Feng, "A review of integration strategies for solid oxide fuel cells," 2010. doi: 10.1016/j.jpowsour.2009.07.045.

[38] M. Gandiglio, A. Lanzini, P. Leone, M. Santarelli, and R. Borchiellini, "Thermoeconomic analysis of large solid oxide fuel cell plants: Atmospheric vs. pressurized performance," 2013. doi: 10.1016/j.energy.2013.03.059.

[39] P. Kuchonthara, S. Bhattacharya, and A. Tsutsumi, "Energy recuperation in solid oxide fuel cell (SOFC) and gas turbine (GT) combined system," *J Power Sources*, vol. 117, no. 1–2, pp. 7–13, May 2003, doi: 10.1016/S0378-7753(03)00009-0.

[40] D. P. Bakalis and A. G. Stamatis, "Optimization methodology of turbomachines for hybrid SOFC–GT applications," *Energy*, vol. 70, pp. 86–94, Jun. 2014, doi: 10.1016/J.ENERGY.2014.03.093.

[41] W. Burbank, D. D. Witmer, and F. Holcomb, "Model of a novel pressurized solid oxide fuel cell gas turbine hybrid engine," *J Power Sources*, vol. 193, no. 2, 2009, doi: 10.1016/j.jpowsour.2009.04.004.

[42] S. R. Oh, J. Sun, H. Dobbs, and J. King, "Performance evaluation of solid oxide fuel cell engines integrated with single/dual-spool turbochargers," *J Fuel Cell Sci Technol*, vol. 8, no. 6, 2011, doi: 10.1115/1.4004471.

[43] L. Mantelli, M. L. Ferrari, and A. Traverso, "Dynamics and control of a turbocharged solid oxide fuel cell system," *Appl Therm Eng*, vol. 191, 2021, doi: 10.1016/j.applthermaleng.2021.116862.

[44] M. L. Ferrari, M. De Campo, and L. Magistri, "Design and emulation of a turbocharged bio-fuelled sofc plant," in *Proceedings of the ASME Turbo Expo*, 2018. doi: 10.1115/GT201875026.

[45] F. D.F. Chuahy and S. L. Kokjohn, "Solid oxide fuel cell and advanced combustion engine combined cycle: A pathway to 70% electrical efficiency," *Appl Energy*, vol. 235, 2019, doi: 10.1016/j.apenergy.2018.10.132.

[46] M. Anderson, "Turbines vs. Reciprocating Engine Generators," Bridgestone Associates Limited. Accessed: Oct. 27, 2025. [Online]. Available: https://brdgstn.com/turbines-vs-reciprocating-engine-generators/

[47] W. Choi, J. Kim, Y. Kim, S. Kim, S. Oh, and H. H. Song, “Experimental study of homogeneous charge compression ignition engine operation fuelled by emulated solid oxide fuel cell anode off-gas,” *Appl Energy*, vol. 229, 2018, doi: 10.1016/j.apenergy.2018.07.086.

[48] W. Choi, J. Kim, Y. Kim, and H. H. Song, “Solid oxide fuel cell operation in a solid oxide fuel cell–internal combustion engine hybrid system and the design point performance of the hybrid system,” *Appl Energy*, vol. 254, 2019, doi: 10.1016/j.apenergy.2019.113681.

[49] W. Choi, J. Kim, Y. Kim, and H. H. Song, “Solid oxide fuel cell operation in a solid oxide fuel cell–internal combustion engine hybrid system and the design point performance of the hybrid system,” *Appl Energy*, vol. 254, p. 113681, Nov. 2019, doi: 10.1016/J.APENERGY.2019.113681.

[50] J. Kim, Y. Kim, W. Choi, K. Y. Ahn, and H. H. Song, “Analysis on the operating performance of 5-kW class solid oxide fuel cell-internal combustion engine hybrid system using spark-assisted ignition,” *Appl Energy*, vol. 260, 2020, doi: 10.1016/j.apenergy.2019.114231.

[51] R. Braun *et al.*, “Development of a High-Efficiency, Low-Cost Hybrid SOFC/Internal Combustion Engine Power Generator,” *ECS Trans*, vol. 103, no. 1, 2021, doi: 10.1149/10301.0221ecst.

[52] R. J. Braun *et al.*, “Development of a Novel High Efficiency, Low Cost Hybrid SOFC/Internal Combustion Engine Power Generator,” *ECS Trans*, vol. 91, no. 1, 2019, doi: 10.1149/09101.0355ecst.

[53] “Scroll Compressors - an overview | ScienceDirect Topics.” Accessed: Oct. 28, 2025. [Online]. Available: https://www.sciencedirect.com/topics/engineering/scroll-compressors

[54] S. L. Dixon and C. A. Hall, *Fluid Mechanics and Thermodynamics of Turbomachinery*. 2010. doi: 10.1016/C2009-0-20205-4.

[55] “What is an electric turbocharger? | Mitsubishi Turbocharger.” Accessed: Oct. 28, 2025. [Online]. Available: https://www.turbocharger.mtee.eu/what-is-an-electric-turbocharger/

[56] “FISCHER HIGH-SPEED TURBO COMPRESSORS.” Accessed: Oct. 28, 2025. [Online]. Available: https://www.fischerspindle.com/en/products/high-speed-turbo-compressors

[57] K. Toyama, P. W. Runstadler, and R. C. Dean, “An experimental study of surge in centrifugal compressors,” *Journal of Fluids Engineering, Transactions of the ASME*, vol. 99, no. 1, 1977, doi: 10.1115/1.3448506.

[58] R. Stasyshan, “How inlet conditions impact centrifugal air compressors,” *Renewable and Sustainable Energy Reviews*, vol. 80, pp. 1–6, 2015.

[59] T. Dugan, “Inlet Air Temperature Impacts on Air Compressor Performance,” Compressed Air Best Practices. Accessed: Sep. 17, 2025. [Online]. Available: https://www.airbestpractices.com/system-assessments/compressor-controls/inlet-air-temperature-impacts-air-compressor-performance

[60] R. Stasyshan, “How inlet conditions impact centrifugal air compressors,” *Renewable and Sustainable Energy Reviews*, vol. 80, pp. 1–6, 2015.

[61] Office of Energy Efficiency and Renewable Energy, “Improving Compressed Air System Performance,” 2003. Accessed: Aug. 24, 2025. [Online]. Available: chrome-extension://efaidnbmnnnibpcajpcglclefindmkaj/https://www1.eere.energy.gov/manufacturing/tech_assistance/pdfs/compressed_air_sourcebook.pdf

[62] R. Persky and E. Sauret, “Loss models for on and off-design performance of radial inflow turbomachinery,” *Appl Therm Eng*, vol. 150, 2019, doi: 10.1016/j.applthermaleng.2019.01.042.

[63] N. D. Whitehouse, A. Stotter, and M. S. Janota, “Estimating the effects of altitude, ambient temperature and turbocharger match on engine performance,” *ARCHIVE: Proceedings of the Institution of Mechanical Engineers 1847-1982 (vols 1-196)*, vol. 178, no. 1963, 1963, doi: 10.1243/pime_proc_1963_178_036_02.

[64] Office of Energy Efficiency and Renewable Energy, “Comparison of Fuel Cell Technologies | Department of Energy,” 2021.

[65] O. Corigliano, L. Pagnotta, and P. Fragiacomo, “On the Technology of Solid Oxide Fuel Cell (SOFC) Energy Systems for Stationary Power Generation: A Review,” 2022. doi: 10.3390/su142215276.

[66] R. Jones-Albertus, “Confronting the Duck Curve: How to Address Over-Generation of Solar Energy | Department of Energy,” *Office of Energy Efficiency & Renewable Energy*, 2017.

[67] D. Oryshchyn, N. F. Harun, D. Tucker, K. M. Bryden, and L. Shadle, “Fuel utilization effects on system efficiency in solid oxide fuel cell gas turbine hybrid systems,” *Appl Energy*, vol. 228, 2018, doi: 10.1016/j.apenergy.2018.07.004.

[68] M. Song, Y. Zhuang, L. Zhang, W. Li, J. Du, and S. Shen, “Thermodynamic performance assessment of SOFC-RC-KC system for multiple waste heat recovery,” *Energy Convers Manag*, vol. 245, p. 114579, Oct. 2021, doi: 10.1016/J.ENCONMAN.2021.114579.

[69] American Gas Association, American Petroleum Institute, and Gas Processors Association, “AGA 3.1: Orifice Metering of Natural Gas and Other Related Hydrocarbon Fluids: Part 1,” Oct. 1990. Accessed: Nov. 20, 2025. [Online]. Available: chrome-

extension://efaidnbmnnnibpcajpcglclefindmkaj/https://law.resource.org/pub/us/cfr/ibr/001/aga.3.1.1990.pdf

[70] Joint Committee For Guides In, “Evaluation of measurement data — Guide to the expression of uncertainty in measurement,” *International Organization for Standardization Geneva ISBN*, vol. 50, no. September, 2008.

[71] T. L. Bergman, A. S. Lavine, F. P. Incropera, and D. P. Dewitt, *Fundamentals of Heat and Mass Transfer, 2011. Fundamentals of Heat and Mass Transfer. 7th Edition.* 2011.

[72] W. Li and P. Hrnjak, “Compensating for the end-plate effect on heat transfer in brazed plate heat exchangers,” *International Journal of Refrigeration*, vol. 126, 2021, doi: 10.1016/j.ijrefrig.2021.01.019.

[73] W. Li and P. Hrnjak, “Single-phase flow distribution in plate heat exchangers: Experiments and models,” *International Journal of Refrigeration*, vol. 126, 2021, doi: 10.1016/j.ijrefrig.2021.01.026.

[74] N. R. Smith, R. A. Berdanier, J. C. Fabian, and N. L. Key, “Reconciling compressor performance differences for varying ambient inlet conditions,” *J Eng Gas Turbine Power*, vol. 137, no. 12, 2015, doi: 10.1115/1.4030518.

[75] B. Sirakov and M. Casey, “Evaluation of Heat Transfer Effects on Turbocharger Performance,” *J Turbomach*, vol. 135, no. 2, 2012, doi: 10.1115/1.4006608.

APPENDIX A. SYSTEM DATA

80 g/s Airflow

Net Power (kW)

	200	220	240	260	280	300
35	87.3	87.6	86.5	85.3	84.4	83.4
35.5	88.4	88.7	87.6	86.4	85.6	84.5
36		89.8	88.7	87.5	86.7	85.6
36.5		90.8	89.8	88.6	87.8	86.7
37				89.7	88.9	87.9
37.5					90.0	89.0

Stack Power (kW)

	200	220	240	260	280	300
35	91.8	92.4	92.8	93.2	93.5	93.8
35.5	92.9	93.4	93.9	94.3	94.6	94.9
36		94.5	94.9	95.3	95.7	95.9
36.5		95.5	96.0	96.4	96.7	97.0
37				97.4	97.8	98.1
37.5					98.8	99.1

System Efficiency (%)

	200	220	240	260	280	300
35	68.0	68.2	67.4	66.4	65.8	64.9
35.5	67.9	68.1	67.3	66.3	65.7	64.9
36		68.0	67.2	66.3	65.6	64.8
36.5		67.8	67.0	66.2	65.6	64.8
37				66.1	65.5	64.7
37.5					65.4	64.7

Engine Power (kW)

	200	220	240	260	280	300
35	5.65	5.63	5.61	5.58	5.55	5.53
35.5	5.74	5.71	5.69	5.66	5.63	5.60
36		5.79	5.77	5.74	5.71	5.68
36.5		5.87	5.85	5.82	5.79	5.76
37				5.90	5.87	5.84
37.5					5.95	5.92

Stack Efficiency (%)

	200	220	240	260	280	300
35	56.4	56.7	57.1	57.3	57.6	57.7
35.5	56.2	56.6	56.9	57.2	57.4	57.6
36		56.4	56.7	57.0	57.2	57.4
36.5		56.2	56.6	56.8	57.1	57.3
37				56.7	56.9	57.1
37.5					56.8	57.0

Parasitic Load (kW)

	200	220	240	260	280	300
35	3.4	3.4	3.5	3.6	3.7	3.8
35.5	3.4	3.5	3.5	3.6	3.7	3.8
36		3.5	3.6	3.6	3.7	3.8
36.5		3.5	3.6	3.7	3.8	3.9
37				3.7	3.8	3.9
37.5					3.8	3.9

90 g/s Airflow

Net Power (kW)

	200	220	240	260	280	300
35	86.3	86.6	86.7	84.9	83.8	82.6
35.5	87.4	87.7	87.8	86.0	84.9	83.8
36	88.5	88.8	88.9	87.2	86.1	84.9
36.5	89.5	89.9	90.0	88.3	87.2	86.0
37	90.5	91.0	91.1	89.4	88.3	87.1
37.5	91.6	92.0	92.1	90.5	89.4	88.3
38		93.0	93.2	91.5	90.5	89.4
38.5			94.2	92.6	91.5	90.4
39				93.6	92.6	91.5
39.5						92.6

Stack Power (kW)

	200	220	240	260	280	300
35	92.1	92.6	93.1	93.4	93.7	94.0
35.5	93.1	93.7	94.1	94.5	94.8	95.1
36	94.2	94.7	95.2	95.6	95.9	96.2
36.5	95.2	95.8	96.2	96.6	97.0	97.2
37	96.2	96.8	97.3	97.7	98.0	98.3
37.5	97.1	97.8	98.3	98.7	99.1	99.4
38		98.8	99.3	99.8	100.1	100.4
38.5			100.3	100.8	101.2	101.5
39				101.8	102.2	102.5
39.5						103.5

System Efficiency (%)

	200	220	240	260	280	300
35	67.2	67.5	67.5	66.1	65.2	64.3
35.5	67.1	67.4	67.4	66.1	65.2	64.3
36	67.0	67.3	67.3	66.0	65.2	64.3
36.5	66.8	67.1	67.2	65.9	65.1	64.2
37	66.7	67.0	67.1	65.8	65.0	64.2
37.5	66.5	66.9	67.0	65.7	65.0	64.2
38		66.7	66.8	65.7	64.9	64.1
38.5			66.7	65.5	64.8	64.0
39				65.4	64.7	64.0
39.5						63.9

Engine Power (kW)

	200	220	240	260	280	300
35	5.7	5.6	5.6	5.6	5.6	5.5
35.5	5.7	5.7	5.7	5.7	5.6	5.6
36	5.8	5.8	5.8	5.7	5.7	5.7
36.5	5.9	5.9	5.8	5.8	5.8	5.8
37	6.0	6.0	5.9	5.9	5.9	5.8
37.5	6.1	6.0	6.0	6.0	5.9	5.9
38		6.1	6.1	6.1	6.0	6.0
38.5			6.2	6.1	6.1	6.1
39				6.2	6.2	6.2
39.5						6.2

Stack Efficiency (%)

	200	220	240	260	280	300
35	56.5	56.9	57.2	57.5	57.7	57.9
35.5	56.4	56.7	57.0	57.3	57.5	57.7
36	56.2	56.6	56.9	57.1	57.4	57.6
36.5	56.0	56.4	56.7	57.0	57.2	57.4
37	55.8	56.2	56.5	56.8	57.1	57.3
37.5	55.6	56.0	56.4	56.7	56.9	57.1
38		55.9	56.2	56.5	56.7	57.0
38.5			56.0	56.3	56.6	56.8
39				56.2	56.4	56.6
39.5						56.5

Parasitic Load (kW)

	200	220	240	260	280	300
35	3.4	3.4	3.5	3.6	3.7	3.8
35.5	3.4	3.5	3.5	3.6	3.7	3.8
36	3.4	3.5	3.6	3.7	3.7	3.8
36.5	3.5	3.5	3.6	3.7	3.8	3.9
37	3.5	3.6	3.6	3.7	3.8	3.9
37.5	3.5	3.6	3.7	3.8	3.8	3.9
38		3.6	3.7	3.8	3.9	4.0
38.5			3.7	3.8	3.9	4.0
39				3.9	3.9	4.0
39.5						4.1

100 g/s Airflow

Net Power (kW)

	200	220	240	260	280	300
35	85.8	85.0	85.5	85.6	83.7	81.9
35.5	86.9	86.1	86.6	86.7	84.9	83.1
36	88.0	87.2	87.7	87.9	86.0	84.3
36.5	89.0	88.3	88.8	89.0	87.2	85.4
37	90.1	89.3	89.9	90.1	88.3	86.5
37.5	91.1	90.4	91.0	91.2	89.4	87.7
38	92.1	91.5	92.1	92.3	90.5	88.8
38.5	93.1	92.5	93.1	93.3	91.6	89.9
39	94.1	93.5	94.2	94.4	92.7	90.9
39.5		94.5	95.2	95.4	93.7	92.0
40			96.2	96.5	94.8	93.1

Stack Power (kW)

	200	220	240	260	280	300
35	92.3	92.8	93.3	93.6	93.9	94.1
35.5	93.4	93.9	94.3	94.7	95.0	95.2
36	94.4	95.0	95.4	95.8	96.1	96.3
36.5	95.4	96.0	96.5	96.9	97.2	97.4
37	96.4	97.0	97.5	97.9	98.2	98.5
37.5	97.4	98.1	98.6	99.0	99.3	99.6
38	98.4	99.1	99.6	100.0	100.4	100.7
38.5	99.4	100.1	100.6	101.0	101.4	101.7
39	100.3	101.0	101.6	102.1	102.4	102.8
39.5		102.0	102.6	103.1	103.4	103.8
40			103.5	104.0	104.5	104.8

System Efficiency (%)

	200	220	240	260	280	300
35	66.8	66.2	66.6	66.7	65.2	63.8
35.5	66.7	66.1	66.5	66.6	65.2	63.8
36	66.6	66.0	66.4	66.5	65.1	63.8
36.5	66.5	65.9	66.3	66.5	65.1	63.8
37	66.4	65.8	66.2	66.4	65.0	63.8
37.5	66.2	65.7	66.1	66.3	65.0	63.7
38	66.1	65.6	66.0	66.2	64.9	63.7
38.5	65.9	65.5	65.9	66.1	64.8	63.6
39	65.8	65.3	65.8	66.0	64.8	63.6
39.5		65.2	65.7	65.9	64.7	63.5
40			65.5	65.7	64.6	63.4

Engine Power (kW)

	200	220	240	260	280	300
35	5.7	5.6	5.6	5.6	5.6	5.5
35.5	5.7	5.7	5.7	5.7	5.6	5.6
36	5.8	5.8	5.8	5.7	5.7	5.7
36.5	5.9	5.9	5.8	5.8	5.8	5.8
37	6.0	6.0	5.9	5.9	5.9	5.8
37.5	6.1	6.0	6.0	6.0	5.9	5.9
38	6.1	6.1	6.1	6.1	6.0	6.0
38.5	6.2	6.2	6.2	6.1	6.1	6.1
39	6.3	6.3	6.2	6.2	6.2	6.2
39.5		6.4	6.3	6.3	6.3	6.2
40			6.4	6.4	6.3	6.3

Stack Efficiency (%)

	200	220	240	260	280	300
35	56.7	57.0	57.3	57.6	57.8	58.0
35.5	56.5	56.9	57.2	57.4	57.6	57.8
36	56.3	56.7	57.0	57.3	57.5	57.7
36.5	56.2	56.5	56.8	57.1	57.3	57.5
37	56.0	56.4	56.7	57.0	57.2	57.4
37.5	55.8	56.2	56.5	56.8	57.0	57.2
38	55.6	56.0	56.4	56.6	56.9	57.1
38.5	55.4	55.8	56.2	56.5	56.7	56.9
39	55.2	55.7	56.0	56.3	56.6	56.8
39.5		55.5	55.8	56.1	56.4	56.6
40			55.7	56.0	56.2	56.5

Parasitic Load (kW)

	200	220	240	260	280	300
35	3.3	3.4	3.5	3.6	3.7	3.8
35.5	3.3	3.4	3.5	3.6	3.7	3.8
36	3.4	3.5	3.6	3.7	3.8	3.9
36.5	3.4	3.5	3.6	3.7	3.8	3.9
37	3.5	3.5	3.6	3.7	3.8	3.9
37.5	3.5	3.6	3.7	3.8	3.9	4.0
38	3.5	3.6	3.7	3.8	3.9	4.0
38.5	3.6	3.7	3.7	3.8	3.9	4.0
39	3.6	3.7	3.8	3.9	4.0	4.1
39.5		3.7	3.8	3.9	4.0	4.1
40			3.9	3.9	4.0	4.1

110 g/s Airflow

Net Power (kW)

	200	220	240	260	280	300
35	83.9	84.3	83.6	83.8	83.8	82.2
35.5	85.0	85.4	84.7	84.9	85.0	83.4
36	86.1	86.5	85.8	86.0	86.1	84.5
36.5	87.1	87.6	86.9	87.2	87.2	85.7
37	88.2	88.7	88.0	88.3	88.4	86.8
37.5	89.2	89.8	89.1	89.4	89.5	87.9
38	90.3	90.9	90.2	90.5	90.6	89.1
38.5	91.3	91.9	91.3	91.6	91.7	90.2
39	92.3	92.9	92.3	92.7	92.8	91.3
39.5	93.3	93.9	93.4	93.7	93.9	92.3
40	94.2	94.9	94.4	94.8	94.9	93.4

Stack Power (kW)

	200	220	240	260	280	300
35	92.5	93.0	93.4	93.8	94.0	94.3
35.5	93.6	94.1	94.5	94.9	95.1	95.4
36	94.6	95.2	95.6	96.0	96.3	96.5
36.5	95.7	96.2	96.7	97.0	97.3	97.6
37	96.7	97.3	97.7	98.1	98.4	98.7
37.5	97.7	98.3	98.8	99.2	99.5	99.8
38	98.7	99.3	99.8	100.2	100.6	100.9
38.5	99.7	100.3	100.8	101.3	101.6	101.9
39	100.6	101.3	101.9	102.3	102.7	103.0
39.5	101.6	102.3	102.9	103.3	103.7	104.0
40	102.5	103.2	103.8	104.3	104.7	105.0

System Efficiency (%)

	200	220	240	260	280	300
35	65.0	65.7	65.1	65.2	65.3	64.0
35.5	65.2	65.6	65.0	65.2	65.2	64.0
36	65.2	65.5	65.0	65.1	65.2	64.0
36.5	65.1	65.4	64.9	65.1	65.2	64.0
37	65.0	65.4	64.9	65.0	65.1	64.0
37.5	64.9	65.3	64.8	65.0	65.1	63.9
38	64.8	65.2	64.7	64.9	65.0	63.9
38.5	64.6	65.1	64.6	64.8	64.9	63.8
39	64.5	64.9	64.5	64.8	64.9	63.8
39.5	64.4	64.8	64.4	64.7	64.8	63.7
40	64.2	64.7	64.3	64.6	64.7	63.7

Engine Power (kW)

	200	220	240	260	280	300
35	5.7	5.6	5.6	5.6	5.6	5.5
35.5	5.7	5.7	5.7	5.7	5.6	5.6
36	5.8	5.8	5.8	5.7	5.7	5.7
36.5	5.9	5.9	5.8	5.8	5.8	5.8
37	6.0	6.0	5.9	5.9	5.9	5.8
37.5	6.1	6.0	6.0	6.0	5.9	5.9
38	6.1	6.1	6.1	6.1	6.0	6.0
38.5	6.2	6.2	6.2	6.1	6.1	6.1
39	6.3	6.3	6.2	6.2	6.2	6.2
39.5	6.4	6.4	6.3	6.3	6.3	6.2
40	6.5	6.4	6.4	6.4	6.3	6.3

Stack Efficiency (%)

	200	220	240	260	280	300
35	56.8	57.1	57.4	57.7	57.9	58.1
35.5	56.6	57.0	57.3	57.5	57.7	57.9
36	56.5	56.8	57.1	57.4	57.6	57.8
36.5	56.3	56.7	57.0	57.2	57.4	57.6
37	56.1	56.5	56.8	57.1	57.3	57.5
37.5	56.0	56.3	56.7	56.9	57.2	57.4
38	55.8	56.2	56.5	56.8	57.0	57.2
38.5	55.6	56.0	56.3	56.6	56.9	57.1
39	55.4	55.8	56.2	56.4	56.7	56.9
39.5	55.2	55.6	56.0	56.3	56.5	56.8
40	55.0	55.5	55.8	56.1	56.4	56.6

Parasitic Load (kW)

	200	220	240	260	280	300
35	3.2	3.4	3.5	3.6	3.7	3.8
35.5	3.3	3.4	3.5	3.6	3.7	3.8
36	3.3	3.4	3.5	3.7	3.8	3.9
36.5	3.3	3.5	3.6	3.7	3.8	3.9
37	3.4	3.5	3.6	3.7	3.8	3.9
37.5	3.4	3.5	3.6	3.8	3.9	4.0
38	3.5	3.6	3.7	3.8	3.9	4.0
38.5	3.5	3.6	3.7	3.8	3.9	4.0
39	3.5	3.7	3.8	3.9	4.0	4.1
39.5	3.6	3.7	3.8	3.9	4.0	4.1
40	3.6	3.7	3.8	3.9	4.0	4.1

120 g/s Airflow

Net Power (kW)

	200	220	240	260	280	300
35	80.8	82.0	82.5	81.7	81.7	81.7
35.5	82.0	83.1	83.6	82.9	82.9	82.9
36	83.1	84.2	84.7	84.0	84.1	84.1
36.5	84.1	85.3	85.9	85.2	85.2	85.2
37	85.2	86.4	87.0	86.3	86.4	86.4
37.5	86.3	87.5	88.1	87.4	87.5	87.5
38	87.3	88.6	89.2	88.5	88.6	88.6
38.5	88.3	89.6	90.3	89.6	89.7	89.8
39	89.3	90.7	91.3	90.7	90.8	90.9
39.5	90.3	91.7	92.4	91.8	91.9	92.0
40	91.3	92.7	93.4	92.8	93.0	93.0

Stack Power (kW)

	200	220	240	260	280	300
35	92.7	93.2	93.6	93.9	94.2	94.4
35.5	93.8	94.3	94.7	95.0	95.3	95.5
36	94.8	95.3	95.8	96.1	96.4	96.6
36.5	95.9	96.4	96.8	97.2	97.5	97.8
37	96.9	97.5	97.9	98.3	98.6	98.9
37.5	97.9	98.5	99.0	99.4	99.7	99.9
38	98.9	99.5	100.0	100.4	100.8	101.0
38.5	99.9	100.6	101.1	101.5	101.8	102.1
39	100.9	101.6	102.1	102.5	102.9	103.2
39.5	101.9	102.6	103.1	103.5	103.9	104.2
40	102.8	103.5	104.1	104.6	104.9	105.3

System Efficiency (%)

	200	220	240	260	280	300
35	62.9	63.8	64.2	63.6	63.7	63.6
35.5	62.9	63.8	64.2	63.6	63.7	63.6
36	62.8	63.8	64.2	63.6	63.7	63.6
36.5	62.8	63.7	64.1	63.6	63.6	63.6
37	62.7	63.7	64.1	63.6	63.6	63.6
37.5	62.6	63.6	64.0	63.5	63.6	63.6
38	62.6	63.5	64.0	63.5	63.6	63.6
38.5	62.5	63.4	63.9	63.5	63.5	63.5
39	62.4	63.4	63.8	63.4	63.5	63.5
39.5	62.3	63.3	63.7	63.3	63.4	63.5
40	62.2	63.2	63.7	63.3	63.4	63.4

Engine Power (kW)

	200	220	240	260	280	300
35	5.7	5.6	5.6	5.6	5.6	5.5
35.5	5.7	5.7	5.7	5.7	5.6	5.6
36	5.8	5.8	5.8	5.7	5.7	5.7
36.5	5.9	5.9	5.8	5.8	5.8	5.8
37	6.0	6.0	5.9	5.9	5.9	5.8
37.5	6.1	6.0	6.0	6.0	5.9	5.9
38	6.1	6.1	6.1	6.1	6.0	6.0
38.5	6.2	6.2	6.2	6.1	6.1	6.1
39	6.3	6.3	6.2	6.2	6.2	6.2
39.5	6.4	6.4	6.3	6.3	6.3	6.2
40	6.5	6.4	6.4	6.4	6.3	6.3

Stack Efficiency (%)

	200	220	240	260	280	300
35	56.9	57.2	57.5	57.7	58.0	58.1
35.5	56.7	57.1	57.4	57.6	57.8	58.0
36	56.6	56.9	57.2	57.5	57.7	57.9
36.5	56.4	56.8	57.1	57.3	57.5	57.7
37	56.3	56.6	56.9	57.2	57.4	57.6
37.5	56.1	56.5	56.8	57.0	57.3	57.5
38	55.9	56.3	56.6	56.9	57.1	57.3
38.5	55.7	56.1	56.4	56.7	57.0	57.2
39	55.6	56.0	56.3	56.6	56.8	57.0
39.5	55.4	55.8	56.1	56.4	56.7	56.9
40	55.2	55.6	56.0	56.2	56.5	56.7

Parasitic Load (kW)

	200	220	240	260	280	300
35	3.1	3.3	3.4	3.6	3.7	3.8
35.5	3.2	3.3	3.5	3.6	3.7	3.8
36	3.2	3.3	3.5	3.6	3.7	3.9
36.5	3.2	3.4	3.5	3.7	3.8	3.9
37	3.3	3.4	3.6	3.7	3.8	3.9
37.5	3.3	3.5	3.6	3.7	3.8	4.0
38	3.4	3.5	3.6	3.8	3.9	4.0
38.5	3.4	3.5	3.7	3.8	3.9	4.0
39	3.5	3.6	3.7	3.8	3.9	4.1
39.5	3.5	3.6	3.7	3.9	4.0	4.1
40	3.6	3.7	3.8	3.9	4.0	4.1

APPENDIX B. EES CODE

```
FUNCTION q_act_ATGC (T_in_air, T_in_tg, P_in_air, i,m_dot_c, Cp_ATGC, T_tg)
$ARRAYS ON
"ATGC Inlet"
   "ATGC Properties----------------------------------------------------------"
   N_Ch_ATGC = 24
   w_atgc = 0.186 [m]

   ATGC_T = 0.002 [m]
   ATGC_L = 0.613 [m]
   Pressing_Depth = 0.002[m]
   D_e = 2 * Pressing_depth

   ATG_Area = 5.292 [m^2]
   f = 2.1865 "Correction Factor"
   k_plate = 21.5 [W/m-k]
   M_dot_tg = 0.036 [kg/s]

   "TG Properties"
   Cp_tg = 1.701 [kj/kg-k]
   mu_w = 0.027 [pa-s]
   mu_tg = 0.00002673 [Pa-s]
   k_tg = 0.03949 [w/m-k]
   Pr_tg = 0.7005
   T_tg[1] = T_tg
   Re_ch_tg = m_dot_tg*D_e/(Pressing_Depth*(w_atgc)*mu_tg)

   N_uD_ATGH = 0.2913*(Re_ch_tg^0.702)*(mu_TG/mu_w)^0.14*(PR_tg^(1/3))
   h_ATGH = N_uD_ATGH/ATGC_L*k_tg
   C_ATGH = m_dot_tg*Cp_Tg

   k_ATGC[i] = Conductivity(Air_ha, T = T_in_air, P = P_in_air)
   Mu_ATGC[i] = Viscosity(Air_ha, T = T_in_air, P = P_in_air)
   Re_ch_air[i] = m_dot_c*Convert(g,kg)*D_e/(Pressing_Depth*(w_atgc)*mu_ATGC[i])
   PR_ATGC[i] = Prandtl(Air_ha, T =T_in_air, P = P_in_air)


   N_uD_ATGC[i] = 0.2913*(Re_ch_air[i]^0.702)*(mu_ATGC[i]/mu_w)^0.14*(Pr_ATGC[i]^(1/3))
   h_ATGC[i] = N_uD_ATGC[i]/ATGC_L*k_ATGC[i]

   C_ATGC[i] = m_dot_c*Convert(g,kg)*Cp_ATGC


   "Heat Exchanger"

   C_r[i] = Min(C_ATGC[i], C_ATGH)/Max(C_ATGC[i], C_ATGH)

   q_max[1] = Min(C_ATGC[i], C_ATGH) * (T_tg[i] - T_in_air)

   U[1] = f/(1/h_ATGH + 1/h_ATGC[i] + ATGC_T/(2*k_plate))

   NTU[1] = U[1] *Convert(w,kw)*(ATG_Area/4)/Min(C_ATGC[i], C_ATGH)

   epsilon[1] = (1-Exp(-NTU[i]*(1-C_r[i])))/(1-(C_r[1]*Exp(-NTU[i]*(1-C_r[i]))))
   q_ATGC[i] = -epsilon[i]*q_max[i]

   q_act_ATGC = q_ATGC[i]
END

FUNCTION q_act_APH (T_in_c, T_in_h, P_in_c, P_in_h, m_dot_c, m_dot_h, Cp_APC, Cp_APH)
   "Air Preheater Properties"
   w_APH = 0.186[m]
   APH_T = 0.002 [m]
   APH_L = 0.613 [m]
   Pressing_Depth = 0.02 [m]
```

```
D_e = 2 * Pressing_depth

APH_A = 15.435 [m^2]
f = 18.05
k_plate = 21.5 [W/m-k]

"Fluid Properties"
mu_w = 0.027 [Pa-s]
"Cold Side"
mu_c = Viscosity(Air_ha, T = T_in_c, P = P_in_c)
k_c = Conductivity(Air_ha, T = T_in_c, P = P_in_c)
Pr_c = Prandtl(Air_ha, T = T_in_c, P = P_in_c)
Re_ch_c = m_dot_c*Convert(g/s,kg/s)*D_e/(Pressing_Depth*(w_APH)*mu_c)

"Hot Side"
mu_h = Viscosity(Air_ha, T =T_in_h, P =P_in_h)
k_h = Conductivity(Air_ha, T = T_in_h, P = P_in_h)
Pr_h = Prandtl(Air_ha, T = T_in_h, P = P_in_h)
Re_ch_h = m_dot_h*Convert(g,kg)*D_e/(Pressing_Depth*(w_APH)*mu_h)

N_uD_c = 0.2913*(Re_ch_c^0.702)*(mu_c/mu_w)^0.14*(PR_c^(1/3))
N_uD_h = 0.2913*(Re_ch_h^0.702)*(mu_h/mu_w)^0.14*(PR_h^(1/3))

h_c = N_uD_c/APH_L*k_c
h_h = N_uD_h/APH_L*k_h

C_c = m_dot_c*Convert(g,kg)*Cp_APC
C_h = m_dot_h*Convert(g,kg)*Cp_APH

"Heat Exchanger"

C_r = Min(C_c, C_h)/Max(C_h, C_c)

q_max = Min(C_c, C_h) * (T_in_h - T_in_c)

U = f/(1/h_h + 1/h_c + APH_T/(2*k_plate))

NTU = U*Convert(w,kw)*(APH_A/4)/Min(C_c, C_H)

epsilon= (1-Exp(-NTU*(1-C_r)))/(1-(C_r*Exp(-NTU*(1-C_r))))
q = epsilon*q_max

q_act_APH = q


END
 "Universal Constants"
g = 9.81 [m/s^2]
Eta_m = 0.85
Turbine_Correction = 0.471 [kW]
T_ref = 298 [K]
P_ref = 1 [bar]
k = 0.014 [m]
mH2O = (9.80655) [kPa/m]
Ambient_Temp = 22 [C]
Ambient_Pressure = 101 [kPa]
Beta = 1/ConvertTemp(c,k,Ambient_Temp)

nu_amb = KinematicViscosity(Air_ha, T = Ambient_Temp, P = Ambient_Pressure)
Pr_amb = Prandtl(Air_ha, T = Ambient_Temp, P = Ambient_Pressure)
k_amb = Conductivity(Air_ha, T = Ambient_Temp, P = Ambient_Pressure)
```

```
"PR_C = 2.05

PR_C2 = 1.323


m_dot_c = 100 [g/s]"
"P_in_PV = 300 [kPa]"

"Pipe Properties----------------------------------------------------------------------------------------------------------------------------------"

"Pipe Properties Final Stretch"
D_pipe_ID = 3 [in] * Convert(in,m)
L_pipe_H = 18 [ft] * Convert(ft,m)
D_pipe_OD = 3.5 [in] * Convert(in,m)
D_pipe_ins = 7.5 [in] * Convert(in,m)
A_pipe =D_pipe_ID^2/4*pi

k_pipe = 22 [W/m-k]
k_ins = 0.14 [W/m-k]

Pipe_Ins_Diameter = 6.375 [in] * Convert(in,m)
A_s_Exhaust = pi*Pipe_diameter*Pipe_Length_exhaust
A_s_CATG = pi*Pipe_diameter*Pipe_Length_CATG
A_s_ATGH = pi*Pipe_diameter*Pipe_Length_ATGH_out

A_s_CATG_ins = pi*Pipe_ins_diameter*Pipe_Length_CATG

Pipe_Length_Exhaust = 20 [ft] * Convert(ft, m)
Pipe_diameter = 2 [in] * Convert(in, m)
Pipe_OD = 2.375 [in] * Convert(in,m)
Pipe_A = Pipe_diameter^2/4*pi
Pipe_Length_CATG = 7.112 [m]
Pipe_Length_ATGH_out = 15 [ft] *Convert(ft,m)

N_e = 12
N_u = 4
N_bv = 4
N_t = 6
N_cv = 2

k_e = 1.5
k_u = 0.08
k_bv = 0.05
k_tee = 2.0
k_cv = 2.0

K_tot = (N_e*k_e + N_u*k_u+N_bv*k_bv+N_t*k_tee+N_cv*k_cv)/10

"Air Pre-heater Properties"
N_Ch_PH = 69
L_PH = 0.613 [m]
W_PH = 0.186 [m]
H_PH = 0.350 [m]
A_PH = ATG_Area*(140/48)


"ATGC Properties----------------------------------------------------------"

N_Ch_ATGC = 24
w_atgc = 0.186 [m]

ATGC_T = 0.002 [m]

,
```

```
ATGC_L = 0.613 [m]
Pressing_Depth = 0.002[m]
ATG_Area = 5.292 [m^2]
f = 2.1865 "Correction Factor"
k_plate = 21.5 [W/m-k]
M_dot_tg = 0.036 [kg/s]

"TG Properties"
Cp_tg = 1.701 [kj/kg-k]
mu_w = 0.027 [pa-s]
mu_tg = 0.00002673 [Pa-s]
k_tg = 0.03949 [w/m-k]
Pr_tg = 0.7005

"Coolant Properties"

"Compressor Stage----------------------------------------------------------------------------------------------------------------------------------"

"Compressor Inlet Properties"
P[1] = 101 [kPa]
T[1] = 22 [C]

M_dot_corrected = M_dot_c*Sqrt(ConvertTemp(C,K,T[1])/(T_ref))/(P[1]*Convert(kPa,bar)/P_ref)

"Compressor 1"
H[1] = Enthalpy(Air_ha, T = T[1], P = P[1])
S[1] = Entropy(Air_ha, T = T[1], P = P[1])

PR_c = P[2]/P[1]

S_s[2] = S[1]
H_s[2] = Enthalpy(Air_ha, P = P[2], S = S_s[2])
H[2] = Enthalpy(Air_ha, P = P[2], T = T_out_c)
Eta_c = Interpolate2DM('CEM22', PR_c, M_dot_corrected)
H[2] = (H_s[2]-H[1])/Eta_c + H[1]
Work[1] = M_dot_c*Convert(g/s,kg/s)* (H[2]-H[1])
Q_gly[1] = Work[1]*(1-Eta_m) + Turbine_Correction
Q_gly[2] = Work[2]*(1-Eta_m) + Turbine_Correction

"Compressor 2"
T[2] =If(PR_c2, 1, T_out_c, T_out_c, 38 [C])

M_dot_corrected_c2 = M_dot_c*Sqrt(ConvertTemp(C,K,T[2])/(T_ref))/(P[2]*Convert(kPa,bar)/P_ref)

H[3] = Enthalpy(Air_ha, T = T[2], P = P[2])
S[3] = Entropy(Air_ha, T = T[2], P = P[2])

PR_c2 = P[3]/P[2]

S_s[4] = S[3]
H_s[4] = Enthalpy(Air_ha, P = P[3], S = S_s[4])
H[4] = Enthalpy(Air_ha, P = P[3], T = T[3])
Eta_c2 = If(PR_c2, 1, 1, 1, Interpolate2DM('CEM38', PR_c2, M_dot_corrected_c2))
H[4] = (H_s[4]-H[3])/Eta_c2 + H[3]
Work[2] = M_dot_c*Convert(g/s,kg/s)*(H[4]-H[3])
PR_tot = PR_c*PR_c2

"Pressure Drop and Temperature Change to Fuel Cell----------------------------------------------------------------------------------------------
----------------------------------------"

"Pipes to ATG Cooler----------------------------------------------------------------------------------------------------------------------------
```

```
----------------------------------------------------------"

Rho_air_c = Density(Air_ha, P = P[3], T = T[3])
Nu_air_c = Viscosity(Air_ha, P = P[3], T = T[3])
omega_c = (M_dot_c * Convert(g/s,kg/s))/Rho_air_c/Pipe_A
Pr_CATG = Prandtl(Air_ha, P = P[3], T = T[3])
Cp_CATG = Cp(Air_ha, P = P[3], T = T[3])
k_air_ATGC = Conductivity(Air_ha, P = P[3], T = T[3])

Re_c = rho_air_c*omega_c*Pipe_Diameter/Nu_air_c

1/Sqrt(lambda_catg) = -2*Log10((2.51/(Re_c*Sqrt(lambda_catg)))+k/Pipe_diameter * 0.269)
DELTAP_catg = ((lambda_catg*Pipe_Length_CATG/Pipe_Diameter*rho_air_c/2*omega_c^2)*Convert(pa,kpa))+h_L_minor
h_L_minor = K_tot *rho_air_c/2*omega_c^2*Convert(pa,kpa)
P[4] = P[3] - DELTAP_catg
T[4] = T[3]

"ATGC----------------------------------------------------------------------------------------------------------------
----------------------------------------------------------"
l_atg = 0.613 [m]
D_h_ATGC = (3.987*10^(-3)) [m]
A_plate = (3.72*10^(-4)) [m^2]

re_ch_air_ATGC = m_dot_c*Convert(g,kg)*D_e/(Pressing_Depth*(w_atgc)*nu_air_c)

f_air_ATGC = 2.990*Re_ch_air_ATGC^(-0.183)
mu_atgc = m_dot_c*Convert(g/s,kg/s)*(1/rho_air_c)*(1/A_plate)
DELTAP_ATGC = 4*f_air_ATGC*(rho_air_c*mu_atgc^2)/2*l_atg/D_h_ATGC * Convert(pa,kpa)/1000

DELTAP_CMSM = DELTAP_ATGC+DELTAP_catg
P_out_ATGC = P[4] - DELTAP_ATGC

"Heat Transfer Constants"
D_e = 2 * Pressing_depth

"ATG Function Calls"

"Tailgas"
T_tg[1] = 275 [C] "Inlet to ATGH"
P_tg_in = P[4]

Re_ch_tg = m_dot_tg*D_e/(Pressing_Depth*(w_atgc)*mu_tg)

N_uD_ATGH = h_ATGH * ATGC_L/k_tg
N_uD_ATGH = 0.2913*(Re_ch_tg^0.702)*(mu_TG/mu_w)^0.14*(PR_tg^(1/3))

C_ATGH = m_dot_tg*Cp_Tg
T_air_ATGC[1] = T[4]

Cp_ATGC[1] = Cp(Air_ha, T  = T_air_ATGC[1], P = P[4])
q_ATGC[1] = q_act_ATGC(T_air_ATGC[1], T_tg[1], P[4], 1,m_dot_c,CP_ATGC[1],T_tg[4])
q_ATGC[1] = -m_dot_c*Convert(g,kg)*Cp_ATGC[1]*(T_air_atgc[2]-T_air_atgc[1] )
q_ATGC[1] = m_dot_tg*cp_tg*(T_tg[4]-T_tg[5])

Cp_ATGC[2] = Cp(Air_ha, T  = T_air_ATGC[2], P = P[4])
q_ATGC[2] = q_act_ATGC(T_air_ATGC[2], T_tg[2], P[4], 1,m_dot_c,CP_ATGC[2],T_tg[3])
q_ATGC[2] = -m_dot_c*Convert(g,kg)*Cp_ATGC[2]*(T_air_atgc[3]-T_air_atgc[2])
q_ATGC[2] = -m_dot_tg*cp_tg*(T_tg[3]-T_tg[4])

Cp_ATGC[3] = Cp(Air_ha, T  = T_air_ATGC[3], P = P[4])
```

```
q_ATGC[3] = q_act_ATGC(T_air_ATGC[3], T_tg[3], P[4], 1,m_dot_c,CP_ATGC[3],T_tg[2])
q_ATGC[3] = -m_dot_c*Convert(g,kg)*Cp_ATGC[3]*(T_air_atgc[4]-T_air_atgc[3])
q_ATGC[3] = -m_dot_tg*cp_tg*(T_tg[2]-T_tg[3])

Cp_ATGC[4] = Cp(Air_ha, T  = T_air_ATGC[4], P = P[4])
q_ATGC[4] = q_act_ATGC(T_air_ATGC[4], T_tg[4], P[4], 1,m_dot_c,CP_ATGC[4],T_tg[1])
q_ATGC[4] = -m_dot_c*Convert(g,kg)*Cp_ATGC[4]*(T_air_atgc[5]-T_air_atgc[4])
q_ATGC[4] = -m_dot_tg*cp_tg*(T_tg[1]-T_tg[2])

q_ATGC_Tot = q_ATGC[1] + q_ATGC[2] + q_ATGC[3] + q_ATGC[4]

T_ATGC_Out = T_air_atgc[5]

"Air Preheater"

"Pressure Drop"

nu_PH_in_c = Viscosity(Air_ha, T = T_ATGC_OUT, P = P_Out_ATGC)
rho_PH_in_c = Density(Air_ha, T = T_ATGC_Out, P = P_Out_ATGC)

re_ch_air_APHC = m_dot_c*Convert(g,kg)*D_e/(Pressing_Depth*(w_atgc)*nu_PH_in_c)

f_air_APHC = 2.990*Re_ch_air_APHC^(-0.183)
mu_aphc = m_dot_c*Convert(g/s,kg/s)*(1/rho_PH_in_C)*(1/A_plate)
DELTAP_APHC = 4*f_air_APHC*(rho_PH_in_C*mu_APHC^2)/2*l_atg/D_h_ATGC * Convert(pa,kpa)/1000


P[5] = P_Out_ATGC - DELTAP_APHC

"Heat Exchanger Function Calls"
T_APH[5] = T[6]

Cp_APC[1] = Cp(Air_ha, T  = T_ATGC_Out, P = P_Out_ATGC)
Cp_APH[1] = Cp(Air_ha, T = T_APH[1], P = P[6])

q_APH[1] = q_act_APH(T_ATGC_Out, T_APH[2], P_OUT_ATGC, P[6], M_dot_c, M_dot_e, Cp_APC[1], Cp_APH[1])
q_APH[1] = m_dot_c*Convert(g,kg)*Cp_APC[1]*(T_APC[1] - T_ATGC_Out)
q_APH[1] = m_dot_e*Convert(g,kg)*Cp_APH[1]*(T_APH[2] - T_APH[1])

Cp_APC[2] = Cp(Air_ha, T = T_APC[1], P = P_Out_ATGC)
Cp_APH[2] = Cp(Air_ha, T = T_APH[2], P = P[6])

q_APH[2] = q_act_APH(T_APC[1], T_APH[3], P_Out_ATGC, P[6], M_dot_c,M_dot_e, Cp_APC[2], Cp_APH[2])
q_APH[2] = m_dot_c*Convert(g,kg)*Cp_APC[2]*(T_APC[2]-T_APC[1])
q_APH[2] = m_dot_e*Convert(g,kg)*Cp_APH[2]*(T_APH[3] - T_APH[2])

Cp_APC[3] = Cp(Air_ha, T = T_APC[2], P = P_Out_ATGC)
Cp_APH[3] = Cp(Air_ha, T = T_APH[3], P = P[6])

q_APH[3] = q_act_APH(T_APC[2], T_APH[4], P_Out_ATGC, P[6], M_dot_c,M_dot_e, Cp_APC[3], Cp_APH[3])
q_APH[3] = m_dot_c*Convert(g,kg)*Cp_APC[3]*(T_APC[3]-T_APC[2])
q_APH[3] = m_dot_e*Convert(g,kg)*Cp_APH[3]*(T_APH[4] - T_APH[3])

Cp_APC[4] = Cp(Air_ha, T = T_APC[3], P = P_Out_ATGC)
Cp_APH[4] = Cp(Air_ha, T = T_APH[5], P = P[6])

q_APH[4] = q_act_APH(T_APC[3], T_APH[5], P_Out_ATGC, P[6], M_dot_c,M_dot_e, Cp_APC[4], Cp_APH[4])
q_APH[4] = m_dot_c*Convert(g,kg)*Cp_APC[4]*(T_APC[4]-T_APC[3])
q_APH[4] = m_dot_e*Convert(g,kg)*Cp_APH[4]*(T_APH[5] - T_APH[4])
```

```
q_APH_Tot = q_APH[1] + q_APH[2]+q_APH[3]+q_APH[4]
T_out_Preheater = T_APC[4]
q_HEX_tot = q_APH_tot - q_ATGC_tot

"Drop through pipes out of the Pre-heater"

Rho_air_APO = Density(Air_ha, P = P[5], T = T_out_Preheater)
Nu_air_APO = Viscosity(Air_ha, P = P[5], T = T_out_Preheater)
omega_APO = (M_dot_c * Convert(g/s,kg/s))/Rho_air_APO/A_pipe
Pr_APO = Prandtl(Air_ha, P = P[5], T = T_out_Preheater)
Cp_APO = Cp(Air_ha, P = P[5], T = T_out_Preheater)
k_air_APO = Conductivity(Air_ha, P = P[5], T = T_out_Preheater)

Re_APO = rho_air_APO*omega_APO*D_pipe_ID/Nu_air_APO


1/Sqrt(lambda_APO) = -2*Log10((2.51/(Re_APO*Sqrt(lambda_APO)))+k/D_pipe_ID* 0.269)
DELTAP_APO = ((lambda_APO*L_pipe_H/D_Pipe_ID*rho_air_APO/2*omega_APO^2)*Convert(pa,kpa))+h_L_minor_APO
h_L_minor_APO = (K_tot-2) *rho_air_APO/2*omega_APO^2*Convert(pa,kpa)
T[5] = T_out_Preheater
P_in_PV = P[5] - DELTAP_APO


"MSM and Vessel----------------------------------------------------------------------------------------------------------
----------------------------------------"
DELTAP_MSM = Interpolate2DM('Pressure Vessel Drop', P_in_PV, m_dot_c)
P[6] = P[5] - DELTAP_MSM
T_out_PV = 630 [C]
P_MSM_Out = P[6]
T[6] = T_out_PV
"Vessel Outlet to APH Inlet"
Rho_air_VO = Density(Air_ha, P = P[6], T = T_out_PV)
```

```
Nu_air_VO = Viscosity(Air_ha, P = P[6], T = T_out_PV)
omega_VO = (M_dot_c * Convert(g/s,kg/s))/Rho_air_VO/A_pipe
Pr_VO = Prandtl(Air_ha, P = P[6], T = T_out_PV)
Cp_VO = Cp(Air_ha,P = P[6], T = T_out_PV)
k_air_VO = Conductivity(Air_ha, P = P[6],  T =T_out_PV)

Re_VO = rho_air_VO*omega_VO*D_pipe_ID/Nu_air_VO

1/Sqrt(lambda_VO) = -2*Log10((2.51/(Re_VO*Sqrt(lambda_VO)))+k/D_pipe_ID* 0.269)
DELTAP_VO = ((lambda_VO*L_pipe_H/D_Pipe_ID*rho_air_VO/2*omega_VO^2)*Convert(pa,kpa))+h_L_minor_VO
h_L_minor_VO = (K_tot-2) *rho_air_VO/2*omega_VO^2*Convert(pa,kpa)
P_in_APH = P[6] - DELTAP_VO
T_in_APH = T_out_PV


"APH HOT----------------------------------------------------------------------------------------------------------------
-----------------------------------"
Rho_air_MSM = Density(Air_ha, P = P_MSM_Out, T = (630 [c]))
Nu_air_MSM = Viscosity(Air_ha, P = P_MSM_Out, T = (630 [c]))
mu_msm_p = M_dot_e*Convert(g/s,kg/s)/Rho_air_msm/Pipe_A
Re_MSM = rho_air_msm*mu_msm_p*Pipe_Diameter/Nu_air_msm

mu_msm = m_dot_e * Convert(g/s,kg/s)*(1/rho_air_msm)*(1/A_plate)
f_air_ATGH = 2.990*Re_MSM^(-0.183)
DELTAP_ATGH = 4*f_air_ATGH*(rho_air_msm*mu_msm^2/2)*l_atg/D_h_ATGC *Convert(pa,kpa)/1000
P_ATGH_out = P_MSM_Out - DELTAP_ATGH
P[7] = P[6] - DELTAP_ATGH

"Pressure Drop Across Pipes out of APH HOT-------------------------------------------------------------------------------
-----------------------------"
T_ATGH_out = T_APH[4]
T_avg_e = (T_ATGH_out + T_in_e)/2

Rho_air_ATGH_out = Density(Air_ha, P = P_ATGH_out, T = T_avg_e)
Nu_air_ATGH_out = Viscosity(Air_ha, P = P_ATGH_out, T = T_avg_e)

mu_ATGH_out = M_dot_e * Convert(g/s,kg/s)/Rho_air_ATGH_out/Pipe_A
Re_ATGH_out = rho_air_atgh_out*mu_atgh_out*Pipe_Diameter/Nu_air_ATGH_out

1/Sqrt(lambda_atgh) = -2*Log10((2.51/(Re_ATGH_out*Sqrt(lambda_atgh)))+k/Pipe_diameter * 0.269)
DELTAP_ATGH_e = (lambda_atgh*Pipe_Length_ATGH_out/Pipe_Diameter*rho_air_ATGH_out/2*mu_ATGH_out^2)*
Convert(pa,kpa)

P[8] = P_in_e

P_in_e = P_ATGH_out - DELTAP_ATGH_e

"Expansion Stage--------------------------------------------------------------------------------------------------------
-----------------------------------------"

"Stage 1"

"Expander Inlet Properties----------------------------------------------------------------------------------------------
-----------------------------------------"

M_dot_e = M_dot_c - 8 [g/s]
M_dot_corrected_e = M_dot_e*Sqrt(ConvertTemp(C,K,T_in_e)/(T_ref))/(P_in_e*Convert(kPa,bar)/(P_ref))
```

```
T_in_e = 115 [C]

P_out_e = P_in_e/PR_e
P[9] = P_out_e

"Bypass Calculation----------------------------------------------------------------------------------------------------------------------------
-------------------------------------"
PR_Max = P_in_e/P_out_e2_test
PR_e = If(PR_e_test, PR_MAX, PR_e_test, PR_MAX, PR_Max)
Bypass_E2 = If(PR_c2, 1, 0, 0, If(PR_e, PR_Max, 0,1,1))

Turbine_Max = Interpolate2DM('TM', PR_e, M_dot_corrected_e)
Bypass =  If(Turbine_Max, M_dot_corrected_e, (M_dot_corrected_e - (M_dot_corrected_e-Turbine_Max))/M_dot_corrected_e,
 1, 1)

M_dot_reduced_new = M_dot_reduced * Bypass
M_dot_reduced = M_dot_e * Convert(g/s,kg/s)* Sqrt(ConvertTemp(c,k,T_in_e))/P_in_e

"Pressure Drop Across Turbine----------------------------------------------------------------------------------------------------------------
-----------------------------------------------"

PR_e_test = Interpolate('TMAX', 'Reduced_Flow', 'PR', Reduced_Flow = M_dot_reduced_new)
Eta_e = Interpolate2DM('EEM115', PR_e, M_dot_reduced_new)

"Performance Calculations----------------------------------------------------------------------------------------------------------------------
-----------------------------------------"

H[5] = Enthalpy(Air_ha, T = T_in_e, P = P_in_e)
S[5] = Entropy(Air_ha, T = T_in_e, P = P_in_e)

S_s[6] = S[5]
H_s[6] = Enthalpy(Air_ha, P = P_out_e, S = S_s[6])
H[6] = Eta_e * (H_s[6]-H[5]) + H[5]

Work_e = Bypass*M_dot_e*Convert(g/s,kg/s)* (H[6]-H[5])
Work_T_1 = Work[1] + Q_gly[1] + Work_e

cp_e  =  Cp(Air_ha, T = T_out_e, P = P_out_e)
T_out_e = Temperature(Air_ha, H = H[6], P = P_out_e)
T_out_e_corr = T_out_e - Turbine_Correction/(cp_e * m_dot_e * bypass * Convert(g,kg))


"Stage 2----------------------------------------------------------------------------------------------------------------------------------
-----------------------------"

M_dot_corrected_e2 = M_dot_e*Sqrt(ConvertTemp(C,K,T_in_e2)/(T_ref))/(P_in_e2*Convert(kPa,bar)/(P_ref))

T_in_e2 = T_out_e_corr
P_in_e2 = P_out_e

P_out_e2 = P_in_e2/PR_e2

"Bypass Calculations----------------------------------------------------------------------------------------------------------------------
-----------------------------------------"

Turbine_Max_2 = Interpolate2DM('TM', PR_e2, M_dot_corrected_e2)

Bypass2 =If(Bypass_E2, 1, If(Turbine_Max_2, M_dot_corrected_e2, Turbine_Max_2/M_dot_corrected_e2, 1,1), 0, 0)
```

```
M_dot_reduced_new2 = M_dot_reduced_e2 *Bypass2
M_dot_reduced_e2 = M_dot_e * Convert(g/s,kg/s) * Sqrt(ConvertTemp(c,k,T_in_e2))/P_in_e2

"Pressure Drop Across Turbine----------
----------"
TMAX_e2 = P_in_e2/P_out_e2_test
PR_e2_int = If(Bypass2,0,1,1, Interpolate('TMAX', 'Reduced_Flow', 'PR', Reduced_Flow = M_dot_reduced_new2))
PR_e2 = If(PR_e2_int, TMAX_e2, PR_e2_int, TMAX_e2, TMAX_e2)
Eta_e2 = If(Bypass2, 0, 1, 1, Interpolate2DM('EEM115', PR_e2, M_dot_reduced_new2))

"Ensuring outlet is not below limit----------
----------"

Rho_air_e_test = Density(Air_ha, P = P_out_e2_test, T = 50 [C])
Nu_air_e_test = Viscosity(Air_ha, P = P_out_e2_test, T = 50 [C])
omega_e_test = M_dot_e*Convert(g/s,kg/s)*1/Rho_air_e_test*1/Pipe_A

Reynolds_e_test = rho_air_e_test*omega_e_test*Pipe_Diameter/Nu_air_e_test

1/Sqrt(lambda_e_test) = -2*Log10((2.51/(Reynolds_e_test*Sqrt(lambda_e_test)))+k/Pipe_diameter * 0.269)
DELTAP_e_test = 0.5 * ((lambda_e_test*Pipe_Length_exhaust/Pipe_Diameter*rho_air_e_test/2*omega_e_test^2)*Convert(
pa,kpa)) + 3 [kPa]
P_exhaust_test = 101 [kPa]
P_out_e2_test = P_exhaust_test + DELTAP_e_test

"Performance Calculations----------
----------"

H[7] = Enthalpy(Air_ha, T = T_in_e2, P = P_in_e2)
S[7] = Entropy(Air_ha, T = T_in_e2, P = P_in_e2)

S_s[8] = S[7]
H_s[8] = Enthalpy(Air_ha, P = P_out_e2, S = S_s[8])
H[8] = Eta_e2 * (H_s[8] - H[7]) + H[7]

Work_e2 = Bypass2*M_dot_e*Convert(g/s,kg/s)*(H[8]-H[7])
Work_T_2 = If(PR_c2, 1, 0,0, Work[2] + Q_gly[2] + Work_e2)

cp_e2 = Cp(Air_ha, T = T_out_e2, P = P_out_e2)
T_out_e2 = Temperature(Air_ha, H = H[8], P = P_out_e2)
T_out_e2_corr = If(0.05 ,bypass2, T_out_e2 - Turbine_Correction/(cp_e2 * ((m_dot_e * bypass2)+0.05[g/s]) * Convert(g,kg)),
T_out_e2, T_out_e2)

Work_Total =Work_T_2 + Work_T_1

"Pressure Drop to Exhaust----------
----------"

P_exhaust = P_out_e2 - DELTAP_e
P_avg = (P_exhaust + P_out_e2)/2

Rho_air_e = Density(Air_ha, P = P_out_e, T = T_out_e2_corr)
Nu_air_e = Viscosity(Air_ha, P =P_out_e, T = T_out_e2_corr)
omega_e = (M_dot_e*Bypass * Convert(g/s,kg/s))/Rho_air_e/Pipe_A

Reynolds_e = rho_air_e*omega_e*Pipe_Diameter/Nu_air_e


1/Sqrt(lambda_e) = -2*Log10((2.51/(Reynolds_e*Sqrt(lambda_e)))+k/Pipe_diameter * 0.269)

DELTAP_e = 0.5 * ((lambda_e*Pipe_Length_exhaust/Pipe_Diameter*rho_air_e/2*omega_e^2)*Convert(pa,kpa))
```

APPENDIX C. P&ID OF SYSTEM

General System Layout

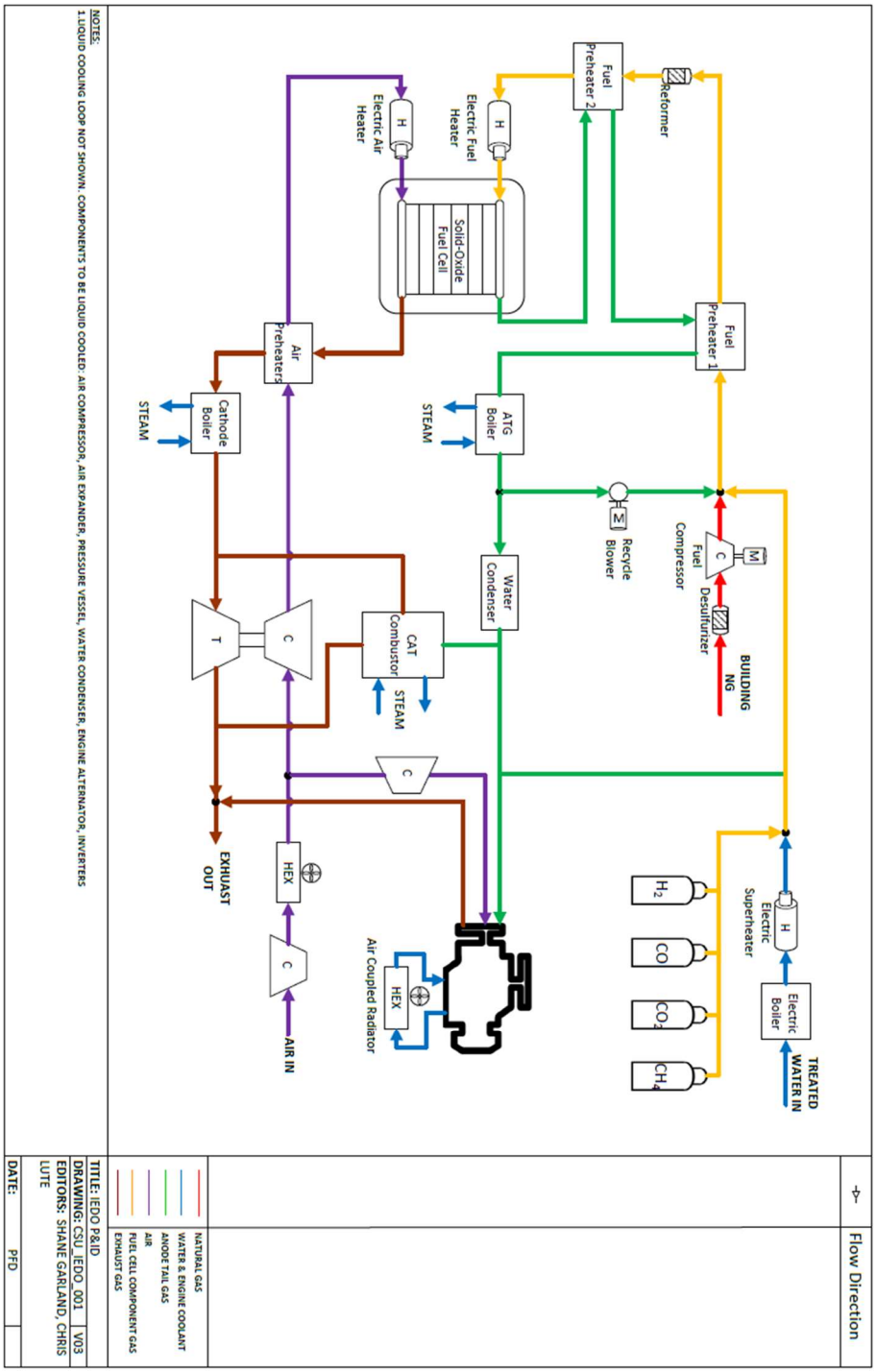

Air BOP

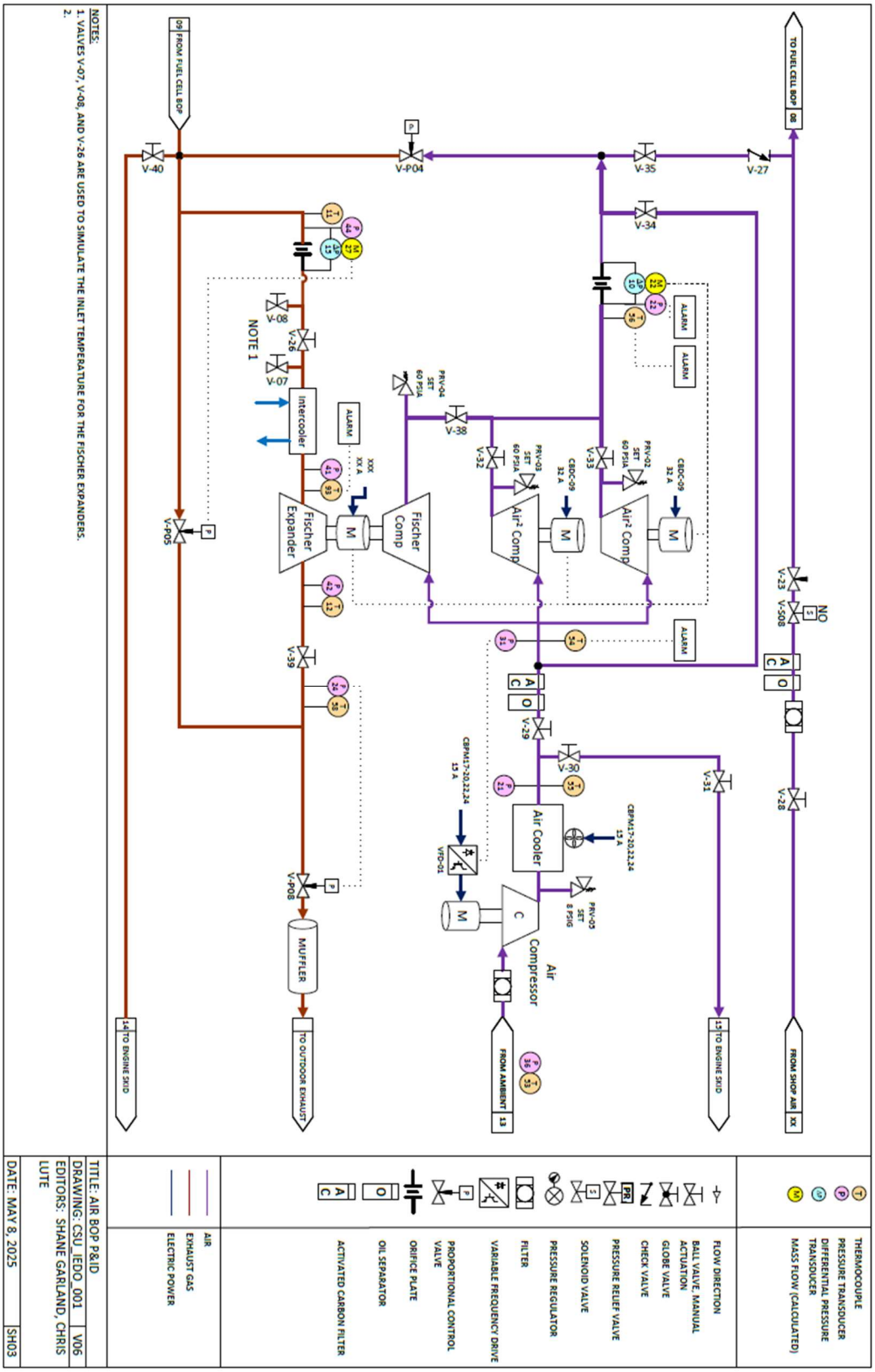
TO FUEL CELL BOP
FROM SHOP AIR
FROM FUEL CELL BOP
TO ENGINE SKID
TO OUTDOOR EXHAUST
FROM AMBIENT
MUFFLER
Intercooler
Fischer Expander
Fischer Comp
Air² Comp
Air² Comp
Air Cooler
Air Compressor
ALARM
NOTE 1
NO
V-01
V-02
V-03
V-04
V-05
V-06
V-07
V-08
V-23
V-26
V-27
V-28
V-29
V-30
V-31
V-32
V-33
V-34
V-35
V-38
V-39
V-40
V-P04
V-P05
V-P06
PRV-01 SET 60 PSIA
PRV-02 SET 60 PSIA
PRV-03 SET 60 PSIA
PRV-04 SET 60 PSIA
PRV-05 SET 8 PSIG
CBDC-09 32 A
CBPM17-30,32,24 13 A
CBPM17-30,32,24 13 A
VFD-01
XXX XX A
THERMOCOUPLE
PRESSURE TRANSDUCER
DIFFERENTIAL PRESSURE TRANSDUCER
MASS FLOW (CALCULATED)
FLOW DIRECTION
BALL VALVE, MANUAL ACTUATION
GLOBE VALVE
CHECK VALVE
PRESSURE RELIEF VALVE
SOLENOID VALVE
PRESSURE REGULATOR
FILTER
VARIABLE FREQUENCY DRIVE
PROPORTIONAL CONTROL VALVE
ORIFICE PLATE
OIL SEPARATOR
ACTIVATED CARBON FILTER
AIR
EXHAUST GAS
ELECTRIC POWER
NOTES:
1. VALVES V-07, V-08, AND V-26 ARE USED TO SIMULATE THE INLET TEMPERATURE FOR THE FISCHER EXPANDERS.
2.
TITLE: AIR BOP P&ID
DRAWING: CSU_JEDO_001
V06
EDITORS: SHANE GARLAND, CHRIS LUTE
DATE: MAY 8, 2025
SH03

Engine P&ID

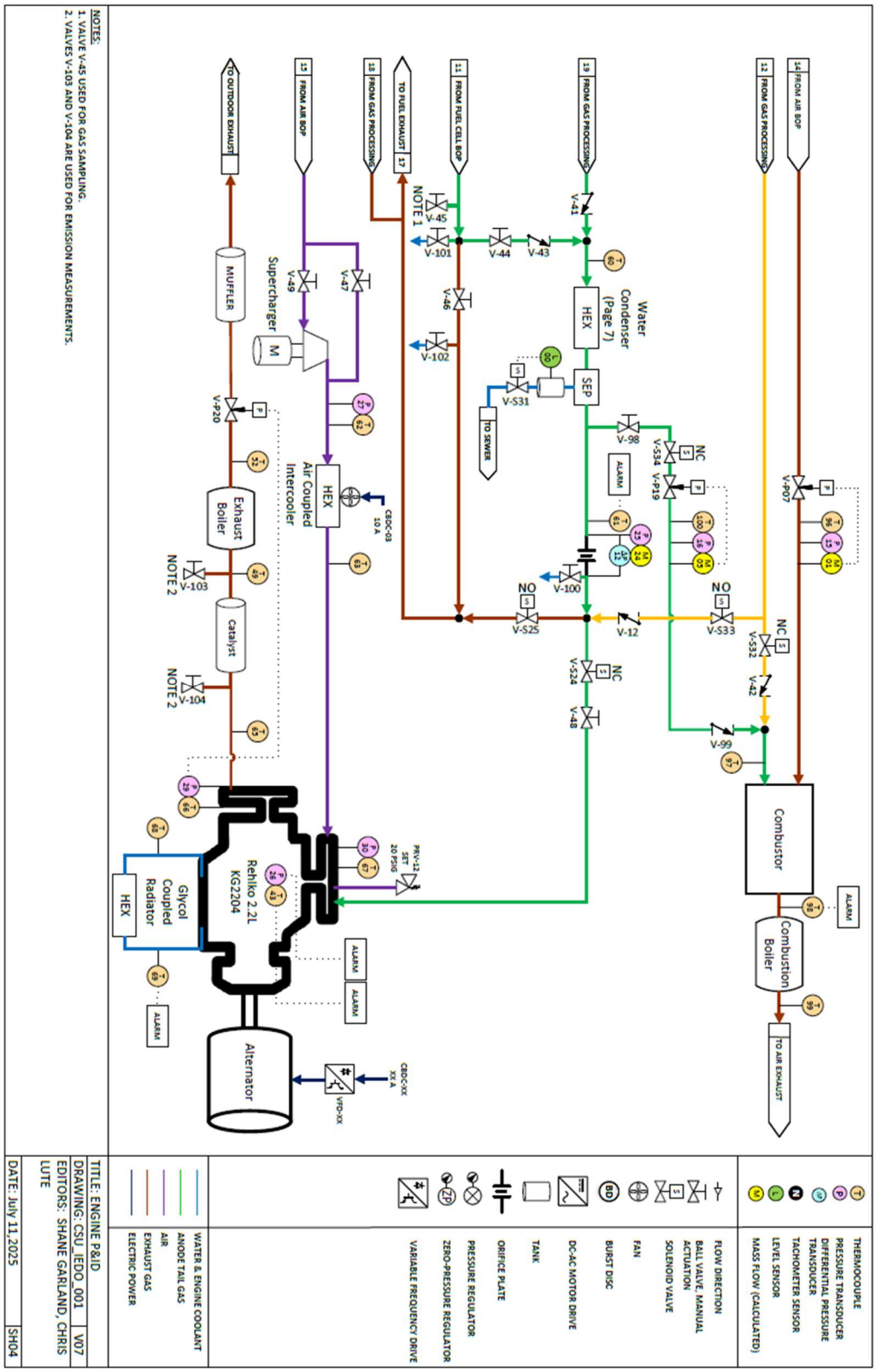
NOTES:
1. VALVE V-45 USED FOR GAS SAMPLING.
2. VALVES V-103 AND V-104 ARE USED FOR EMISSION MEASUREMENTS.
THERMOCOUPLE
PRESSURE TRANSDUCER
DIFFERENTIAL PRESSURE TRANSDUCER
TACHOMETER SENSOR
LEVEL SENSOR
MASS FLOW (CALCULATED)
FLOW DIRECTION
BALL VALVE, MANUAL ACTUATION
SOLENOID VALVE
FAN
BURST DISC
DC-AC MOTOR DRIVE
TANK
ORIFICE PLATE
PRESSURE REGULATOR
ZERO-PRESSURE REGULATOR
VARIABLE FREQUENCY DRIVE
WATER & ENGINE COOLANT
ANODE TAIL GAS
AIR
EXHAUST GAS
ELECTRIC POWER
TITLE: ENGINE P&ID
DRAWING: CSU_IEDO_001
V07
EDITORS: SHANE GARLAND, CHRIS LUTE
DATE: July 11,2025
SH04
FROM AIR BOP
FROM GAS PROCESSING
FROM FUEL CELL BOP
TO FUEL EXHAUST
TO OUTDOOR EXHAUST
TO SEWER
TO AIR EXHAUST
V-P07
V-41
V-45
V-101
V-44
V-43
V-46
V-102
V-47
V-49
Supercharger
M
MUFFLER
V-P20
Water Condenser (Page 7)
HEX
SEP
V-S31
V-98
V-S34
V-P19
NC
ALARM
V-100
NO
V-S25
V-S33
V-12
V-S32
V-42
V-S24
V-48
V-99
Combustor
Combustion Boiler
Air Coupled Intercooler
HEX
CEDC-03 10 A
Exhaust Boiler
V-103
NOTE 2
catalyst
V-104
NOTE 2
NOTE 1
PRV-12 SET 20 PSIG
Rehlko 2.2L KG2204
Glycol Coupled Radiator
HEX
Alternator
VFD-XX
CEDC-XX XX A

Fuel Processing

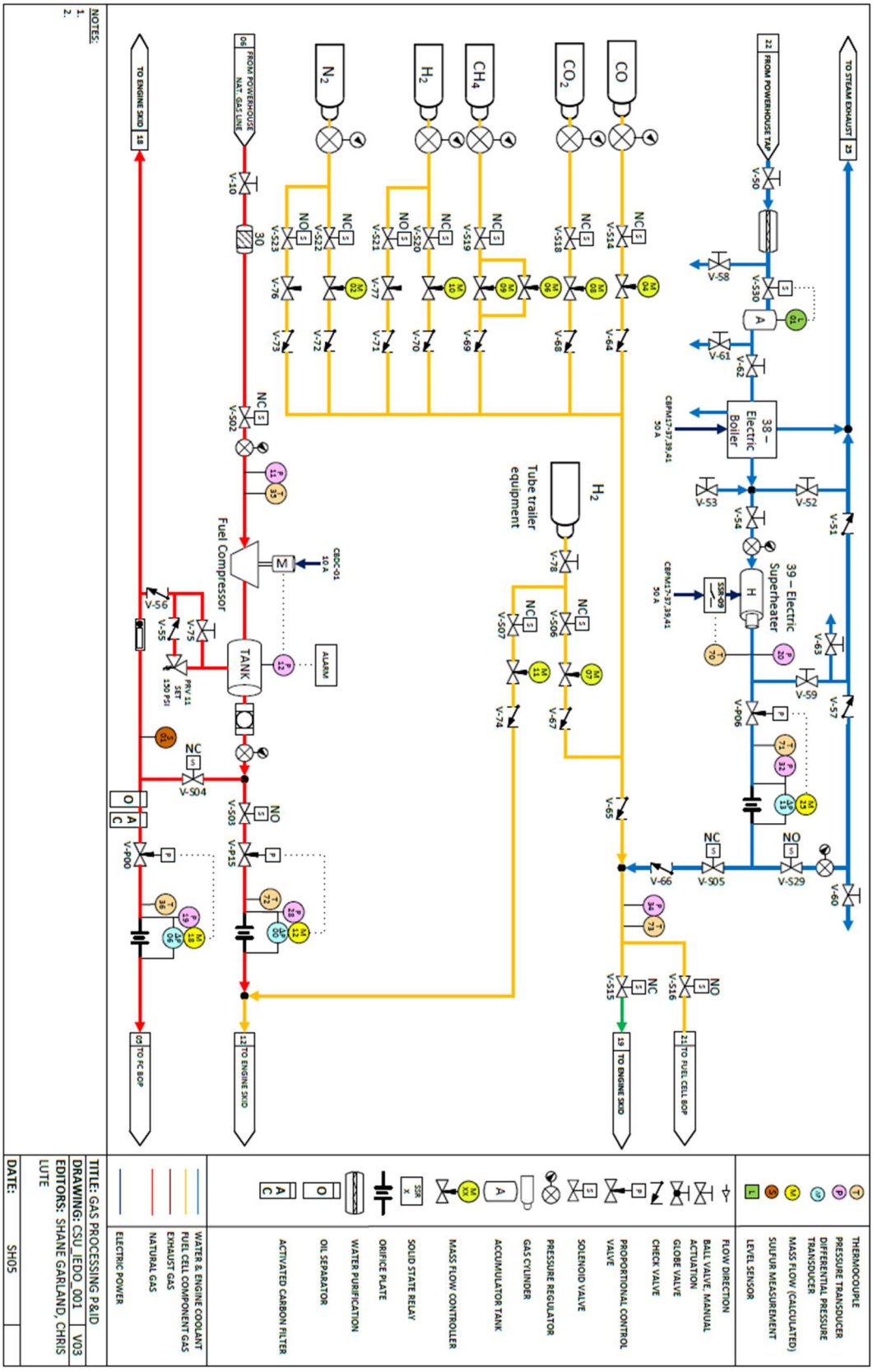

Coolant System

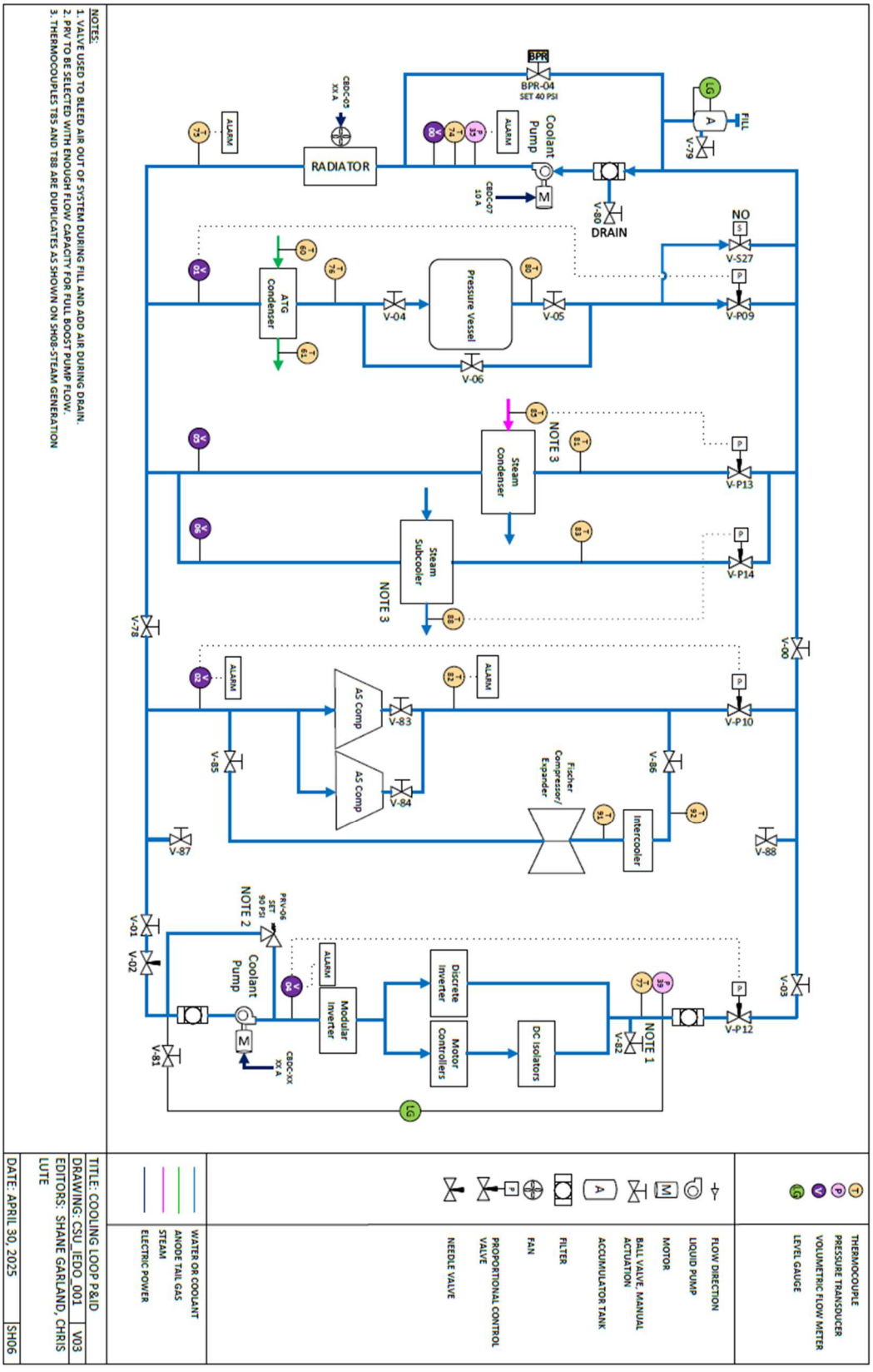

APPENDIX D. FISCHER OPERATING PROCEDURES

Fischer Compressor-Turbine Operation

Step 0. Turn on LabVIEW by following steps in section 6.2.

Step 1. Turn on Cooling Loop Skid by following steps in section 6.4.

- Open valves located under Fischer device along the coolant lines to allow flow of coolant through both the Fischer device and the inverters.
- Shut coolant valves to Air-Squared

Step 2. Check valve configuration for Air BOP to ensure a flow path is open or activate any valves which are required. Ensure that that P-04,05,06,08 are all set to 100% open at start of operation

- For compressor operation:
  - Open Valves: V-38, V-29
  - Close Valves: V-33 and V-32
- If including turbine operation:
  - Open Valves: V-26, V-40, V-39
  - Close Valves: V-40, V-37, V-36
  - If using heater cart:
    - Open valves V-07, V-08
    - Close valve V-26

Step 3. Turn on fuse disconnect switch. Then enter the LabView inverter page and press the button for the inverter start

Step 4. Start Fischer device at idle speed (20,000 RPM)

Step 5. Turn on Sea Level Air Compressor by following steps in Section 6.6.

Step 6. Increase Fischer to desire speed.

- Ensure no compressor surge occurs by stepping the speed incrementally with the pressure ratio regulated by V-P04

Step 7. Increase V-P04 setpoint and/or use PI controlled to achieve desired pressure on compressor side.

If using turbine:

- Increase V-P08 setpoint and/or use PI controlled to achieve desired pressure on turbine side.
- Increase V-P05 setpoint and/or use PI controlled to achieve desired mass flow on turbine side.

Step 8. If necessary, close V-P08 to achieve desired pressure.

Step 9. For use of heater cart:

- Step 9.1: Ensure the manual knobs are at 0 and then plug in heater cart cables to 480 V plug
- Step 9.2: Attach insulated hosing to the hose barbs on Valve 07 and 08 (hoses connect at appropriate heights)
- Step 9.3: Open LabView heater cart section and turn on the devices, adjust temperature according to thermocouple at outlet (**DO NOT EXCEED 120 °C).**

  NOTICE! Slowly ramp up the heater before going to the full desired temperature as it can overshoot.

  Do not exceed 110,000 RPM and pay close attention to map on LabVIEW to not enter stall or surge regions.

Fischer Compressor-Turbine Shutdown

Step 1. Shut down the heater cart heaters

Step 2. Ramp the Fischer speed down from operating speed to 20 KRPM

> **NOTICE! When ramping down the speed of the Fischer device, ensure it remains away from the surge region of the map.**

Step 3. Once at Fischer speed of 20 KRPM manually ramp the sea level compressor to 5 Hz and shut it down using steps in section 6.6.

Step 4. Shut off the Fischer Compressor.

Step 5. Close all Proportional valves that were opened in the starting process

Step 5. Shutoff the inverter and ensure that the fuse disconnect is open.

Step 6. Turn off Cooling Loop by following the steps in Section 6.4.

Step 7. Return all valves to standard position.

Step 9. Press E-Stop Button on WholeSystem.VIS

LIST OF ACRONYMS

Acronym	Definition
ICE	Internal Combustion Engine
GT	Gas Turbine
SOFC	Solid Oxide Fuel Cell
CSU	Colorado State University
CSM	Colorado School of Mines
BOP	Balance of Plant
ATG	Anode Tail Gas
SI	Spark Ignited
HCCI	Homogeneous Charge Compression Ignition
RCCI	Reactivity Controlled Compression Ignition
SOFC-ICE	Solid Oxide Fuel Cell & Reciprocating Internal Combustion Engine Hybrid
LHV	Lower Heating Value
SAI	Spark Assisted Ignition
MSM	Multi-Stack Module
HEX	Heat Exchanger
NTU	Number of Transfer Units